

HCOOCH₃ as a probe of temperature and structure of Orion-KL ★★★

C. Favre^{1,2}, D. Despois^{1,2}, N. Brouillet^{1,2}, A. Baudry^{1,2}, F. Combes³, M. Guélin⁴, A. Wootten⁵, and G. Włodarczak⁶

¹ Université de Bordeaux, OASU, 2 rue de l'Observatoire, BP 89, 33271 Floirac Cedex, France
e-mail: favre@phys.au.dk, despois, brouillet, baudry@obs.u-bordeaux1.fr

² CNRS, UMR 5804, Laboratoire d'Astrophysique de Bordeaux, 2 rue de l'Observatoire, BP 89, 33271 Floirac Cedex, France

³ Observatoire de Paris, LERMA, 61 Av. de l'Observatoire, 75014 Paris, France
e-mail: francoise.combes@obspm.fr

⁴ Institut de Radioastronomie Millimétrique, Domaine Universitaire, 300 rue de la piscine, St Martin d'Hères, 38400, France
e-mail: guelin@iram.fr

⁵ National Radio Astronomy Observatory, 520 Edgemont Road, Charlottesville, VA 22903-2475, USA
e-mail: awootten@nrao.edu

⁶ Laboratoire de Physique des Lasers, Atomes et Molécules, Université de Lille1, UMR 8523, 59655 Villeneuve d'Ascq Cedex, France
e-mail: georges.wlodarczak@univ-lille1.fr

Received July 07, 2010; accepted March 04, 2011

ABSTRACT

Context. The Orion Kleinmann-Low nebula (Orion-KL) is a complex region of star formation. Whereas its proximity allows studies on a scale of a few hundred AU, spectral confusion makes it difficult to identify molecules with low abundances.

Aims. We studied an important oxygenated molecule, HCOOCH₃, to characterize the physical conditions, temperature and density of the different molecular source components. Methyl formate presents strong close rotational transitions covering a large range of energy and its emission in Orion-KL is not contaminated by the emission of N-bearing molecules. This study will help in the future 1) to constrain chemical models for the formation of methyl formate in gas phase or on grain mantles, 2) to search for more complex or prebiotic molecules.

Methods. To reduce the spectral confusion we used high resolution observations from the IRAM Plateau de Bure Interferometer in order to better isolate the molecular emission regions. We used twelve data sets with a spatial resolution down to 1.8'' × 0.8''. Continuum emission was subtracted by selecting apparently line free channels.

Results. We identify 28 methyl formate emission peaks throughout the 50'' field of observations. The two strongest peaks, named MF1 and MF2, are in the Compact Ridge and in the South West of the Hot Core respectively. From a comparison with single dish observations, we estimate that we miss less than 15% of the flux and that spectral confusion is still prevailing as half of the expected transitions are blended over the region. Assuming that the transitions are thermalized, we derive the temperature at the five main emission peaks. At the MF1 position in the Compact Ridge we find a temperature of 80 K in a 1.8'' × 0.8'' beam size and 120 K on a larger scale (3.6'' × 2.2''), suggesting an external source of heating, whereas the temperature is about 130 K at the MF2 position on both scales. Transitions of methyl formate in its first torsionally excited state are detected as well and the good agreement of the positions on the rotational diagrams between the ground state and the $v_t=1$ transitions suggests a similar temperature. The LSR velocity of the gas is between 7.5 and 8.0 km s⁻¹ depending on the positions and column density peaks vary from 1.6 × 10¹⁶ to 1.6 × 10¹⁷ cm⁻². A second velocity component is observed around 9-10 km s⁻¹ in a North-South structure stretching from the Compact Ridge up to the BN object; this component is warmer at the MF1 peak. The two other C₂H₄O₂ isomers are not detected and the derived upper limit for the column density is ≤ 3 × 10¹⁴ cm⁻² for glycolaldehyde and ≤ 2 × 10¹⁵ cm⁻² for acetic acid. From the 223 GHz continuum map, we identify several dust clumps with associated gas masses in the range 0.8 to 5.8 M_⊙. Assuming that the methyl formate is spatially distributed as the dust, we find relative abundances of methyl formate in the range ≤ 0.1 × 10⁻⁸ to 5.2 × 10⁻⁸. We suggest a relation between the methyl formate distribution and shocks as traced by 2.12 μm H₂ emission.

Key words. Astrochemistry – ISM: molecules – Radio lines: ISM – ISM: individual objects: Orion-KL

1. Introduction

The Orion Nebula is one of the most studied regions in the sky. It contains remarkable groups of bright, visible stars and, at the

same time, it is an extremely rich region of star formation, up to very high masses. In addition, it is the closest high-mass star formation region to the Sun (414 ± 7 pc, Menten et al. 2007). It is thus the best source to investigate with very high spatial resolution the processes leading to star formation. However, Orion cannot be considered as the prototypical star-forming region in our Galaxy because it exhibits some unique characteristics which need to be understood before any generalization is made.

The Orion Kleinmann-Low nebula is an atypical region of the Orion Molecular Cloud 1 (OMC-1), which harbours one of the most luminous embedded IR sources of this region (luminosity ~ 10⁵ L_⊙, Wynn-Williams et al. 1984). Several molec-

* Based on observations carried out with the IRAM Plateau de Bure Interferometer. IRAM is supported by INSU/CNRS (France), MPG (Germany) and IGN (Spain).

** A fits image of the HCOOCH₃ integrated intensity map (Fig. 4) is only available in electronic form at the CDS via anonymous ftp to cdsarc.u-strasbg.fr (130.79.128.5) or via <http://cdsweb.u-strasbg.fr/cgi-bin/qcat?J/A+A/>. All spectra can be obtained upon request to the authors.

ular components (referred to as the Hot Core, Compact and Extended Ridges) and several IR sources or radio sources are associated with Orion-KL. The nature of the source(s) responsible for this IR emission is still poorly known and much debated. Many young stellar objects are still embedded in the dusty gas, including radio source I, a deeply embedded, high-mass young stellar object, which drives a bipolar outflow along a northeast-southwest axis (Beuther et al. 2005; Goddi et al. 2009; Plambeck et al. 2009) and presents a disk perpendicular to it (Matthews et al. 2010).

Another specificity of the Orion protocluster region is the presence of high speed shocks generated in the center of Orion-KL, reminiscent of an explosive event. From VLA velocity measurements, it was proposed that a very unique phenomenon had taken place some 500-1000 years ago: the close encounter, or collision, of two or more rather massive stars. The objects involved in such a dynamical interaction could have included the Becklin-Neugebauer object (BN) and sources I and n (Gómez et al. 2005; Rodríguez et al. 2005; Goddi et al. 2010). We might thus be observing a very recent and energetic event at the heart of the nebula, providing unique conditions for the study of a rich interstellar chemistry. With this scheme in mind, many molecules could have thus been released from the grain mantles because of dust heating or multiple shocks.

The search for complex or prebiotic molecules is difficult because of their relatively low abundance and line intensity. Especially in a very rich molecular source such as Orion-KL, high spectral confusion makes it difficult to detect the weakest lines. Among them, glycine (NH₂CH₂COOH, the simplest amino acid) has been searched for in the interstellar medium by many groups but has not been detected and only upper limits are given by the most sensitive studies (e.g. Combes et al. 1996; Guélin et al. 2008; Snyder et al. 2005). On the other hand, observing abundant complex molecules is necessary to characterize the gas temperature and density of the various Orion-KL molecular source components. Observations of O- and N-bearing molecules show a clearly different spatial distribution. N-bearing molecules tend to peak to the north of the Hot Core while O-bearing molecules cover the Hot Core and the Compact Ridge (Guélin et al. 2008; Beuther et al. 2005; Friedel & Snyder 2008).

Rotational temperature maps have been derived from interferometric observations of CH₃OH (Beuther et al. 2005), NH₃ (Wilson et al. 2000), both essentially focused on the Hot Core, and CH₃CN (Wang et al. 2010); the intense lines of these abundant species require however to correct for opacity effects. Several single dish observations (e.g. Blake et al. 1987; Comito et al. 2005) were also used to derive rotational temperatures towards the Hot Core and the Compact Ridge, which are supposed to be differentiated from their velocity structure. The spatial structure is lacking in these data, however.

In this paper we investigate the spatial structure and temperature distribution of Orion-KL from observations of the O-bearing methyl formate (HCOOCH₃) molecule, which is relatively abundant in several interstellar hot cores and corinos, and especially abundant in Orion-KL (Blake et al. 1987; Kobayashi et al. 2007; Friedel & Snyder 2008). In Sect. 2 we present our observations and the methyl formate frequency data base used in this work and we briefly describe the data reduction methodology. The results of our maps are presented in Sect. 3 together with details on the various molecular emission peaks identified in our maps. In Sect. 4, the temperature and molecular abundance across the entire V-shaped molecular structure linking IRc2 to BN are deduced from the rotational diagrams of the

methyl formate molecule. In Sect. 5, upper limits on the abundance of methyl formate isomers are given. The dust and total mass and the mean gas density of the most prominent dust emission peaks are estimated from our continuum data in Section 6. The methyl formate fractional abundance is also estimated and briefly discussed in this same Section. We compare our results to previous studies in Section 7. In Sect. 8, the methyl formate distribution is discussed in the light of the complex structure of the Orion nebula. Conclusions are presented in the last Section.

2. Observations and methyl formate frequencies

2.1. Observations

We used twelve observational data sets obtained with the IRAM Plateau de Bure Interferometer (PdBI) towards the IRc2 region and its surroundings between 1996 and 2007. The bulk of the observations were obtained between 1999 and 2007. Table 1 lists the different parameters for each data set. The highest spatial resolution (1.79'' × 0.79'') was achieved in the period 2003 to 2007. Most observations used five antennas which were equipped with two SIS receivers operated simultaneously at 3mm and 1mm until 2006, then independently. 0420-014, 0458-020, 0528+134, 0605-085 and 0607-157 were used as phase and amplitude calibrators. The short-term atmospheric phase fluctuations were corrected at 1.3 mm on line. Tropospheric and radiometric phase corrections have been used since 1995 and October 2001, respectively, at the IRAM PdBI, based on the measured water line wings in the continuum emission observed with the 1.3 mm receiver and on the 22 GHz water line radiometers. The six units of the correlator allowed us to observe several data subsets with different bandwidths and spectral resolution which are also given in Table 1. For the highest spatial resolution the spectral resolution was around 0.84 km s⁻¹ while some lower spatial resolution maps were obtained with 0.42 km s⁻¹ spectral resolution. The *uv* coverage of these two data sets is shown in figure 1.

2.2. Data reduction

We used the GILDAS package¹ for data reduction. The continuum emission was subtracted in the data cubes by selecting line-free channels, discarding any contaminated (or doubtful) channels. Continuum emission in Orion-KL is essentially due to the thermal emission from the dust and to a weaker contribution from the free-free radiation of the gas. However, the contribution from the pseudo-continuum resulting from the superposition of many weak lines cannot be easily removed as it may depend on the spectral range analysed. The continuum emission is strong and spatially extended, varies with frequency, and reveals a clumpy structure at the highest spatial resolutions (see Fig.2 and Fig.16). As the center of the observations is not the same for all data sets, the continuum emission is better mapped toward the South at 223 GHz and toward the North at 225 GHz. Mapping the continuum emission is not obvious because of the high density of lines. It is difficult to isolate channels devoid of molecular lines. Nevertheless, we have been able to identify several channels (typically 4 to 22 by data sets) without line emission in our observations. All of these channels have been averaged and the average subtracted from each channel in the data cubes.

Finally, we have cleaned the data cubes, channel by channel, using the Clark method. Columns 9, 10 and 11 in Table 1 summarize the synthesized beam parameters for each dataset.

¹ <http://www.iram.fr/IRAMFR/GILDAS>

Table 1. Main parameters of IRAM Plateau de Bure interferometer observations.

Set ^a	Bandwidth (GHz)	Date of observation ^b	Confi- guration (4)	HPBW (^c)	Spectral resolution (MHz)	(km s ⁻¹) (7)	Flux conversion (1 Jy beam ⁻¹) (8)	Synthesized beam (^c × ^c) (9)	PA (°) (10)	Pixel size (^c × ^c) (11)
(1)	(2)	(3)	(4)	(5)	(6)	(7)	(8)	(9)	(10)	(11)
1	80.502 - 80.574	10-11/1999	CD	60	0.625	2.33	4.6 K	7.63 × 5.35	15	0.80 × 0.80
2	80.582 - 80.654	10-11/1999	CD	60	0.625	2.33	4.7 K	7.62 × 5.23	16	0.96 × 0.96
3	101.178 - 101.717	^c	BC	50	0.625	1.85	15.8 K	3.79 × 1.99	22	0.50 × 0.50
4	105.655 - 105.726	08-11/2005	D	48	0.3125	0.89	2.9 K	7.13 × 5.36	9	1.40 × 1.40
5	105.785 - 105.856	08-11/2005	D	48	0.3125	0.89	2.9 K	7.12 × 5.36	9	1.40 × 1.40
6	110.125 - 110.181	10/1996	C	46	0.15625	0.43	8.5 K	5.85 × 2.02	8	0.54 × 0.54
7	203.331 - 203.403	10-11/1999	CD	25	0.625	0.92	7.0 K	2.94 × 1.44	27	0.38 × 0.38
8	203.411 - 203.483	10-11/1999	CD	25	0.625	0.92	7.0 K	2.94 × 1.44	27	0.32 × 0.32
9	223.402 - 223.941	^d	BC	23	0.625	0.84	17.3 K	1.79 × 0.79	14	0.25 × 0.25
10	225.675 - 225.747	09-11/2005	D	22	0.3125	0.42	2.9 K	3.63 × 2.26	12	0.70 × 0.70
11	225.805 - 225.942	09-11/2005	D	22	0.3125	0.42	2.9 K	3.63 × 2.26	12	0.70 × 0.70
12	225.990 - 226.192	09-11/2005	D	22	0.3125	0.42	2.9 K	3.63 × 2.25	12	0.70 × 0.70

^a Sets 3 and 9 were centered on coordinates ($\alpha_{J2000} = 05^h35^m14^s.20$, $\delta_{J2000} = -05^\circ22'36''.00$). Sets 1, 2, 4, 5, 6, 7, 8, 10, 11 and 12 were centered on coordinates ($\alpha_{J2000} = 05^h35^m14^s.46$, $\delta_{J2000} = -05^\circ22'30''.59$). The observation velocity was 6 km s⁻¹ for sets 1, 2, 6, 7, 8 and 8 km s⁻¹ for the other sets.

^b Format: Month-Month/Year.

^c Dates of observation: 12/2003, 01-12/2004, 03/2005, 01/2006.

^d Dates of observation: 12/2003, 01-12/2004, 03/2005, 01/2006, 11-12/2007.

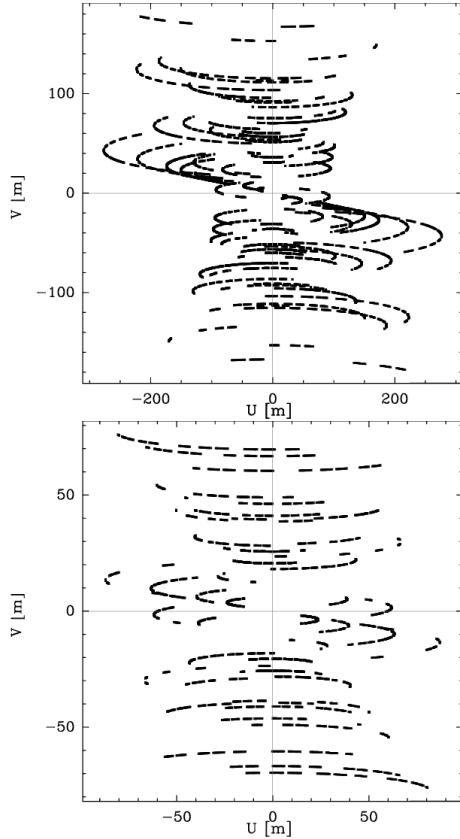


Fig. 1. Resulting uv coverage from the six tracks at 223 GHz (top panel) and four tracks at 225 GHz (bottom panel).

2.3. Interest of methyl formate observations

Methyl formate, one of three [C₂H₄O₂] isomers, is relatively abundant towards Orion-KL, in view of its complexity. High angular resolution allows us 1) to isolate the different emission peaks of methyl formate and to investigate the gas structure, 2) and with large scale maps, to understand the overall

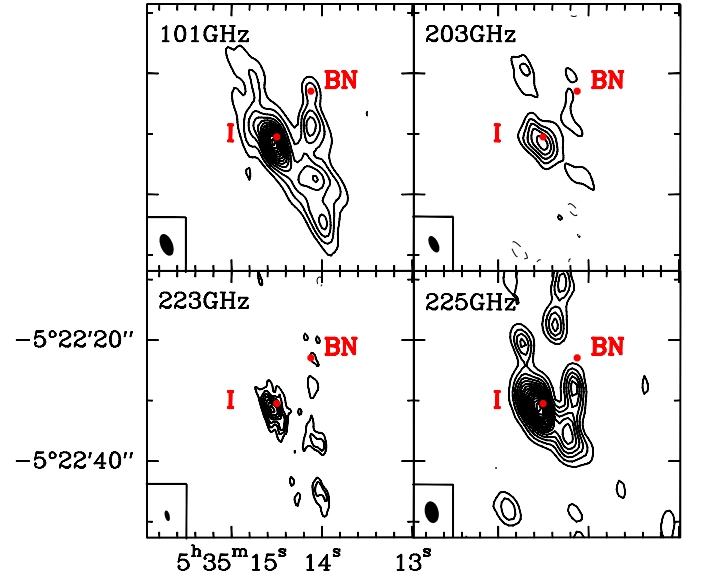


Fig. 2. Continuum maps obtained toward Orion-KL with the Plateau de Bure Interferometer. The clean beam is shown in the bottom left corner of each map. The first contour and the level step are 15 mJy beam⁻¹, 170 mJy beam⁻¹, 70 mJy beam⁻¹ and 100 mJy beam⁻¹ at 101.45 GHz, 203.41 GHz, 223.67 GHz and 225.90 GHz respectively. In each map, positions of the BN object ($\alpha_{J2000} = 05^h35^m14^s.1094$, $\delta_{J2000} = -05^\circ22'22''.724$) and the radio source I ($\alpha_{J2000} = 05^h35^m14^s.5141$, $\delta_{J2000} = -05^\circ22'30''.575$) (Goddi et al. 2010) are indicated. Note that the maps have not been observed with the same center (see table 1).

Orion nebula structure (as discussed later in Section 8 of this work). High angular resolution also lowers the risk of spectral contamination by line-rich species such as C₂H₅CN, because the methyl formate distribution is different from that of N-bearing molecules (Blake et al. 1987; Kobayashi et al. 2007; Friedel & Snyder 2008).

Methyl formate presents close rotational transitions (see Fig.3) with strong line strengths ($S\mu^2$ up to 50.2 D² in our se-

lection, see Tables 10 and A.4). Several transitions covering an important range of energy can be observed at the same time. Comparison of these data obtained with identical spatial and spectral resolutions will allow an optimal estimate of the molecular gas physical conditions. The observed lines are all optically thin, which ease greatly their interpretation.

From a chemical point of view, formation of methyl formate on grain surfaces or in gas phase is still debated, as for many other complex species. The study of its spatial distribution, and its relative abundance with respect to other O-bearing molecules like methanol CH₃OH, dimethyl ether CH₃OCH₃ and the two methyl formate isomers, glycolaldehyde CH₂OHCHO and acetic acid CH₃COOH, could help evaluate the different chemical models (Charnley & Rodgers 2005; Bisschop et al. 2007; Garrod & Herbst 2006; Garrod et al. 2008).

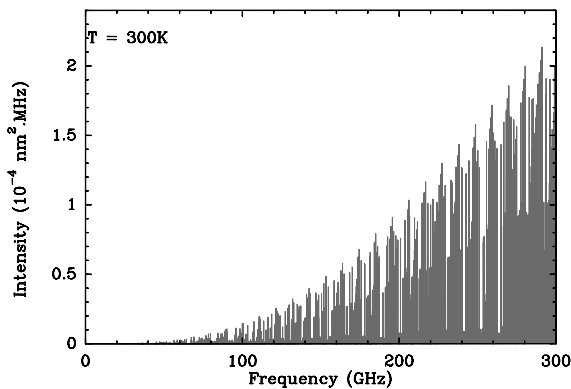


Fig. 3. Methyl formate (HCOOCH₃) line intensities assuming LTE and a temperature of 300 K (sources : JPL database and Ilyushin et al. 2009).

2.4. Methyl formate and isomers frequencies

Recently, Ilyushin et al. (2009) recalculated the rotational transitions of HCOOCH₃ for the ground and first excited torsional states of this molecule. The JPL database² (Pickett 1991; Pickett et al. 1998) is now updated (since April 2009) to include both the newly recalculated methyl formate frequencies and their own predictions (Drouin, B.J.). The methyl group, because of its three-fold internal rotation, leads to a series of thermally populated torsional levels which are split into two torsional substates with A and E symmetries. Previous data separated these two states while current data treat both substates simultaneously. In our study, we use the measured and predicted transitions coming from both Ilyushin's table and the JPL database up to $E_{\text{upper}} \lesssim 650$ K. Assuming HCOOCH₃ lines are thermalized, we take into account transitions in their fundamental and first excited torsional states $v_t = 0$ and $v_t = 1$, respectively. Our observations confirm the detection of transitions of methyl formate in the first torsionally excited state (Kobayashi et al. 2007).

We also searched for the methyl formate isomers (see Sect. 5) and used Ilyushin et al. (2008) for the acetic acid and the CDMS database³ (Müller et al. 2001, 2005) for the glycolaldehyde transitions.

3. Mapping methyl formate emission (HCOOCH₃) with the IRAM interferometer

The methyl formate molecule, HCOOCH₃, allows us to trace the spatial distribution of one major oxygenated molecule in Orion-KL, especially in the direction of the Compact Ridge where high spatial resolution data are missing. We have adopted the Hot Core and Compact Ridge positions labelled in Beuther et al. (2005). Figure 4 shows our large scale, 1.79'' × 0.79'' beam size interferometric map of the HCOOCH₃ line emission integrated over the line profile and on three different transitions: 11_{4,8}-10_{3,7} A and E in $v_t = 0$ and 18_{5,14}-17_{5,13} E in $v_t = 1$ (at 223465.340 MHz, 223500.463 MHz and 223534.727 MHz respectively) to improve the signal to noise ratio. It shows: (a) several main emission peaks labeled MF1 to MF28, and (b) an extended, V-shaped molecular emission linking the radio source I to the BN object.

3.1. Molecular emission peaks

We used the whole data set obtained with different frequencies and angular resolutions to model and investigate the properties of the methyl formate emission. The molecular emission peaks (MF1 to MF28) were determined from our highest angular resolution data (1.79'' × 0.79'') on the channel maps when they are present on *at least three adjacent channels*; they are listed in Table 2. The individual positions can vary by one pixel (0.25'') depending on the HCOOCH₃ transition. Two main molecular peaks, MF1 and MF2, are located toward the Compact Ridge and the Hot Core-SW respectively (e.g references taken from Beuther et al. 2005; Friedel & Snyder 2008). Emission peaks are present throughout the observed field and exhibit more or less extended structures. At some frequencies a molecular emission is also detected at the position of the millimeter source MM23 (Eisner et al. 2008).

The molecular emission peaks MF1, MF2, MF4-5 and MM23 are associated with the 4 main dust peaks identified at 223 GHz (see Fig. 16 in Sect. 6). However the continuum emission does not coincide exactly with the associated molecular line peak ($\Delta\alpha \sim 0.1''$ to $1.2''$ and $\Delta\delta \sim 0.03''$ to $1.8''$, except for MF2 where $\Delta\alpha = 1.8''$ and $\Delta\delta = 2.9''$, for a beam size of $1.8'' \times 0.8''$). Since both continuum and line maps come from the same data sets the observed spatial separations cannot be ascribed to instrumental effects. de Vicente et al. (2002) report the same effect from their HC₃N (10-9) lines observed in different vibrational levels. We conclude that even our best resolution is probably not sufficient to determine exactly the relative positions of molecular and dust emissions.

3.2. Velocity structure

Figure 5 presents the channel maps of the 223465.340 MHz line. Most of the peaks appear between 6 and 9 km s⁻¹. However a linear structure is seen mainly toward the North at higher velocities (see discussion on MF1 and MF4 peaks in Sect. 3.5); it goes from MF5 to MF8. There is no methyl formate emission at the Hot Core position at the usual 5 km s⁻¹ velocity.

3.3. Critical density

We assumed that the HCOOCH₃ transitions are thermalized at the five molecular emission peaks MF1 to MF5. From the H₂ column densities measured at the continuum peaks associated

² <http://spec.jpl.nasa.gov/home.html>

³ <http://www.astro.uni-koeln.de/cdms>

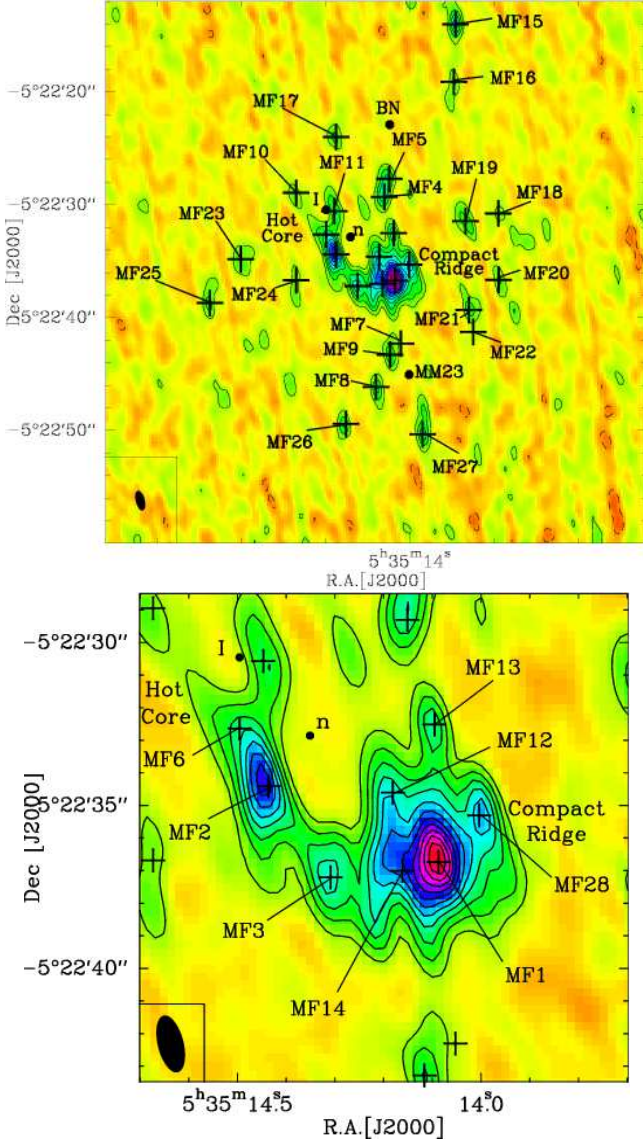


Fig. 4. Methyl formate integrated intensity maps obtained with the Plateau de Bure Interferometer (sum of emission at 223465.340 MHz, 223500.463 MHz and 223534.727 MHz between 5 and 12 km s⁻¹). The bottom image is a blowup of the Hot Core/Compact Ridge map area. The beam is 1.79'' × 0.79''; the level step and first contour are 3.2 K km s⁻¹. The BN object position is ($\alpha_{J2000} = 05^h35^m14^s.1094$, $\delta_{J2000} = -05^\circ22'22''.724$), the radio source I position is ($\alpha_{J2000} = 05^h35^m14^s.5141$, $\delta_{J2000} = -05^\circ22'30''.575$) and the IR source n position is ($\alpha_{J2000} = 05^h35^m14^s.3571$, $\delta_{J2000} = -05^\circ22'32''.719$) (Goddi et al. 2010). The position of the millimetre source MM23 (Eisner et al. 2008) is also indicated. The main different HCOOCH₃ emission peaks identified on channel maps are marked by a cross and labelled MF_{NUMBER}.

to those positions (see Sect. 6 and Table 7) we find indeed $n_{\text{H}_2} \gg n_{\text{cr}} \sim 10^{4-7} \text{ cm}^{-3}$ for the detected lines at frequencies between 80 GHz and 226 GHz. To compute n_{cr} , we have adopted the collision coefficients of H₂O (Faure & Josselin 2008) because of a similar dipole moment to HCOOCH₃ ($\mu = 1.8 \text{ D}$), and we have taken into account a multiplicative factor between 1 and 10 because HCOOCH₃ is a larger molecule. Even if n_{cr}

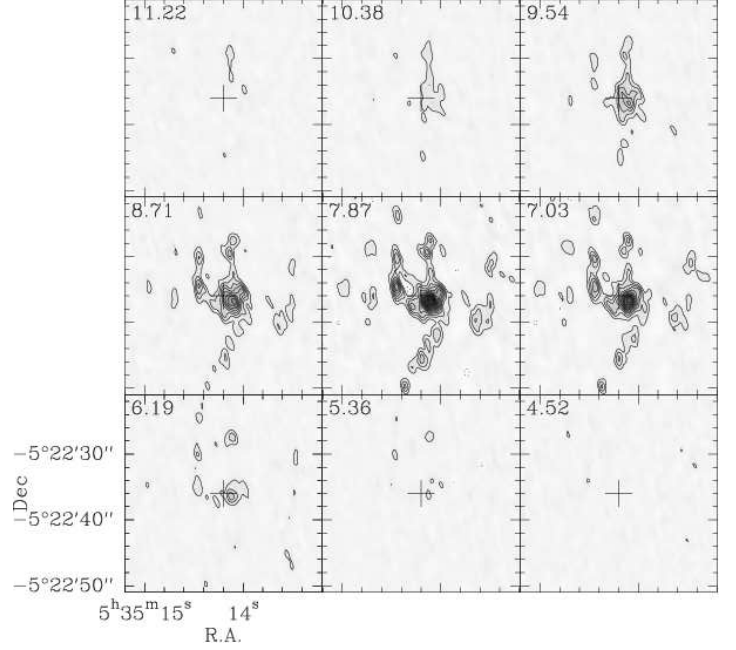


Fig. 5. Methyl formate channel maps of emission at 223465.340 MHz. The beam is 1.79'' × 0.79'' and the first contour and level step are 50 mJy beam⁻¹. The v_{LSR} velocity is indicated on each plot.

would reach 10⁷ cm⁻³ the critical density remains well below n_{H_2} (see Table 7).

3.4. Missing flux estimation

To estimate whether there is some flux missing in our data due to spatial filtering with the PdBI interferometer we have compared our PdBI spectra at 3 mm and 1 mm with IRAM 30-m telescope spectra. The PdBI spectra have been convolved with a Gaussian beam similar to the 30-m beam (25'' at 3 mm and 11'' at 1 mm). For all data sets the convolution was performed at the positions observed with the 30-m telescope. Error bars arising from the calibration and the pointing of the 30-m antenna fall within the typical range of 5–10 %.

In the Compact Ridge, comparison of our PdBI observations (which have a spatial resolution of 3.79'' × 1.99'' at the relevant frequencies) with the 30-m observations made at 101 GHz (Combes et al. 1996) indicates a ratio of missing flux of 3% and 15% measured from lines at 101370.505 MHz (13_{3,11}-13_{2,12}, E) and 101414.746 MHz (13_{3,11}-13_{2,12}, A) respectively. At 101477.421 MHz the 18_{3,15}-18_{3,16}E line is strongly blended with an intense H₂CS transition (see Fig 6).

Concerning the Hot Core position, we also compared our PdBI observations (spatial resolution: 1.79'' × 0.79'') with the 30-m observations made at 223 GHz (J. Cernicharo, private communication). Chemically, this region exhibits an important molecular diversity implying a very high confusion level. All HCOOCH₃ lines are blended either with another strong molecule or with a multitude of weaker lines, which makes it difficult to measure the exact missing flux. Using the 223500.463 MHz (11_{4,8}-10_{3,7}, A) line, we find that about 20% of the flux is missed. At 3 mm we estimate that we can miss between 4% and 15% of methyl formate emission flux; this is determined from the lines at 101302.159 MHz (25_{6,19}-25_{5,20}, A) and 101370.505 MHz (13_{3,11}-13_{2,12}, E).

Table 2. Position of the main HCOOCH₃ emission peaks observed with the Plateau de Bure Interferometer toward Orion-KL.

Position name	R.A (J2000)	Dec (J2000)
	05 ^h 35 ^m	-05°22'
MF1	14:09	36:7
MF2	14:44	34:4
MF3	14:31	37:2
MF4	14:15	29:3
MF5	14:12	27:7
MF6	14:50	32:6
MF7	14:05	42:3
MF8	14:20	46:1
MF9	14:11	43:3
MF10	14:68	28:9
MF11	14:45	30:6
MF12	14:18	34:6
MF13	14:09	32:5
MF14	14:16	37:0
MF15	13:72	14:0
MF16	13:73	19:1
MF17	14:44	24:0
MF18	13:46	30:8
MF19	13:66	31:5
MF20	13:46	36:6
MF21	13:64	39:3
MF22	13:61	41:3
MF23	15:01	34:8
MF24	14:68	36:7
MF25	15:20	38:7
MF26	14:38	49:4
MF27	13:92	50:3
MF28	14:00	35:3

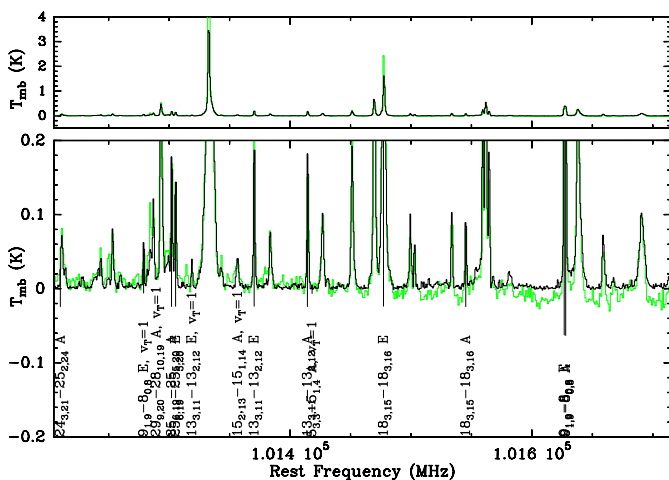


Fig. 6. Spectra of molecular emission at 3 mm toward the Compact Ridge. The lower panel is a blow up of the upper one. Green lines show IRAM 30-m telescope data of Combes et al. (1996) and black lines illustrate PdBI data (set n°3, see table 1) convolved with the 30-m beam. A and E transitions of HCOOCH₃ are marked on the figure.

3.5. Observed parameters of the different HCOOCH₃ peaks

Supposing that the gas rotational temperature does not exceed a few hundred Kelvin, we have searched for the 64 methyl formate transitions with $E_{\text{upper}} \lesssim 650$ K. We have used the MAPPING GILDAS software to map and model the methyl formate source sizes, and the CLASS GILDAS software to determine the line

parameters. The line frequencies, spectroscopic and observed parameters (ν , $\Delta v_{1/2}$, T_B , W) at the MF1 to MF5 emission peaks are given in Tables 10 to A.4. The observational results are briefly summarized below for the main molecular peaks shown in Figure 4.

MF1 is the main HCOOCH₃ emission peak toward the Compact Ridge. It is present in all maps of detected HCOOCH₃ transitions. The source sizes, estimated at half-peak flux density (see Table 10), increase with a lower spatial resolution from $3.0'' \times 2.0''$ at 223 GHz to $7.0'' \times 10.0''$ at 80 GHz. The line width clearly depends on the spatial and spectral resolutions. For instance, with the same beam ($\approx 3'' \times 2''$) but using two different spectral resolutions, 1.85 km s⁻¹ and 0.42 km s⁻¹, we obtain $\Delta v \approx 3.6$ km s⁻¹ and 1.1 km s⁻¹, respectively. Table 10 summarizes the line parameters for all detected, blended or not detected transitions in all data sets. We detected 20 lines, and observed 2 partially blended and 33 blended lines; 9 transitions were too faint to be detected. At both high spatial and spectral resolutions the 203 GHz, 223 GHz and 225 GHz methyl formate spectra display two components, one around 7.5 km s⁻¹ and the other around 9 km s⁻¹ (see fig. 7). The 2-velocity fit parameters are presented in Table 3. Both components have a narrow average line width of $\Delta v_{1/2} \approx 1.7$ km s⁻¹. For the transitions observed with less resolution the second velocity component cannot be directly separated and the line widths are broader ($\Delta v_{1/2} \approx 3.6$ km s⁻¹).

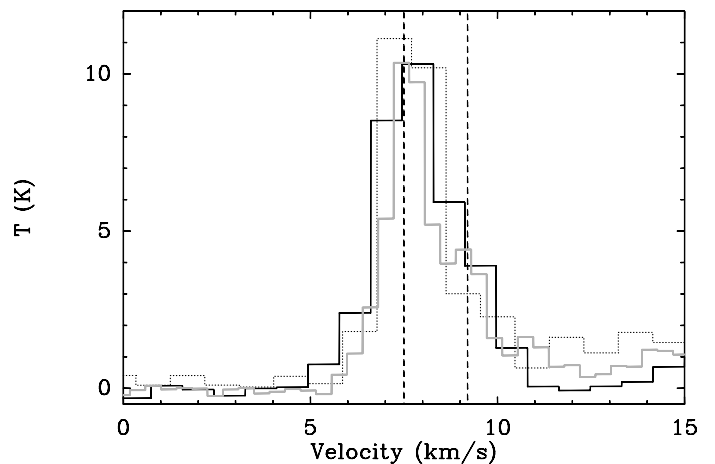


Fig. 7. Two HCOOCH₃ components observed on the emission peak MF1 toward the Compact Ridge. The black spectrum shows the 223465.340 MHz line, the grey spectrum the 225855.505 MHz transition and the dotted line spectrum the 203435.554 MHz transition. The intensity of the 2 latter spectra is multiplied by a factor 1.5 and 2 respectively. Dash lines mark $v_{\text{LSR}} = 7.5$ and 9.2 km s⁻¹.

MF2 is the main HCOOCH₃ emission peak toward the Hot Core region. This peak is present in all detected HCOOCH₃ transitions. The source sizes, estimated at half-peak flux density (see Table A.1 in Appendix A) increases with a lower spatial resolution from $2.5'' \times 1.2''$ at 223 GHz to $5.0'' \times 2.5''$ at 101 GHz⁴. This source appears to be more compact than MF1 in the

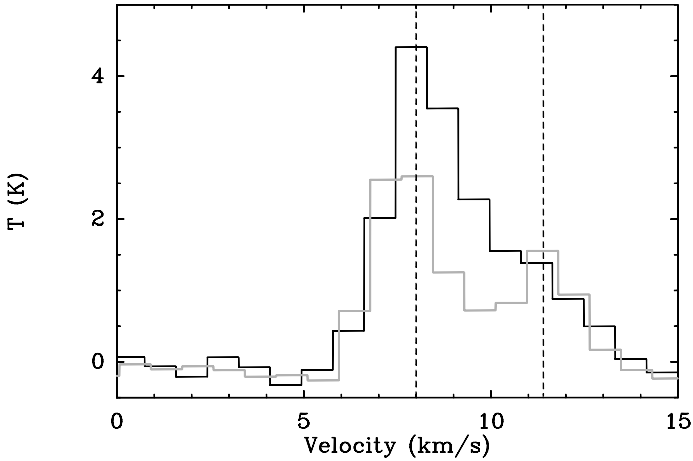
⁴ Note that the lower spatial resolution of the detected lines at 80565.210 MHz and 105815.953 MHz does not allow us to identify individual sources.

Table 3. Two-component analysis of methyl formate transitions observed with the IRAM Plateau de Bure Interferometer toward position MF1 in the Compact Ridge. For the definition of the parameters see Table 10

Frequency (MHz)	Transition	E_{up} (K)	$S\mu^2$ (D ²)	sigma (K)	Component 1				Component 2			
					v_1 (km s ⁻¹)	$(\Delta v_{1/2})_1$ (km s ⁻¹)	T_{B1} (K)	W_1 (K km s ⁻¹)	v_2 (km s ⁻¹)	$(\Delta v_{1/2})_2$ (km s ⁻¹)	T_{B2} (K)	W_2 (K km s ⁻¹)
203435.554	19 _{8,11} – 19 _{7,12} A	155	5.3	0.09	7.6(0.9)	1.6(0.9)	6.40	10.6(1.6)	9.3(0.9)	2.2(0.9)	0.88	2.1(1.6)
203471.840	19 _{8,11} – 19 _{7,12} E	155	4.9	0.09	7.5(0.1)	1.6(0.1)	5.28	9.2(2.0)	9.0(0.7)	3.1(1.0)	1.29	4.3(2.2)
223465.340	11 _{4,8} – 10 _{3,7} E	50	2.1	0.17	7.6(0.1)	2.0(0.2)	10.74	22.5(1.9)	9.5(0.2)	1.5(0.3)	3.17	5.0(1.7)
223500.463	11 _{4,8} – 10 _{3,7} A	50	1.8	0.17	7.4(0.1)	1.8(0.1)	11.49	21.8(1.7)	9.2(0.3)	1.9(0.4)	2.85	5.8(1.2)
223534.727	18 _{5,14} – 17 _{5,13} E, ($v_t=1$)	305	41.6	0.17	7.4(0.1)	1.7(0.1)	10.25	18.5(0.8)	8.9(0.1)	2.9(0.2)	4.16	13.0(8.2)
225855.505	6 _{6,1} – 5 _{5,1} E	36	3.1	0.10	7.6(0.1)	1.2(0.1)	6.84	9.1(0.1)	9.2(0.1)	1.1(0.1)	2.56	2.9(0.1)
225999.145	30 _{7,23} – 29 _{8,22} E	312	2.2	0.11	7.5(0.1)	0.9(0.3)	0.70	0.6(0.2)	9.1(0.1)	0.8(0.3)	0.45	0.4(0.1)

Table 4. Two-component analysis of methyl formate transitions observed with the IRAM Plateau de Bure Interferometer toward position MF4. For the definition of the parameters see Table A.3 (in Appendix A).

Frequency (MHz)	Transition	E_{up} (K)	$S\mu^2$ (D ²)	sigma (K)	Component 1				Component 2			
					v_1 (km s ⁻¹)	$(\Delta v_{1/2})_1$ (km s ⁻¹)	T_{B1} (K)	W_1 (K km s ⁻¹)	v_2 (km s ⁻¹)	$(\Delta v_{1/2})_2$ (km s ⁻¹)	T_{B2} (K)	W_2 (K km s ⁻¹)
223465.340	11 _{4,8} – 10 _{3,7} E	50	2.1	0.17	8.0(0.1)	1.9(0.3)	3.83	7.7(2.5)	10.2(0.8)	3.7(1.0)	1.66	6.6(2.7)
223500.463	11 _{4,8} – 10 _{3,7} A	50	1.8	0.17	8.0(0.1)	2.2(0.2)	1.90	4.4(0.4)	11.4(0.2)	2.2(0.3)	1.29	3.0(0.4)
223534.727	18 _{5,14} – 17 _{5,13} E, ($v_t=1$)	305	41.6	0.17	8.7(0.3)	3.0(0.4)	1.78	5.8(0.8)	11.0(0.4)	5.3(0.8)	1.34	7.6(0.9)

**Fig. 8.** Two HCOOCH₃ components observed toward the emission peak MF4. The black spectrum shows the 223465.340 MHz transition and the grey spectrum the 223500.463 MHz transition. Dash lines mark $v_{\text{LSR}} = 8.0$ and 11.4 km s⁻¹.

Compact Ridge. Table A.1 (in Appendix A) summarizes the line parameters for all detected, blended or not detected transitions in all data sets. We detected 14 lines and observed 3 partially blended and 40 blended lines; 7 transitions were too faint to be detected. The mean velocity is around 7.7 km s⁻¹. As for clump MF1 the line widths depend on the spatial and spectral resolutions. With the highest spatial resolution ($1.79'' \times 0.79''$) we find $\Delta v_{1/2} \approx 2.4$ km s⁻¹ while for a resolution of $3.79'' \times 1.99''$, $\Delta v_{1/2} \approx 4.1$ km s⁻¹; we did not take into account the partially blended line at 226061.796 GHz. The linewidths observed here are slightly broader than those of components 1 and 2 at the MF1

peak; as the lines are optically thin (see Sect. 4) this indicates a larger velocity spread in the source.

MF3 is a HCOOCH₃ emission peak located in-between the two previous clumps. It often appears as an extension of the emission as most of our data do not allow us to isolate the emission peak. As for clumps MF1 and MF2, the linewidth is narrow; at 203 GHz and 223 GHz $\Delta v_{1/2} \approx 1.7$ km s⁻¹. Table A.2 (in Appendix A) summarizes the line parameters for all detected, blended or not detected transitions in all data sets. We detected 14 lines, and observed 3 partially blended and 26 blended lines; 21 transitions were too faint to be detected. The methyl formate velocity is around 7.7 km s⁻¹.

MF4 is one of the main HCOOCH₃ emission peaks lying at the North of the Compact Ridge. Table A.3 (in Appendix A) summarizes the line parameters for all detected, blended or not detected transitions in all data sets. We detected 9 lines, and observed 4 partially blended and 28 blended lines; 23 transitions were too faint to be detected. As for clump MF1 the high spectral resolution line profiles show two components (see fig. 8). The 223 GHz methyl formate emission profiles are fitted with two components centered around 8.0 km s⁻¹ and 11.4 km s⁻¹ (Table 4). Both components have linewidths in the range ($\Delta v_{1/2} \approx 1.9 - 3.7$ km s⁻¹).

MF5 lies near the emission peak MF4 and its size is similar to that of MF4. Two velocity components, visible with high spectral resolution only, are present in our data. However, we have not made any precise velocity identification of these components because they are more blended than those identified in the direction of MF4 and MF1. The unresolved emission is centered around 7.7 km s⁻¹. We detected 9 methyl formate transitions and

observed 3 partially blended and 28 blended lines. 24 other lines were too faint to be detected. All results from all data sets are summarized in Table A.4 (in Appendix A).

3.6. Fraction of blended and detected lines

We have mentioned earlier that spectral confusion is a major problem toward Orion-KL. Confusion increases with frequency and it is more prevalent in our data at 223 GHz–225 GHz than at 101 GHz. Spectral confusion is present to some extent toward all the emission peaks identified in this work (MF1 to MF28).

We present here a rough estimate of the confusion level. From a visual inspection of our spectra, we believe that some line frequencies are contaminated by other lines, and noted a priori as *blended*, whereas at other line frequencies the spectrum appears *free of contamination*. To determine which lines are detectable in our data set we use the simple one-temperature model derived in Section 4 and compare the expected line intensity to the noise level. Of the n_d detectable lines, a number, n_{db} , are blended whereas $n_{df} = n_d - n_{db}$ others appear free of contamination.

For sources MF1, MF2 and MF3 all lines expected above 3 sigma and free of contamination are detected; this is a consistency check of the LTE model. To roughly quantify the effect of confusion in these sources we compute $\eta_D = n_{df}/n_d$. We obtain the following results for temperatures derived from our rotational diagrams (see following Section):

- $\eta_D = 49\%$ at the MF1 peak for $T = 79$ K,
- $\eta_D = 40\%$ at the MF2 peak for $T = 130$ K,
- $\eta_D = 30\%$ at the MF3 peak for $T = 85$ K

For sources MF4 and MF5, the presence of two velocity components makes the methyl formate lines broader and more difficult to detect. The number of detected lines is thus more imprecise, as for example some broad lines may be classified as blended instead of broadened by the dynamics. We get $\eta_D = 13 - 20\%$ which is coherent with an increase of the confusion for broader lines. Some of the fainter lines expected to be detectable from the LTE model are not seen, especially in the data cubes around 225 GHz, which we attribute to an increased interferometric filtering of the quasi vertical MF4-MF5 structure in these cubes (compare the two uv coverages in Fig. 1).

The meaning of η_D should not be overinterpreted because i) it depends on the LTE hypothesis, on the derived column density and temperature values and on the expected line profile; ii) it is not intrinsic to a molecule in a given source as it depends also on the frequency range and other observation parameters (noise level, spectral and spatial resolution, uv coverage). Note in addition that in the case of our dataset, the latter parameters vary from one datacube to another, so that η_D is only an average value. It is however a first indication of the relative importance of the confusion problem - a similar indicator was given by Belloche et al. (2008) for their search and detection of amino acetonitrile in Sgr B2(N).

4. Temperatures and abundance of methyl formate towards the whole molecular V-shape

From Rohlfs & Wilson (2000) the opacity at the line center can be calculated from:

$$\tau = -\ln\left(1 - \frac{\Delta T_{mb}}{J(T_r) - J(T_{continuum}) - J(T_{bg})}\right) \quad (1)$$

where,

ΔT_{mb}	is the excess brightness temperature observed on spectra,
$J(T_r)$	the source function of the rotational brightness temperature,
$J(T_{continuum})$	the source function of the continuum brightness temperature,
$J(T_{bg})$	the source function of the 2.7 K background brightness temperature.

We assumed that all the lines are optically thin (calculated opacities are generally less than 0.05 and at most 0.1) and that the local thermodynamic equilibrium is reached for all positions (see Sect. 3.3), so that the kinetic temperature is equal to the excitation, rotational and vibrational temperatures. We estimated the rotational temperature and the column density of HCOOCH₃ using the equation (Turner 1991):

$$\ln\left(\frac{3k_B W}{8\pi^3 \nu S \mu^2 g_i g_k}\right) = \ln\left(\frac{N}{Q}\right) - \frac{E_{up}}{k_B T} \quad (2)$$

where,

W	is the integrated line intensity (K km s ⁻¹),
ν	the line frequency (Hz),
$S \mu^2$	the line strength (D ²),
g_i	the reduced nuclear spin statistical weight,
g_k	the K-level degeneracy,
N	the total column density,
Q	the partition function,
E_{up}	the upper state energy,
T	the excitation temperature.

Due to the CH₃ group methyl formate is divided into two forms: A and E. Turner (1991) indicates that for A species: $g_i = 2$ and $g_k = 1$, and inversely for E species. We used $g_i g_k = 2$ for all the transition lines.

We have made the rotational diagrams for two different spatial resolutions. One is based on the data with the highest spatial resolution (synthesized beam of 1.79'' × 0.79'' at 223 GHz). The other one includes data at 101 GHz, 203 GHz and 225 GHz where the two first data sets are smoothed to the resolution of the third one (synthesized beam of 3.63'' × 2.26'') for the MF1 emission peak. The rotational temperatures and column density uncertainties, estimated by a least-square fit, are only based on the statistical weight of the detection measurements⁵ (upper limits are not taken into account by the fit). The derived column densities are corrected for the beam filling factor.

Rotational diagram at the MF1 peak

We have made a rotational diagram for each velocity component. Figure 9 displays the diagrams obtained with the data at a 1.79'' × 0.79'' resolution (see set n°9 in Table 1) and figure 10 the diagrams obtained with the data at a 3.63'' × 2.26'' resolution (see sets 7, 8, 10, 11 and 12 in Table 1). They show that the temperature of the 9.2 km s⁻¹ component is higher (112±50 K at high resolution and 168±30 K at a lower resolution) than that of the 7.6 km s⁻¹ component (79±2 K at high resolution and

⁵ Error bars reflect only the uncertainties in the gaussian fit of the lines. Note that some points overlap because they correspond to lines with the same upper energy level E_{up} .

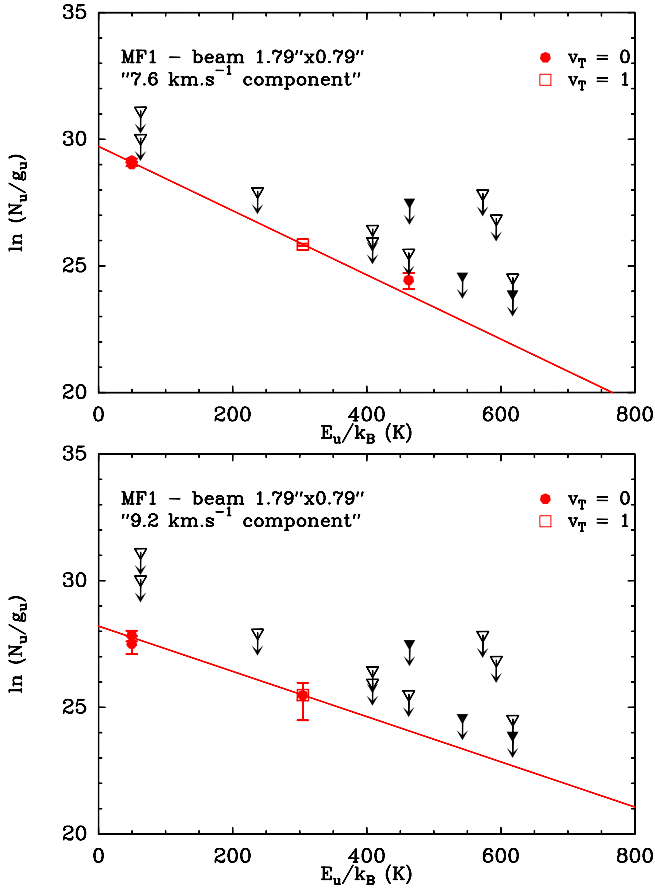


Fig. 9. Rotational diagram of the first (top) and the second (bottom) components toward the MF1 peak, based only on data observed with a synthesized beam of $1.79'' \times 0.79''$. Dots and squares with error bars mark detected and partially blended lines in the fundamental and first excited states $v_t = 0$ and $v_t = 1$, respectively, filled triangles mark undetected lines and open triangles blended lines. The red line is the fit according to the method described in Sect. 4. The derived temperature is 79 ± 2 K and 112 ± 50 K, respectively.

119 ± 10 K at a lower resolution). We also note for both components that the temperatures are lower with the high spatial resolution, suggesting an external heating of the clump. The rotational diagram taking into account both components leads to an average rotational temperature of 100 K.

The derived column densities are given in Table 5. The column density derived with a high spatial resolution is larger than that derived with a lower spatial resolution.

Rotational diagram at the MF2 peak

Both rotational diagrams, for angular resolutions of $1.79'' \times 0.79''$ and $3.63'' \times 2.26''$ (see sets 9 and 3, 7, 8, 10, 11, 12 in Table 1, respectively), give comparable rotational temperatures, within the uncertainties. We obtain 128 ± 9 K and 140 ± 14 K, respectively (see Fig. 11). The derived methyl formate column densities are given in Table 5.

Rotational diagram at the MF3 peak

The rotational temperature derived at a higher resolution is smaller (85 ± 3 K) than that at a lower resolution (103 ± 3 K) (see

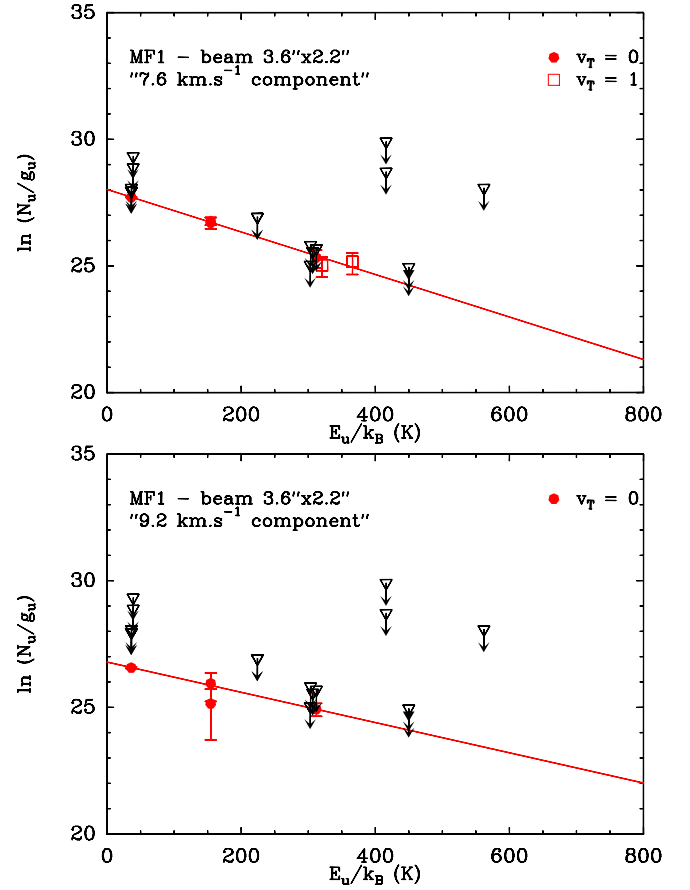


Fig. 10. Rotational diagram of the first (top) and the second (bottom) components toward the MF1 peak, based only on data observed with a synthesized beam of $3.63'' \times 2.26''$. Dots and squares with error bars mark detected and partially blended lines in the fundamental and first excited states $v_t = 0$ and $v_t = 1$, respectively, filled triangles mark undetected lines and open triangles blended lines. The red line is the fit according to the method described in Sect. 4. The derived temperature is 119 ± 10 K and 168 ± 30 K, respectively.

Fig. 12), suggesting external heating like for the MF1 peak. The derived methyl formate column densities are given in Table 5.

Rotational diagram at the MF4 peak

At 223 GHz, two velocity components are present as for the MF1 peak. Though two different upper energies are available, no rotational diagram at the resolution of $1.79'' \times 0.79''$ has been made because of the important error bars in the velocity decomposition. Fig. 13 shows the rotational diagram at a $3.63'' \times 2.26''$ resolution. The derived gas temperature and column density are given in Table 5.

Rotational diagram at the MF5 peak

As for the MF4 peak and from the same above-mentioned argument no rotational diagram has been made at the resolution of $1.79'' \times 0.79''$. Fig. 14 shows the rotational diagram at a $3.63'' \times 2.26''$ resolution. The derived gas temperature and column density are given in Table 5. These values are close to those found at the nearby MF4 position.

Table 5. HCOOCH₃ beam averaged column densities derived towards the emission peaks MF1 to MF5 for two angular resolutions.

Emission peaks	v^a (km s ⁻¹)	T_{rot}^b (K)		$N_{\text{HCOOCH}_3}^b$ (10 ¹⁶ cm ⁻²)	
		(1.79'' × 0.79'')	(3.63'' × 2.26'')	(1.79'' × 0.79'')	(3.63'' × 2.26'')
MF1	7.6	79±2	119±10	16.0±1.0	3.0±0.1
MF1	9.2	112±50	168±30	6.8±2.1	1.6±0.1
MF2	7.7	128±9	140±14	16.0±2.0	7.0±0.4
MF3	7.7	85±3	103±3	4.6±0.3	5.5±0.1
MF4	8.2	–	108±4	–	4.5±0.2
MF5	7.8	–	111±4	–	5.8±0.1

^a Towards MF1 and MF4 two different velocity components are identified but separate rotational diagrams could be made only for MF1 (see text) – for the other sources, velocity is a mean value of detected lines (see tables A.1, A.2 and A.4 for details).

^b Error bars reflect only the uncertainties in the gaussian fit of the lines

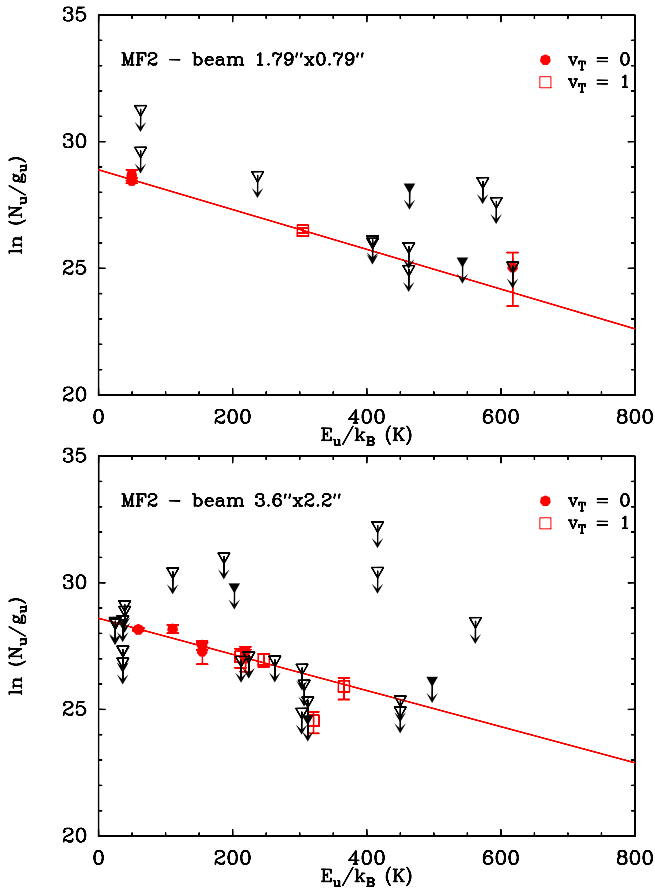


Fig. 11. Rotational diagrams toward the MF2 peak based only on data observed with a beam of 1.79'' × 0.79'' (top) and a beam of 3.63'' × 2.26'' (bottom). Dots and squares with error bars mark detected and partially blended lines in the fundamental and first excited states $v_t = 0$ and $v_t = 1$, respectively, filled triangles mark undetected lines and open triangles blended lines. The red line is the fit according to the method described in Sect. 4. The derived rotational temperatures are 128±9 K and 140±14 K, respectively.

The different temperatures obtained at different positions (MF1 to MF5) are most likely due to different physical conditions (see Sect. 8). When we compare the methyl formate emission from different energy levels (see Fig. 15), it is noticeable that

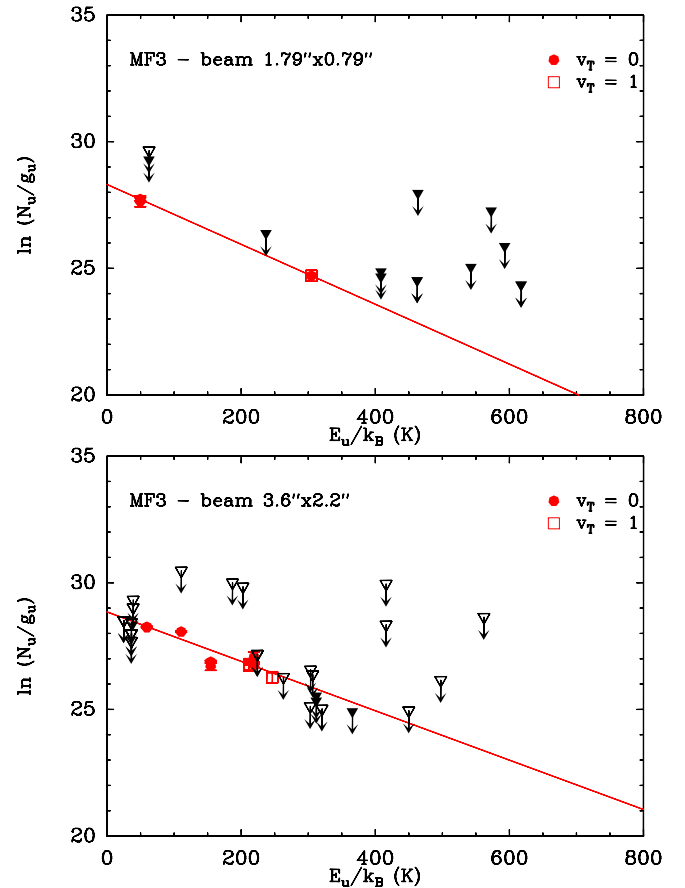


Fig. 12. Rotational diagrams toward the MF3 peak based only on data observed with a beam of 1.79'' × 0.79'' (top) and a beam of 3.63'' × 2.26'' (bottom). Dots and squares with error bars mark detected and partially blended lines in the fundamental and first excited states $v_t = 0$ and $v_t = 1$, respectively, filled triangles mark undetected lines and open triangles blended lines. The red line is the fit according to the method described in Sect. 4. The derived rotational temperatures are 85±3 K and 103±3 K, respectively.

for low upper state energies, the emission at the MF1 position is much stronger than at MF2. The emission at MF2 becomes stronger at higher energy levels.

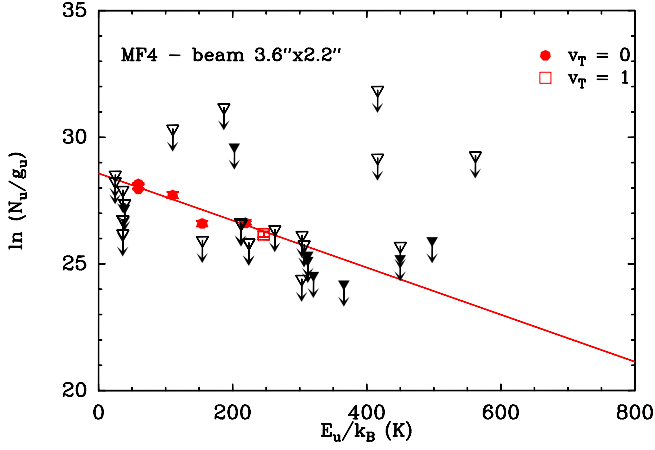


Fig. 13. Rotational diagram toward the MF4 peak based only on data observed with a synthesis beam of $3.63'' \times 2.26''$. Dots and squares with error bars mark detected and partially blended lines in the fundamental and first excited states $v_t = 0$ and $v_t = 1$, respectively, filled triangles mark undetected lines and open triangles blended lines. The red line is the fit according to the method described in Sect. 4. The derived rotational temperature is 108 ± 4 K.

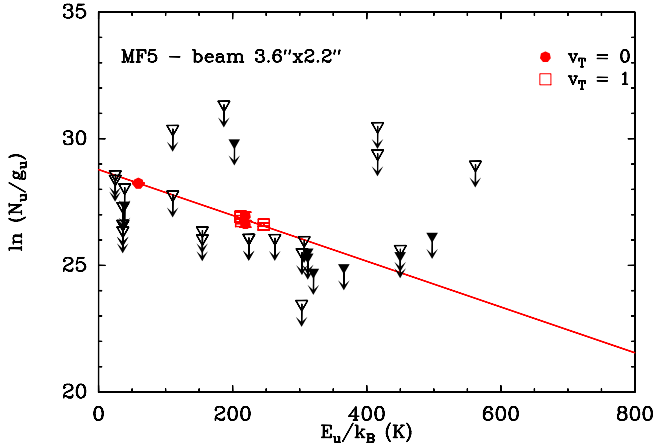


Fig. 14. Rotational diagrams toward the MF5 peak based only on data observed with a synthesis beam of $3.63'' \times 2.26''$. Dots and squares with error bars mark detected and partially blended lines in the fundamental and first excited states $v_t = 0$ and $v_t = 1$, respectively, filled triangles mark undetected lines and open triangles blended lines. The red line is the fit according to the method described in Sect. 4. The derived rotational temperature T is 111 ± 4 K.

5. Comparison with the other C₂H₄O₂ isomers

Methyl formate (HCOOCH₃), acetic acid (CH₃COOH) and glycolaldehyde (CH₂OHCHO) are three isomers among which acetic acid is the most stable. In a recent paper, Lattelais et al. (2009) have argued that the abundance ratio of isomers could be linked to their relative stability, except for some species as methyl formate. Indeed whereas methyl formate is known to be abundant in many molecular cores, glycolaldehyde has only been detected toward Sgr B2 (e.g. Hollis et al. 2000; Halfen et al. 2006) and acetic acid is barely detected in hot cores (e.g. Shiao et al. 2010).

We have searched for acetic acid and glycolaldehyde in our data sets (from upper energy levels of 18 K up to 452 K

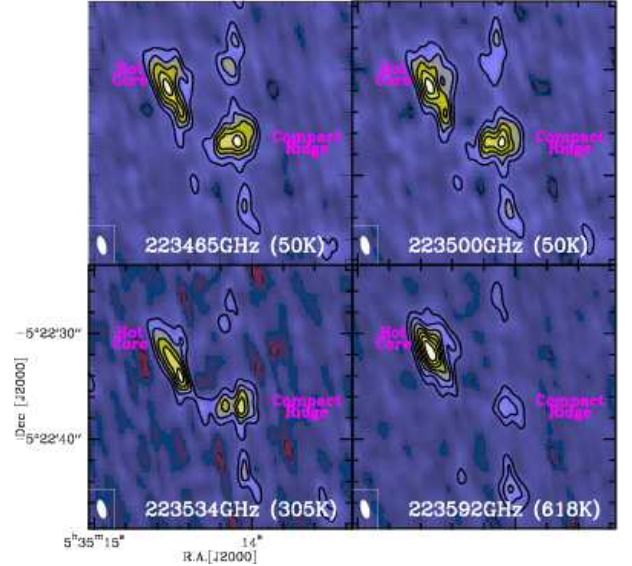


Fig. 15. HCOOCH₃ intensity maps integrated in velocity between 6 and 9 km s⁻¹. The line frequency and the upper state energy are indicated on each plot. The methyl formate emission is stronger towards MF1 than MF2 for low upper energy transitions, while the opposite is verified for high upper state energies.

and of 25 K up to 646 K, respectively), using Ilyushin et al. (2008) for the acetic acid frequencies, but we detect neither of them. Assuming the rotational temperatures derived from our HCOOCH₃ study, we have calculated upper limits for the column densities of these isomers at the MF1 and MF2 positions (Table 6). We find that the abundance of acetic acid is at least 50 times less than the methyl formate one and the abundance of glycolaldehyde at least 200-500 times less.

Table 6. Upper limits of column densities derived for acetic acid and glycolaldehyde from our PdBI data sets.

Emission Peak	Temperature (K)	Beam (″ × ″)	N (cm ⁻²)
CH ₂ OHCHO			
MF1	78	1.79 × 0.79	≤ 2.4 × 10 ¹⁴
MF1	120	3.79 × 1.99	≤ 2.8 × 10 ¹⁴
MF2	128	1.79 × 0.79	— ^a
MF2	140	3.79 × 1.99	≤ 3.5 × 10 ¹⁴
CH ₃ COOH			
MF1	78	1.79 × 0.79	≤ 1.8 × 10 ¹⁵
MF1	120	3.79 × 1.99	≤ 1.2 × 10 ¹⁵
MF2	128	1.79 × 0.79	≤ 2.6 × 10 ¹⁵
MF2	140	3.79 × 1.99	≤ 1.4 × 10 ¹⁵

^a All the glycolaldehyde lines are blended, so that the upper limit is not significant.

6. Dust emission and characteristics of main clumps

Fig. 2 shows that the continuum emission in the 101 to 225 GHz range is strong, extended and, from the highest frequency data, clumpy in places. In this Section we use the high spatial resolution and high signal-to-noise ratio achieved at 223 GHz (see

Fig. 16) to estimate, for the main clumps of dust emission, their masses, the mean projected H₂ column density and the H₂ volume density. Combining our line results with our N_{H₂} estimates we further derive the relative abundance of the methyl formate molecule.

There are 4 main dust clumps in our 223 GHz map (Fig. 16): two, Cb and Ca, lie in the Compact Ridge and the Hot Core near the methyl formate peaks MF1 and MF2, respectively; Cc, in the north lies near MF4 and MF5; another clump, Cd, lies in the south near MM23. Each clump exhibits a complex spatial structure which is not fully revealed even with our 1.79'' × 0.79'' spatial resolution. In the Compact Ridge for instance, we have identified toward MF1 two clear continuum maxima (labelled Cb₁ and Cb₂ in Figure 16) which we consider, however, as one “single clump” (Cb). Ca, Cc and Cd are most probably not single entities as well, but we will consider them as roughly Gaussian clumps in our subsequent analysis. We first give below details on the equations used to derive the mean clump properties.

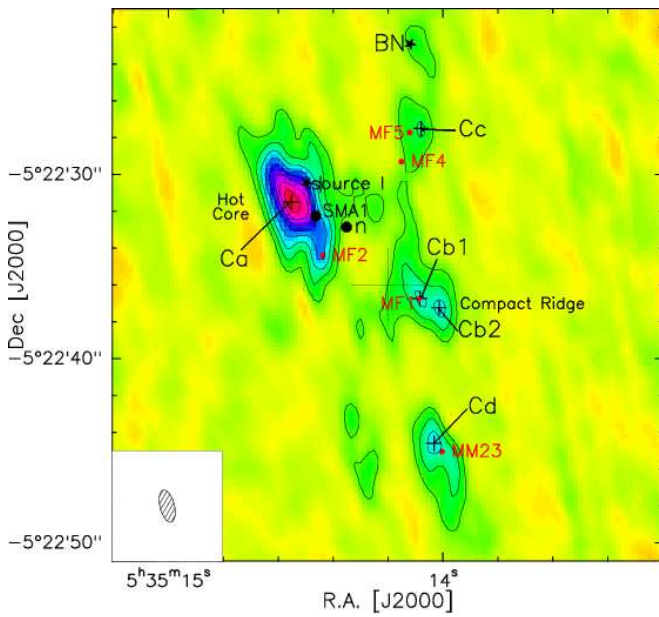


Fig. 16. Continuum emission map obtained with the IRAM Plateau de Bure Interferometer at 223.67 GHz. The level step is 60 mJy beam⁻¹ (3.5 σ) for a beam size of 1.8'' × 0.8''. Dark crosses label the 4 different continuum components while points label the main molecular HCOOCH₃ emission peaks.

The flux density, S_ν , from a dust cloud at frequency ν is given in the optically thin case by:

$$S_\nu \approx \tau B_\nu(T_d)\Omega \quad (3)$$

where τ is the dust opacity at frequency ν , $B_\nu(T_d)$ the Planck function, T_d the dust temperature and Ω the dust cloud solid angle. Estimating the dust column density and mass from the observables S_ν and Ω requires a dust opacity model and to know the variation of the extinction efficiency with frequency. This variation strongly depends on the wavelength range, the dust composition and its temperature. Mathis et al. (1977) suggested that the visible and UV interstellar extinction can be reproduced with a mixture of graphite and silicate grains and their model was extended to the infrared by Draine & Lee (1984). Draine & Lee (1984) showed that a mixture of silicate and graphite explains rather well the NIR and FIR observations and they showed that

the FIR opacity varies as λ^{-2} where λ is the wavelength. Of particular interest here is their estimate of the dust opacity at 125 μm as a function of the visual absorption or the projected H gas density N_H. They obtain $\tau = 4.6 \times 10^{-25} N_{\text{H}}(\text{cm}^{-2})$ which we extrapolate to the mm-wavelength regime, assuming that the extinction varies as λ^{-2} ,

$$\tau = 1.4 \times 10^{-26} \frac{N_{\text{H}_2}(\text{cm}^{-2})}{\lambda^2(\text{mm}^2)} \quad (4)$$

where we further assume the relation holds for molecular hydrogen with $N_{\text{H}} \approx 2N_{\text{H}_2}$. We are aware that the Draine & Lee (1984) data are rather typical of diffuse interstellar clouds and that dust coagulation as described by Ossenkopf & Henning (1994) for protostellar cores could be more appropriate. For an assumed central luminosity and outer envelope radius, the dust mass derived from a 1-D fit of the derived fluxes to the observed spectral energy distribution of the massive protostellar object W3IRS5 is 3 times lower with the Ossenkopf & Henning (1994) opacity profile than with the Draine & Lee (1984) profile (Luis Chavarria, private communication). However, the Ossenkopf & Henning (1994) opacities may be uncertain by a factor of at least 2 due to changes in the physical conditions and, given the additional dust to mass ratio uncertainty, derivation of the total gas mass in protostellar cores remains uncertain.

In this work we adopt a simple approach and combine equations 3 and 4 to derive in a straightforward manner the H₂ projected density and hence the total mass. Using the observed peak flux density per synthesized beam, s_ν in Jy beam⁻¹ (or source brightness temperature in K), and the Rayleigh-Jeans approximation, we derive, for the mean observing frequency of 223.65 GHz (1 Jy beam⁻¹ = 17.3 K, for a HPBW of 1.79'' × 0.79''), the beam averaged projected density from

$$\langle N_{\text{H}_2} \rangle = 2.22 \times 10^{27} \frac{s_\nu(\text{Jy beam}^{-1})}{T_d(\text{K})} \quad (5)$$

Assuming, for simplicity, that the dust clump is Gaussian with peak flux density s_ν and size $\theta_1 \times \theta_2$ determined from the 2-D Gaussian fits to the source half peak flux density, we derive the total gas mass in the entire Gaussian clump from the following equation (taking a mean molecular weight of 2.33 and adopting 414 pc as the Orion KL distance):

$$M_{\text{gas}}(M_\odot) \approx 188.7 \times \frac{s_\nu(\text{Jy beam}^{-1})}{T_d(\text{K})} \times \theta_1('') \times \theta_2('') \quad (6)$$

We use this equation to obtain the total gas mass present in our clumps (see Table 8).

All relevant gas clump parameters are gathered in Tables 7 and 8. They include the positions and names of the 4 main dust clumps as well as the adopted dust temperature (see details below), the peak flux in Jy beam⁻¹, the projected and volumic densities and, see last 4 columns in Table 8, the clump sizes, total flux density and estimated total gas mass within the identified clumps. The methyl formate relative abundance at continuum and molecular peaks is also given in the last column of Table 7.

The dust temperature is a crucial parameter in all of the above calculations. In order to estimate T_d we assume that : (a) the gas-dust relaxation time is short (Draine 2010; Tielens 2005), and (b) the gas temperature is close to the rotational temperature T_r deduced from our methyl formate data. The gas-dust relaxation time is roughly given by $4 \times 10^{16} \text{ s} / T_{\text{K}}^{0.5} n_{\text{H}_2}(\text{cm}^{-3})$ which is $\lesssim 130$ years for $n_{\text{H}_2} \gtrsim 10^6 \text{ cm}^{-3}$ and T_{K} around 100 K; therefore, dust thermalization should be well verified in Orion. T_r is

Table 7. Beam averaged density and methyl formate relative abundance at 223 GHz continuum and molecular peaks.

Continuum Source	R.A (J2000) 05 ^h 35 ^m	Dec (J2000) -05°22′	Adopted T _d (K)	s _v ^a (Jy beam ⁻¹)	$\langle N_{H_2} \rangle^b$ (10 ²⁴ cm ⁻²)	$\langle n_{H_2} \rangle^c$ (10 ⁸ cm ⁻³)	$\langle N_{HCOOCH_3}/N_{H_2} \rangle^d$ (10 ⁻⁸)	
Ca	14 ^h 56	31 ^m 50	200	0.49	5.4	7.3	≤0.6	at continuum peak
			130	0.18	3.1	4.2	5.2	at MF2 molecular peak
Cb	Cb ₁ 14 ^h 08	36 ^m 73	80	0.18	5.0	6.8	3.1	at continuum peak
	Cb ₂ 14 ^h 01	37 ^m 24	80	0.18	5.0	6.8	3.1	at MF1 molecular peak
Cc	14 ^h 08	27 ^m 50	110	0.12	2.4	3.3	≤0.3	at continuum peak
			110	0.08	1.6	2.2	≤0.2	at MF4 molecular peak
			110	0.08	1.6	2.2	≤0.5	at MF5 molecular peak
Cd	14 ^h 03	44 ^m 60	105	0.17	3.6	4.9	≤0.1	at continuum peak
			105	0.17	3.6	4.9	≤0.1	at MM23 molecular peak

^a flux density per beam or brightness temperature.

^b estimated in a beam size of 1.79″ × 0.79″.

^c estimated in a beam size of 1.79″ × 0.79″ at a distance of 414 pc (Menten et al. 2007).

^d estimated at continuum and associated molecular peaks. The methyl formate column densities are derived from this work.

Table 8. Dust clump half sizes, total flux density and total gas mass within the dust clumps.

Continuum source	Nearby molecular peak	Adopted T _d (K)	Adopted clump surface ^a (″ × ″)	M _{gas} (M _⊙)	S _{total} (Jy)
Ca	MF2	200	5.0 × 2.5	5.8	3.9
Cb ^b	MF1	80	4.0 × 2.5	4.3	1
Cc	MF4, MF5	110	2.6 × 1.5	0.8	0.45
Cd	MM23	105	3.0 × 1.5	1.4	0.8

^a taken at half size

^b Overall structure including C_{b1} and C_{b2}.

rather well determined from our LTE multi-line analysis. Hence, it is reasonable to assume that both (a) and (b) are verified, thus $T_d \approx T_r$. Another complication arises because T_d is not uniform throughout Orion as demonstrated by our continuum maps, and our continuum and line peaks do not match exactly. The values of T_d adopted here are given in Tables 7 and 8. They are taken from the rotational temperature obtained for the main gas peaks MF1, MF2, MF4, MF5 and MM23. There is also some uncertainty at the continuum peaks near both MF2 and MM23 because only 3 and 2 methyl formate lines were unambiguously detected in these directions (while many lines are present at the molecular peaks); in this case we used our best judgement to estimate T_r and thus T_d .

The beam averaged projected density N_{H_2} lies in the range 2 to 5 × 10²⁴ cm⁻² corresponding to very large visual extinctions. The latter density is used to derive the volumic H₂ density across the synthesized beam projected at the 414 pc distance of Orion-KL; it lies in the range 2 to 7 × 10⁸ cm⁻³. Our derived densities are much higher than those found in the literature (e.g. Irvine et al. 1987; Persson et al. 2007; Mezger et al. 1990). However, our spatial resolution is higher and the densities are similar if we take into account the beam dilution. Moreover, we find similar H₂ density values when we use the continuum map of Beuther et al. (2004) and use their source and dust properties hypothesis.

Our individual clump masses vary from about 1 to 5 solar masses. We stress that these individual masses cannot be highly accurate because of various reasons. First, any T_d uncertainty is directly translated into a mass uncertainty in our mass equations. Second, an uncertainty in the opacity wavelength dependence also results in a mass uncertainty; at 1.3 mm there is a 30% mass change when the extinction varies from a λ^{-2} dependence to λ^{-1} .

Third, as explained earlier our clumps might not be Gaussian and our observed spatial structure might be even more clumpy than reported here. Another way to estimate our mass uncertainty is to derive the total gas mass for the entire clump from the equation, $M_{gas}(M_{\odot}) \approx 270 \times \frac{S_v(Jy)}{T_d(K)}$, where S_v is the flux density measured in Jy in our calibrated maps (see last column in Table 8). The derived masses differ from those obtained with equation 6 by about 9% to 30%. Despite these uncertainties, we estimate that the total mass derived for all clumps identified here, about 12 solar masses, is meaningful. This mass reservoir could well be used in future star forming activity.

In the last column of Table 7 we also give the methyl formate relative abundance averaged over the synthesized beam in the direction of the 223 GHz dust emission peaks and of the molecular peaks. The relative abundances lie in the range $\leq 0.1 \times 10^{-8}$ to 5×10^{-8} and show variations from one peak to another. Toward Cc and Cd, there are not enough detected molecular lines to estimate a precise methyl formate column density and we only give upper limits of the relative abundance. Toward Cb there is no difference in abundance between the molecular and continuum peaks, while there is a marked difference in the relative abundances measured toward the Hot Core (Ca) and the associated Hot Core-SW molecular peak (MF2). The largest methyl formate relative abundances are observed toward MF2 and MF1.

7. Comparison with previous studies

In this section we try to relate our results to some of the most comparable and recent other studies of Orion-KL. The large number of published works devoted to this region prevents us from being exhaustive. Therefore, we limit ourselves to the high (<10″) resolution studies of the continuum emission and methyl

formate emission. There is a general agreement on space and velocity distribution and on column densities derived; however, our data show more details due to higher spatial and/or spectral resolution.

Methyl formate temperatures were often not derived by previous authors from their interferometric studies so we quote also for reference other temperature indicators at high resolution: dust color temperature, and methanol (CH₃OH) and methyl cyanid (CH₃CN) rotational temperatures. Methanol is interesting because this O-bearing species may be formed on grains (e.g. van der Tak et al. 2000) like methyl formate, and, as stated previously it may also be a precursor of methyl formate. It may however suffer opacity problems, and its excitation is often more complex than LTE (see e.g. Menten et al. 1988; Leurini et al. 2004). Methyl cyanide is a well-known probe of kinetic temperature (Boucher et al. 1980). But N-bearing species have a different distribution, so that temperatures derived from these molecules may thus differ from those derived from methyl formate.

Much work has been done on the other hand with single dish telescopes towards Orion-KL, and large surveys allow for the determination of a temperature of the region averaged over the beam, and sometimes for a decomposition into a few spectral features identified from their velocity profiles. We quote previous results on methyl formate and methanol avoiding, however, studies most affected by optical thickness effects. The HCOOCH₃ temperatures we derive fall in the 60-220 K range found in these studies.

7.1. High resolution continuum maps

Our 1.3 mm continuum map differs from the Hot Core maps obtained with the SMA at 345 GHz and 690 GHz by Beuther et al. (2004) and Beuther et al. (2006) because we do not see any emission peak on source I and SMA1. We note that the Beuther et al. (2004) and Beuther et al. (2006) maps already show differences between each other. This could be due to the different spatial resolutions and/or to the different *uv* coverages used in these two works. Finally, we note that the SMA 870 μ m dust continuum maps of Tang et al. (2010) is much similar to our 223 GHz map obtained with a 1.79'' \times 0.79'' resolution. Our map covers a more extended region of the southern Compact Ridge but all other clumps observed by us along the Ridge up to BN are also detected in the 0.8'' \times 0.7'' SMA map. As also suggested by our 1.3 mm map, the 870 μ m dust emission map shows that there are at least two clumps in the Hot Core region. From their polarization study of the Hot Core and Compact Ridge Tang et al. (2010) suggest that the magnetic field is regulating star formation at large physical scales. Hence, all clumps identified here are probably intimately related with the Orion large scale magnetic field.

7.2. High resolution studies of methyl formate distribution and temperature

Our methyl formate emission peaks MF1, MF2 and MF4-5⁶ are also present in the interferometric maps of Friedel & Snyder (2008) and Beuther et al. (2005) but the MF3 and MF4 peaks are less obvious in their data. Their maps, like ours, do not show any emission of this molecule towards the Hot Core around 5 km s⁻¹.

⁶ The MF5 emission peak corresponds to the IRc6 position in Friedel & Snyder (2008) and Beuther et al. (2005).

The methyl formate observations of Friedel & Snyder (2008) made with the CARMA interferometer with a 2.5'' \times 0.85'' beam size also reveal components at 7.6 km s⁻¹ and 9.3 km s⁻¹ towards the Compact Ridge region⁷. However the authors do not separate the two velocity components to derive the temperature and the column density. Their results agree with ours if we do not separate the two HCOOCH₃ spectral components: $T_{rot}=101$ K and $N_{HCOOCH_3}=1.5 \times 10^{17}$ cm⁻². Moreover methyl formate emission towards the Compact Ridge region has also been observed with BIMA by Liu et al. (2002) and Remijan et al. (2003). Their spatial and spectral resolutions do not allow them to see the two velocity components and they derive a temperature and a column density similar to those found by Friedel & Snyder (2008) and to ours when we combine the two components into one.

Hollis et al. (2003) also imaged methyl formate at high resolution (2.9'' \times 1.6'') using the VLA at 45 GHz. The very low ($E_u = 6$ K) energy of the upper state of the transition they observed shows that emission from the Compact Ridge is dominant, thus confirming the trend shown in our Fig.15. Despite their very good spatial resolution, their limited spectral resolution (1.36 km s⁻¹ channel separation) allows them to detect only two broad peaks beside the Compact Ridge, corresponding to our MF2 and MF4-5 peaks. At the Compact Ridge peak (MF1), again summing up our two velocity components, our column density agrees with their value derived for a temperature of 100 K.

The interferometric map of methyl formate at 2'' \times 1.5'' resolution integrated over velocities obtained with the Owens Valley interferometer by Blake et al. (1996) shows a reasonable global agreement with ours: Hot Core-SW and MF4-5 (IRc6) peaks are displaced from ours by <1'', and their Compact Ridge peak lies 1.5'' North of MF1; the emission around MF4-5 (IRc6) appears more intense and more extended, with peaks displaced by $\sim 1''$ compared to ours.

7.3. Other temperature determinations

7.3.1. From dust infrared emission

Our temperature estimates lie in the range 80-170 K which is close to the range of (color) dust temperatures found by Wynn-Williams et al. (1984) from their 30 μ m and 20 μ m measurements, but they are lower than the temperatures they derive at shorter (and more optically thick) wavelengths. However, the temperature variations observed by Wynn-Williams et al. (1984) between the Hot Core, the Compact Ridge and IRc6 (MF4-5) are not ordered as in our study. This may be due to remaining opacity effects in the mid-infrared. In a more recent work Robberto et al. (2005) derived color temperatures in Orion-KL (excepting BN) of 125-140 K from 10 and 20 μ m observations, and higher values (200-230 K) from silicate features, using a simple "two-component" model for the IR emission.

7.3.2. From methanol and methyl cyanide high resolution studies

A comparison of our results with the temperatures derived from previous interferometric works on methanol (CH₃OH) by Beuther et al. (2005) cannot be done toward the Compact Ridge and the Hot Core-SW because, unfortunately but not surpris-

⁷ Note that the Compact Ridge position defined in Friedel & Snyder (2008) is not the the same as that used in this study. Their IRc5 position is closer to our Compact Ridge position (1.5'' away).

ingly, our two strongest methyl formate peaks correspond to areas where methanol is optically thick. It is only in the direction of MF4-MF5 (IRc6) that we observe some overlap with their temperature map: they find a somewhat higher temperature, around 180-240 K to be compared with our ~ 110 K. Note that methanol emission is more extended than methyl formate and does not sample exactly the same gas, and methanol may be formed at least in part in the gas phase (e.g. Plambeck & Wright 1988); note also that a methanol maser has been identified by the latter authors at IRc6.

As N-bearing and O-bearing molecules clearly do not share the same spatial and velocity distribution (see e.g. their position velocity diagram showing the much broader velocity range of CH₃CN emission), no simple comparison can be made of our work with the higher temperature values recently obtained by Wang et al. (2010) using CH₃CN (190-620 K in the Hot Core and 170-280 K in the Compact Ridge).

Our temperatures and column densities derived from the analysis of the MF1 emission peak suggest an external heating towards the Compact Ridge. It is interesting to mention that recently Zapata et al. (2010) have also found some evidence for external heating towards the Hot Core. These two dense regions of the Orion-KL nebula seem to be associated with the dynamical event which occurred 500 years ago.

7.3.3. From single dish methyl formate and methanol studies

From a single dish measurement of the optically thin isotopologue ¹³CH₃OH Blake et al. (1984) derived a rotational temperature of 120 K averaged over their 30'' beam; this is close to the 140 K derived for CH₃OH by Johansson et al. (1984) with a similar beam. Blake et al. (1987), also in a 30'' beam, have attributed the methanol and methyl formate emissions to the Compact Ridge and derived rotational temperatures of 146 \pm 3 K and 90 \pm 10 K respectively, whereas a temperature of 166 \pm 70 K was found in the Hot Core from their H₂CO data. Within a ~ 22 -28'' beam Menten et al. (1988) have derived from their CH₃OH and ¹³CH₃OH observations rotational temperatures of 109-147 K and 33 K respectively. Their CH₃OH line profiles are interpreted as the superposition of a broad and a narrow component (the former marginally warmer by 10-20 K). This interpretation, aimed both at thermal emission and maser excitation, suggests that infrared radiation from the dust plays an important role in the excitation of methanol in addition to collisions. From a 325-360 GHz survey made with 20'' resolution, Schilke et al. (1997) found rotational temperatures of 188 \pm 3 K (methanol) and 98 \pm 3 K (methyl formate). More recently, at 350 μ m and with a 11'' beam Comito et al. (2005) infer 220 K for the Hot Core, and 160 K for the Compact Ridge from CH₃OH lines, and an almost identical value (220 K and 155 K) from H₂CO. A somewhat lower temperature, 61 K, was found in a 40'' beam for methyl formate by Ziurys & McGonagle (1993).

Very recently Herschel observations of ¹³CH₃OH (and CH₃OH) at 534 GHz and 1061 GHz made by Wang et al. (2011) determined $T_{\text{rot}} = 105 \pm 2.6$ K (resp. $T_{\text{rot}} = 125 \pm 2.8$ K) in the Compact Ridge; the Compact ridge was isolated from other spatial components in the 43'' and 20'' Herschel beams thanks to its velocity profile. A more elaborated transfer model developed for a spherical source with a temperature gradient provides a very good fit to the methanol population diagram of the Compact Ridge at both frequencies if it is externally heated. This conclusion well agrees with our findings.

8. Discussion on methyl formate distribution and Orion structure

The Orion-KL region is located about 1' from the Trapezium OB stars at the heart of a large stellar cluster still in formation. Many remarkable objects have been identified in this region (see e.g. reviews by Irvine et al. 1987; Genzel & Stutzki 1989; O'dell et al. 1993; O'dell 2001; O'Dell & Henney 2008; O'Dell et al. 2009). In this Section, we primarily try to correlate the HCOOCH₃ distribution with several optical, NIR, MIR, X, radio continuum and radio line data, with the help of the ALADIN software⁸ (Bonnarel et al. 2000) and the SIMBAD database⁸. We focus our discussion on the Compact Ridge and Hot Core regions as they contain the main methyl formate peaks in Orion-KL (MF1 and MF2, respectively).

8.1. Stars and YSOs

Orion-KL is a complex region, with a very high density of YSOs (Young Stellar Objects) and recently formed stars.

Putting together the remarkably detailed NIR pictures of Stolovy et al. (1998) and D. Rouan (private communication) together with the X picture (Getman et al. 2005; Grosso et al. 2005) and previous IR work (Greenhill et al. 2004; Hillenbrand & Carpenter 2000; Lonsdale et al. 1982; Muench et al. 2002), and including the IR polarization work of Simpson et al. (2006) we have been able to identify more than 34 probable stars or forming stars in the 0.5' region of methyl formate emission in Fig. 4. In this 0.058 pc wide field, this means a projected density of 156 objects arcmin⁻² (1 object every $\sim 5''$) or 10⁴ objects pc⁻². For comparison, Lada et al. (2004) determined stellar projected densities for deeply embedded sources reaching up to 3000 star pc⁻² south of Orion-KL (this would mean 10 objects in the same 0.5' region of Fig. 4); for less embedded stars close to the Trapezium, the observed projected density is twice higher, up to 6000 star pc⁻². With such a high density, one should always keep in mind the possibility of chance projection effects in the following spatial comparisons.

Over small distance scales (a few '' or 1000-2000 AU), and with the exception of Parenago 1822/LBLS k at the center of the Compact Ridge (see discussion below), little correlation is seen between the methyl formate (MF) peaks and the stellar objects. Almost no association is obvious as well with the IRc sources, as seen on figure 17 which shows the position of the IRc sources from Shuping et al. (2004) with respect to the methyl formate emission. Over larger scales ($\geq 10''$ or 4500 AU) it seems, as discussed below, that the methyl formate distribution is closely linked to the presence of a few remarkable objects, in particular the "low-velocity" SiO outflow whose origin is attributed to radio source I by Goddi et al. (2009) and Plambeck et al. (2009), and linked to the matter (traced in CO and H₂) ejected during the recent (~ 500 yr) stellar collision or close interaction between the B-type star BN, and the I and n objects (at least) as proposed by e.g. Zapata et al. (2009). Long range effects due to heating, photodissociating photons or shocks are also possible from BN itself and source n. Note that our data do not allow us to separate the respective effects of source I from source SMA1 which has recently been identified by Beuther & Nissen (2008) as another candidate source for the high-velocity CO and H₂ outflow.

⁸ Centre de Données Astronomiques de Strasbourg, see: <http://aladin.u-strasbg.fr/aladin.gml> and <http://simbad.u-strasbg.fr/simbad/>.

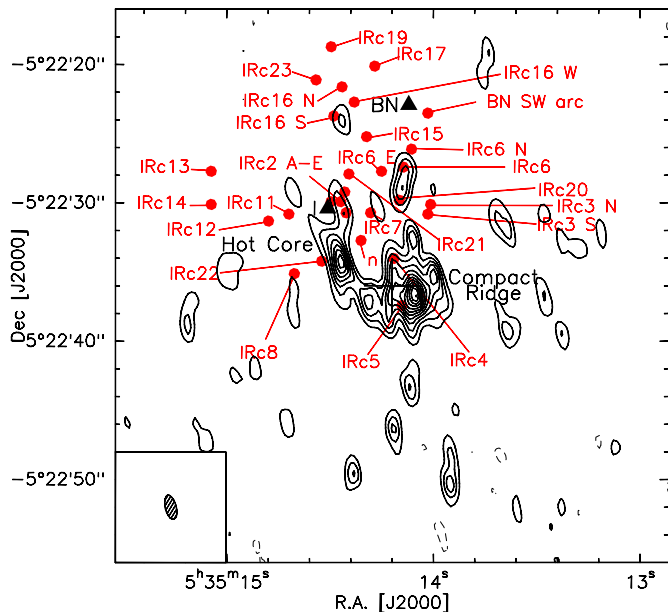


Fig. 17. Positions of the IRc sources identified by Shuping et al. (2004) on the methyl formate integrated intensity map (see Fig. 4).

8.2. HCOOCH_3 and the “low-velocity” SiO outflow

As shown in Fig. 18 there is a striking complementarity of the 87 GHz SiO $v=0$ $J=2-1$ line map from Plambeck et al. (2009) with our methyl formate distribution. We consider that this fact is not fortuitous and points to some kind of direct connection between both species. The SiO traces the large “low-velocity” outflow originating from radio source I. As shown by various proper motion studies (Gómez et al. 2005; Rodríguez et al. 2005; Goddi et al. 2010) source I is moving towards the South-East (bottom left).

The HCOOCH_3 distribution near MF2 (Hot Core-SW) may be due, to a large extent, to the recent sidewise “encounter” of this outflow with quiet dense gas resulting in shocks which in turn disrupt icy grain mantles and release new molecules. The Hot Core region would then be the prominent result of this sidewise encounter. With this picture in mind one expects a recent major increase in the release of molecules from grains in the Hot Core region and in the eastern side of the large scale V-shaped region mapped in MF in this work.

The Compact Ridge methyl formate distribution also matches the shape of the SiO outflow. In this area, the interaction is more frontal, the outflowing matter coming more or less perpendicular to the border of the quiescent gas. The SiO outflow could be older than the stellar collision event. In that case the shock at the Compact Ridge would be older than the collision and be modified only by the recent motion of source I. Alternatively, the outflow could be linked to the stellar collision, or its trajectory might have encountered the Compact Ridge gas because of the recent proper motion of source I. In the first case, the release of molecules from grains would be older than 500 yr, in the latter case it would be more recent. Such a connection between the “low-velocity” outflow and the Compact Ridge has been proposed earlier (see e.g. Irvine et al. 1987).

A shock from the I outflow can either release CH_3OH rich ices, followed by gas phase chemistry leading to HCOOCH_3 formation (Charnley & Rodgers 2005), or directly release HCOOCH_3 formed on the grain (Garrod & Herbst 2006). The

detailed chemical modelling is beyond the scope of the present study.

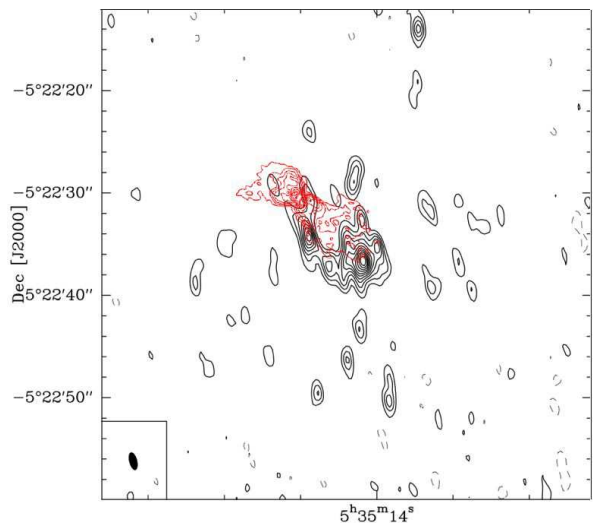


Fig. 18. HCOOCH_3 contours (in black) overlaid over the SiO $J=2-1$ $v=0$ map (red contours) by Plambeck et al. (2009). Note the nice match of the SiO outflow with the quiescent and recently shocked gas traced by HCOOCH_3 as the SiO fills the hole in the methyl formate distribution.

8.3. HCOOCH_3 and IR 11 μm map

In Fig. 19 we compare the methyl formate distribution with the 11 μm map of Smith et al. (2005). There is a clear trend for the MF emission peaks to lie outside the bright 11 μm regions—it is especially true for the East branch of the V-shaped MF emission, which encompasses the Hot Core MF2 and goes from MF7 to MF10. A notable apparent exception to this anticorrelation (but see below) is the main source MF1 located in the Compact Ridge.

It has long been noted that there is a tendency for some molecular emission in Orion-KL, in particular NH_3 , to be anticorrelated with mid-IR emission (e.g. Genzel & Stutzki 1989; Wynn-Williams et al. 1984). Recently Shuping et al. (2004) reached a similar conclusion from their high resolution mid-IR map and the NH_3 high resolution map of Wilson et al. (2000): they suggest that the NH_3 emission comes from a foreground layer of interstellar matter, cold and dense enough to be seen in the mid-IR as an absorbing dark lane against a brighter background.

We propose that most of the methyl formate emission seen in places of low 11 μm emission is also originating in this dark foreground material. In the case of MF1 in the Compact Ridge, there are indications that the methyl formate layer is also in the foreground material, but is thin enough to let the IR background radiation to be seen through it (see discussion on excited H_2).

8.4. HCOOCH_3 and 2.12 μm H_2 emission

MF1: A most striking spatial correlation is observed between the methyl formate distribution at the MF1 peak and the 2.12 μm

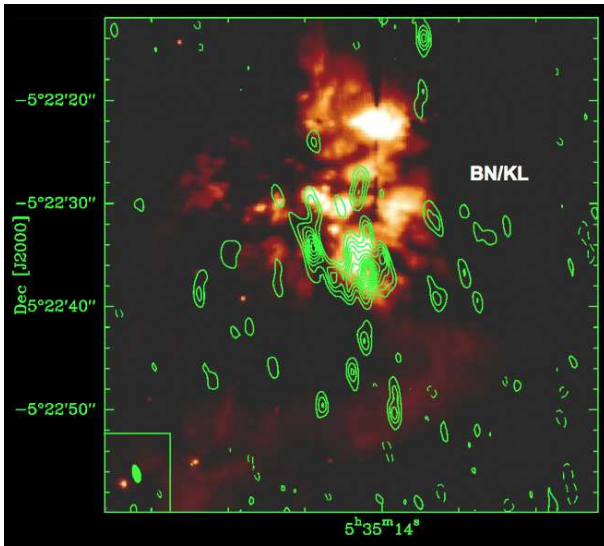


Fig. 19. The HCOOCH₃ emission contours from MF7 to MF10 follow closely a black zone where 11 μ m IR emission is lacking (Smith et al. 2005), most probably due to a dense, absorbing foreground gas/dust lane. Such an anticorrelation has been observed for NH₃ and interpreted in a similar manner by Shuping et al. (2004) using the NH₃ map of Wilson et al. (2000)

H₂ emission imaged by Lacombe et al. (2004) with adaptive optics (NACO) at the Very Large Telescope. This is shown in Fig. 20. Additional H₂ pictures can be found in Stolovy et al. (1998) and Nissen et al. (2007).

We first note a global overlap of MF1 with a zone of excited H₂ emission. Going into details, the MF1 methyl formate distribution departs from a simple elliptical shape, showing several extensions: 1) the MF1 peak corresponds to a local maximum of H₂ emission, 2) there is a second peak at a North West position of the Compact Ridge (labeled NW in Fig. 20) in both tracers, 3) Two extensions of the MF map towards the South South East and West respectively of the Compact Ridge (labeled SSE and SSW in Fig. 20) correspond to two other peaks. These findings strongly support the association between MF and excited H₂. At the North East of the Compact Ridge (position labeled NE in Fig. 20), MF overlaps the strong 2 μ m continuum emission which has been subtracted and appears as a black zone in Fig. 20. This prevents a good comparison of the H₂ emission in this area. However, inspection of the Subaru map (Fig. 21) confirms that there is also 2.12 μ m emission there.

The North and South MF extensions have no counterpart at 2.12 μ m (only faint 2.12 μ m emission is present near N). They seem to be related to a different layer of emission, which appears as a North-South bar in the MF channel maps at velocities around or larger than 9 km s⁻¹. Because such a structure does not show up in any optical or IR map, we consider it likely that the gas is on the far side of OMC-1, probably behind the KL nebula itself.

Other peaks: The methyl formate - excited H₂ association observed in the MF1 area is also observed on a broader scale, especially, clockwise from the West, toward MF19, MF18-SW, MF21, MF27, MF8, MF23. However, some MF peaks have no excited H₂ emission counterpart: for example, and most notably, there is no H₂ emission at the MF2 (Hot Core-SW) peak; however excited H₂ emission is present in its Southern part (Fig. 20

and 21). Conversely bright 2.12 μ m emission areas (e.g. East of the Hot Core, close to star LBLs t) do not exhibit MF emission.

To better understand the diversity of the observations the following explanations are worth considering:

- MF is seen associated with a 2.12 μ m emission if the shock related to the Orion-KL explosive event passes through interstellar material dense and cold enough so that grains have ice mantles. In that case the correlation observed toward MF1 is explained by the shock-induced release of methyl formate or its progenitor CH₃OH from ice-coated grain mantles.
- The molecular production efficiency related to the shock may also be low in places, or cold grain mantles may be less abundant (e.g. closer to the very luminous Trapezium OB stars located 1' SE of Orion-KL), so that the MF column density is undetectable.
- In some other places (e.g. around LBLs t) the 2.12 μ m emission geometry suggests that the emission is linked to the star and thus might be of a different nature.
- MF may also peak in regions where it is released or produced by mechanisms (e.g. thermal heating) different from the shock generated by the explosive event.
- H₂ emission may be hidden in some areas by a large column density of foreground dust.

The latter possibility is well illustrated by the comparison of the H₂ 2.12 μ m map of Lacombe et al. (2004) (Fig. 20) with the Subaru deep exposure (Fig. 21, reproduced in extenso in Shuping et al. 2004). The larger extension of the H₂ emission seen in the Subaru map indicates that a rather “thin” layer prevented some H₂ peaks to be visible in the Lacombe et al. (2004) map. For a few H₂ emission spots in this field Colgan et al. (2007) estimated indeed a foreground absorption corresponding to $A_v = 4-8$. In the direction of the Compact Ridge, the NIR sources IRC4 and IRC5 are interpreted as reflection nebulae seen through holes of foreground matter (Shuping et al. 2004; Simpson et al. 2006); the larger size of these sources (hence of these holes) at 11 μ m compared to 2 μ m (continuum) is an additional indication of the relative thinness of the foreground matter.

On the contrary the MF2 peak would be a case where strong dust absorption hides all H₂ 2.12 μ m emission. Close to MF2, very large opacities are advocated to explain the non-detection of the bright source I (e.g. Greenhill et al. 2004). Indeed from our continuum data (Sect. 6) we derive at both MF1 and MF2 peaks large N_{H₂} column densities (5 and 3.1 10²⁴ cm⁻² respectively); this corresponds to $A_v \geq 1000$, assuming standard dust opacities. Our interpretation of the contrasted situation at both peaks is that at the Compact Ridge (MF1), a shock hits the front side of a dense clump of matter, whereas at the Hot Core-SW (MF2), it hits the rear side (with respect to the observer). The presence close to MF2 of a H₂O maser spot (053247.001-052427.81, Gaume et al. 1998), similar to other spots found in the Compact Ridge, strengthens the hypothesis that a shock is present there too.

The source of excitation of the H₂ molecules is most likely linked to the global explosive event. Most of the H₂ emission can be traced to a common center whose coordinates are given in Table 9 (e.g. Zapata et al. 2009 and refs. therein). Stolovy et al. (1998) analyse in detail two remarkable features which they call the “nested arcs” and the “bullets” (see their Fig. 4c), and suggest that other H₂ features in their map could be of similar nature but are less easily identified due to projection effects. If this is indeed the case, the comparison with these two features favourably seen in a more edge-on configuration sheds some light on the probable geometry of the shocked region at MF1, and how the shock

might lead to the release of methyl formate from grain mantles; a detailed modelling at MF1 is however required.

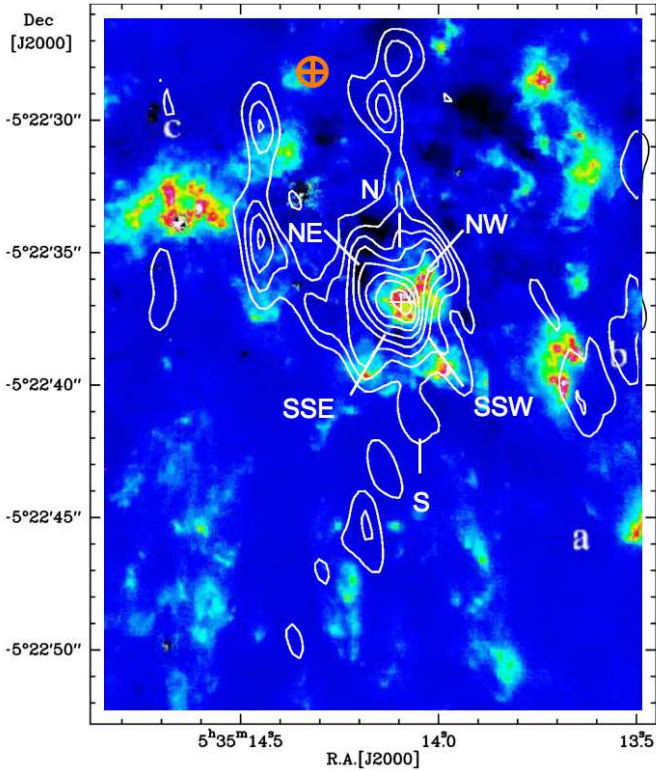


Fig. 20. Methyl formate 8.7 km s⁻¹ channel map contours overlaid over Lacombe et al. (2004) 2.12 μm excited H₂ emission showing a good correlation of both tracers toward MF1 (white cross) and around (North West (NW), South South West (SSW) and South South East (SSE)). The North East (NE) region analysis is hampered by the subtraction of strong 2 μm continuum from IRC4 (see Fig. 17) – which results in an artefact (the zone in black). Emission toward the North (N) and the South (S) seems of a different nature and is linked to the 9-10 km s⁻¹ velocity gas (see discussion). Note that a fraction only of the H₂ “bullets” distribution (those moving towards us and thus closer to the observer) is expected to suffer sufficiently low extinction to be visible. The red circled cross marks the proper motion center where the sources n, I and BN were located 500 years ago (Gómez et al. 2005, 2008; Rodríguez et al. 2005).

8.5. Main Methyl Formate peak MF1 (Compact Ridge)

In addition to the correlation observed between the low-velocity outflow traced by SiO and the excited H₂ emission at 2.12 μm discussed above, some other remarkable objects are observed towards the main MF peak, MF1. The visible star Parenago 1822/LBLS k (Parenago 1954, 1997) is situated right in the middle of the MF1 methyl formate peak. It exhibits 1.3 mm continuum emission which is analyzed as disk emission by Eisner et al. (2008) under the name HC 438. Getman et al. (2005) derive an age of 22 000 yr and a small mass of 0.26 M_⊙. Another nearby remarkable object is the H₂O “Supermaser” identified and studied by Matveenko et al. (2000), see also

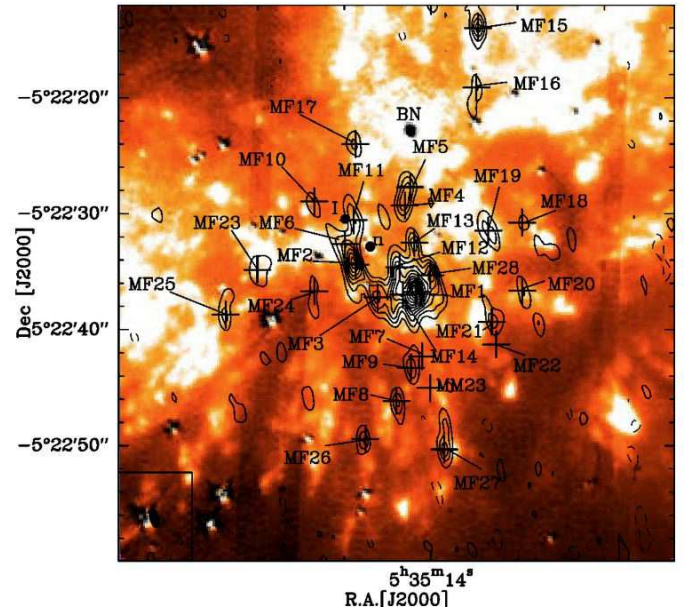


Fig. 21. Map of the integrated methyl formate emission (cf. Fig. 4) overlaid over a Subaru Observatory image of H₂ at 2.12 μm emission (© Subaru Telescope, NAOJ. All rights reserved). In this large-scale image, the “methyl formate - excited H₂” correlation is evident in several peaks other than the MF1 peak (Fig. 20): e.g. MF19, MF18-SW, MF21 (even more clearly seen in Fig. 20), MF27, MF8, MF23. Note, however, that some HCOOCH₃ or H₂ peaks have no counterpart. Possible explanations are given in the text.

Table 9. Coordinates of noticeable objects or places near the main methyl formate peak (MF1).

Object/place	R.A. (J2000) 05 ^h 35 ^m	Dec. (J2000) -05°22'	Precision
HCOOCH ₃ MF1 peak ^a	05 35 14.09	-05 22 36.7	±0.8"
P1822/LBLS k ^b	05 35 14.092	-05 22 36.43	
COUP 600 X source ^c	05 35 14.09	-05 22 36.4	
H ₂ O supermaser ^d	05 35 14.12	-5 22 36.27	
HC 438 ^e	05 35 14.09	-5 22 36.6	
CO Fingers Outflow Center ^f	05 35 14.37	-05 22 27.9	±1.5"
Proper motion center ^g	05 35 14.35	-05 22 27.7	±1"

^a This study

^b SIMBAD

^c Grosso et al. (2005)

^d Matveenko et al. (2000) after Greenhill et al. (2004)

^e Eisner et al. (2008)

^f Stolovy et al. (1998); Zapata et al. (2009)

^g Gómez et al. (2005, 2008); Rodríguez et al. (2005)

Demichev & Matveenko (2009) and Matveenko et al. (2007). Table 9 gives the *absolute* position of this H₂O source together with our methyl formate position and positions from other studies of nearby objects. Matveenko et al. (2000) estimate a very small mass of 0.007 M_⊙ for their H₂O supermaser central source whose position is distinct from P1822/LBLS k. However, the proximity and youth of these two objects suggest that they might be a binary still in its forming phase.

P1822/LBLS k and associated supermaser could perhaps play a role in the observed distribution of methyl formate. Shocks are playing a central role in the vicinity of the H₂O supermaser whose excitation and properties are best explained by molecular collisions in shocked dense gas clumps. These shocks may well have released the methyl formate or its precursor from grain mantles. However the methyl formate clumps cannot be always tightly associated with all the H₂O maser spots because H₂O maser emission traces only the hottest and densest pockets of gas.

We suggest that four phenomena, observed in an area as small as 5'', may play a role in the release of the methyl formate molecule from ice grain mantles: i) bullets ejected 500 years ago (due to the BN-I-n encounter), ii) bipolar outflow from source I, iii) action from the star P1822/LBLS k, and iv) shocks linked to the excitation of the H₂O supermaser. From a statistical point of view it seems unlikely that the above suggestions are unrelated. However, the relative importance of these four phenomena in the MF production, their relative timing and their causal relationship deserve further study.

9. Conclusions

We have studied the distribution of the complex O-bearing molecule Methyl Formate (MF) HCOOCH₃ with medium to high angular resolution ($\approx 7''$ to $2''$) using interferometric data from the IRAM Plateau de Bure Interferometer. Our main results and conclusions are the following:

1. Our data sets include 21 well detected transitions of MF from $E_{\text{up}}=25$ K to $E_{\text{up}}=618$ K. A few more lines are present, still usable but partially blended with other lines. Only about 40% of the lines stronger than the weakest detected line appear free of blend. The line are optically thin ($\tau < 0.1$).
2. We confirm the detection of $v_t=1$ transitions. In this study, we used together $v_t=0$ and $v_t=1$ transitions to derive rotational temperatures.
3. We identify at least 28 MF concentrations. The most intense emissions, MF1 and MF2, arise from the Compact Ridge and the Hot Core-SW respectively. The emission toward MF1 is much stronger than toward MF2 for low energy levels whereas the emission at MF2 becomes stronger at high energy levels.
4. We have determined the MF temperature using rotational diagrams for the five main positions and deduced HCOOCH₃ column densities assuming LTE. Temperatures cover the range 80 to 170 K, and column densities 1.6×10^{16} to 1.6×10^{17} cm⁻².
5. In the course of the MF data reduction, we had to produce and subtract maps of the continuum emission, using line free channels. We used these continuum maps to identify four major clumps Ca to Cd, for which we derived dust masses in the range 0.01 to 0.05 M_⊙ using a dust temperature equal to the MF rotational temperature. Assuming a gas-to-dust ratio of 100 the gas masses are in the range 1 to 5 M_⊙.
6. MF gas velocities lie in the range 7-8 km s⁻¹. At some places two different velocity components are clearly seen and the high velocity component (around 9-10 km s⁻¹) has a linear North-South structure. We see no gas emission at the 5 km s⁻¹ velocity usually reported for the Hot Core: the gas we observe there is slightly higher in velocity and probably of the same nature as the gas we observe for the Compact Ridge.
7. We have searched for the two isomers of methyl formate but we did not detect them. We find an abundance ratio of less than 1/50 for acetic acid CH₃COOH and less than 1/(200-500) for glycolaldehyde CH₂OHCHO.
8. We have correlated the MF1/Compact Ridge emission with other gas tracers and with various Orion objects. A very clear association is found with 2.12 μm excited H₂ maps. This tends to confirm a scenario of MF production involving the release of molecules from ice mantles, either MF itself or a precursor (CH₃OH). Four possible origins have been identified for the excited H₂ emission and the MF production: shock from the "low-velocity" outflow from source I, shock from a bullet ejected during the supposed collision-explosion event 500 yr ago (Zapata et al. 2009), action of the young forming star Parenago 1822/LBLS k, or from the nearby source (and possible companion of the star) responsible for the H₂O supermaser (Matveenko et al. 2000). We can not conclude yet which of these four likely processes dominates the MF production but all may have contributed. To further analyze the Compact Ridge history more radio and IR high angular resolution images are needed. In the future, ALMA and adaptive optics on large ground based telescopes and space telescopes will provide the new data required to progress deeply in the understanding of the Orion-KL region.

The structure we find in Orion-KL might help to better understand the correlation previously found between cometary and interstellar ices (Bockelée-Morvan et al. 2000). In this correlation, sources of different nature *a priori*, "hot cores" on one side and a bipolar flow L1157 on the other side, both appeared as a good match of cometary ices. Shocks releasing molecules from icy grain mantles are in L1157 a major source of molecules in the gas phase. From the correlation we found between methyl formate and excited H₂ emission, this might also be the case in Orion-KL as well as in other hot cores.

Acknowledgements. We thank Laurent Margules and Brian Drouin for their spectroscopic knowledge and advices on HCOOCH₃. We thank Thierry Jacq for his dataset at 80 GHz and 203 GHz, and Daniel Rouan and Nathan Smith for their H₂ and 11 μm maps. Valuable contributions from David Field are gratefully acknowledged. We also thank Alexandre Faure for the discussion on lines in fundamental and excited torsional states. We thank the IRAM staff in Grenoble for their help to get and reduce the data. Finally we thank the anonymous referee for his helpful comments. This research has made use of the SIMBAD database and ALADIN software, operated at CDS, Strasbourg, France. This work was supported by CNRS national programs PCMI (Physics and Chemistry of the Interstellar Medium) and GDR Exobiology.

References

- Belloche, A., Menten, K. M., Comito, C., et al. 2008, A&A, 482, 179
 Beuther, H. & Nissen, H. D. 2008, ApJ, 679, L121
 Beuther, H., Zhang, Q., Greenhill, L. J., et al. 2004, ApJ, 616, L31
 Beuther, H., Zhang, Q., Greenhill, L. J., et al. 2005, ApJ, 632, 355
 Beuther, H., Zhang, Q., Reid, M. J., et al. 2006, ApJ, 636, 323
 Bisschop, S. E., Jørgensen, J. K., van Dishoeck, E. F., & de Wachter, E. B. M. 2007, A&A, 465, 913
 Blake, G. A., Mundy, L. G., Carlstrom, J. E., et al. 1996, ApJ, 472, L49+
 Blake, G. A., Sutton, E. C., Masson, C. R., & Phillips, T. G. 1987, ApJ, 315, 621
 Blake, G. A., Sutton, E. C., Masson, C. R., et al. 1984, ApJ, 286, 586
 Bockelée-Morvan, D., Lis, D. C., Wink, J. E., et al. 2000, A&A, 353, 1101
 Bonnarel, F., Fernique, P., Bienaymé, O., et al. 2000, A&AS, 143, 33
 Boucher, D., Burie, J., Bauer, A., Dubrulle, A., & Demaison, J. 1980, Journal of Physical and Chemical Reference Data, 9, 659
 Charnley, S. B. & Rodgers, S. D. 2005, in IAU Symposium, Vol. 231, Astrochemistry: Recent Successes and Current Challenges, ed. D. C. Lis, G. A. Blake, & E. Herbst, 237–246
 Colgan, S. W. J., Schultz, A. S. B., Kaufman, M. J., Erickson, E. F., & Hollenbach, D. J. 2007, ApJ, 671, 536

- Combes, F., Q-Rieu, N., & Wlodarczak, G. 1996, *A&A*, 308, 618
- Comito, C., Schilke, P., Phillips, T. G., et al. 2005, *ApJS*, 156, 127
- de Vicente, P., Martín-Pintado, J., Neri, R., & Rodríguez-Franco, A. 2002, *ApJ*, 574, L163
- Demichev, V. A. & Matveenko, L. I. 2009, *Astronomy Reports*, 53, 79
- Draine, B. T. 2010, *Physics of the Interstellar and Intergalactic Medium*, ed. Draine, B. T.
- Draine, B. T. & Lee, H. M. 1984, *ApJ*, 285, 89
- Eisner, J. A., Plambeck, R. L., Carpenter, J. M., et al. 2008, *ApJ*, 683, 304
- Faure, A. & Josselin, E. 2008, *A&A*, 492, 257
- Friedel, D. N. & Snyder, L. E. 2008, *ApJ*, 672, 962
- Garrod, R. T. & Herbst, E. 2006, *A&A*, 457, 927
- Garrod, R. T., Weaver, S. L. W., & Herbst, E. 2008, *ApJ*, 682, 283
- Gaume, R. A., Wilson, T. L., Vrba, F. J., Johnston, K. J., & Schmid-Burgk, J. 1998, *ApJ*, 493, 940
- Genzel, R. & Stutzki, J. 1989, *ARA&A*, 27, 41
- Getman, K. V., Flacomio, E., Broos, P. S., et al. 2005, *ApJS*, 160, 319
- Goddi, C., Greenhill, L. J., Chandler, C. J., et al. 2009, *ApJ*, 698, 1165
- Goddi, C., Humphreys, E. M. L., Greenhill, L. J., Chandler, C. J., & Matthews, L. D. 2010, *ArXiv e-prints*
- Gómez, L., Rodríguez, L. F., Loinard, L., et al. 2008, *ApJ*, 685, 333
- Gómez, L., Rodríguez, L. F., Loinard, L., et al. 2005, *ApJ*, 635, 1166
- Greenhill, L. J., Gezari, D. Y., Danchi, W. C., et al. 2004, *ApJ*, 605, L57
- Grosso, N., Feigelson, E. D., Getman, K. V., et al. 2005, *ApJS*, 160, 530
- Guélin, M., Brouillet, N., Cernicharo, J., Combes, F., & Wooten, A. 2008, *Ap&SS*, 313, 45
- Halfen, D. T., Apponi, A. J., Woolf, N., Polt, R., & Ziurys, L. M. 2006, *ApJ*, 639, 237
- Hillenbrand, L. A. & Carpenter, J. M. 2000, *ApJ*, 540, 236
- Hollis, J. M., Lovas, F. J., & Jewell, P. R. 2000, *ApJ*, 540, L107
- Hollis, J. M., Pedelty, J. A., Snyder, L. E., et al. 2003, *ApJ*, 588, 353
- Ilyushin, V., Kleiner, I., & Lovas, F. J. 2008, *Journal of Physical and Chemical Reference Data*, 37, 97
- Ilyushin, V., Kryvda, A., & Alekseev, E. 2009, *Journal of Molecular Spectroscopy*, 255, 32
- Irvine, W. M., Goldsmith, P. F., & Hjalmarson, A. 1987, *Astrophysics and Space Science Library*, Vol. 134, *Chemical abundances in molecular clouds*, ed. D. J. Hollenbach & H. A. Thronson Jr., 561–609
- Johansson, L. E. B., Andersson, C., Ellder, J., et al. 1984, *A&A*, 130, 227
- Kobayashi, K., Ogata, K., Tsunekawa, S., & Takano, S. 2007, *ApJ*, 657, L17
- Lacombe, F., Gendron, E., Rouan, D., et al. 2004, *A&A*, 417, L5
- Lada, C. J., Muench, A. A., Lada, E. A., & Alves, J. F. 2004, *AJ*, 128, 1254
- Lattalais, M., Pauzat, F., Ellinger, Y., & Ceccarelli, C. 2009, *ApJ*, 696, L133
- Leurini, S., Schilke, P., Menten, K. M., et al. 2004, *A&A*, 422, 573
- Liu, S., Girart, J. M., Remijan, A., & Snyder, L. E. 2002, *ApJ*, 576, 255
- Lonsdale, C. J., Becklin, E. E., Lee, T. J., & Stewart, J. M. 1982, *AJ*, 87, 1819
- Mathis, J. S., Rumpl, W., & Nordsieck, K. H. 1977, *ApJ*, 217, 425
- Matthews, L. D., Greenhill, L. J., Goddi, C., et al. 2010, *ApJ*, 708, 80
- Matveenko, L. I., Diamond, P. J., & Graham, D. A. 2000, *Astronomy Reports*, 44, 592
- Matveyenko, L. I., Graham, D. A., & Demichev, V. A. 2007, *Memorie della Societa Astronomica Italiana*, 78, 419
- Menten, K. M., Reid, M. J., Forbrich, J., & Brunthaler, A. 2007, *A&A*, 474, 515
- Menten, K. M., Walmsley, C. M., Henkel, C., & Wilson, T. L. 1988, *A&A*, 198, 253
- Mezger, P. G., Wink, J. E., & Zylka, R. 1990, *A&A*, 228, 95
- Muench, A. A., Lada, E. A., Lada, C. J., & Alves, J. 2002, *ApJ*, 573, 366
- Müller, H. S. P., Schlöder, F., Stutzki, J., & Winnewisser, G. 2005, *Journal of Molecular Structure*, 742, 215
- Müller, H. S. P., Thorwirth, S., Roth, D. A., & Winnewisser, G. 2001, *A&A*, 370, L49
- Nissen, H. D., Gustafsson, M., Lemaire, J. L., et al. 2007, *A&A*, 466, 949
- O'dell, C. R. 2001, in *Revista Mexicana de Astronomia y Astrofisica*, vol. 27, Vol. 10, *Revista Mexicana de Astronomia y Astrofisica Conference Series*, ed. J. Cantó & L. F. Rodríguez, 1–8
- O'Dell, C. R. & Henney, W. J. 2008, *AJ*, 136, 1566
- O'Dell, C. R., Henney, W. J., Abel, N. P., Ferland, G. J., & Arthur, S. J. 2009, *AJ*, 137, 367
- O'dell, C. R., Wen, Z., & Hu, X. 1993, *ApJ*, 410, 696
- Ossenkopf, V. & Henning, T. 1994, *A&A*, 291, 943
- Parento, P. P. 1954, *Trudy Gosudarstvennogo Astronomicheskogo Instituta*, 25, 3
- Parento, P. P. 1997, *VizieR Online Data Catalog*, 2171, 0
- Persson, C. M., Olofsson, A. O. H., Koning, N., et al. 2007, *A&A*, 476, 807
- Pickett, H. M. 1991, *Journal of Molecular Spectroscopy*, 148, 371
- Pickett, H. M., Poynter, I. R. L., Cohen, E. A., et al. 1998, *Journal of Quantitative Spectroscopy and Radiative Transfer*, 60, 883
- Plambeck, R. L. & Wright, M. C. H. 1988, *ApJ*, 330, L61
- Plambeck, R. L., Wright, M. C. H., Friedel, D. N., et al. 2009, *ApJ*, 704, L25
- Remijan, A., Snyder, L. E., Friedel, D. N., Liu, S., & Shah, R. Y. 2003, *ApJ*, 590, 314
- Robberto, M., Beckwith, S. V. W., Panagia, N., et al. 2005, *AJ*, 129, 1534
- Rodríguez, L. F., Poveda, A., Lizano, S., & Allen, C. 2005, *ApJ*, 627, L65
- Rohlfs, K. & Wilson, T. L. 2000, *Book Review: Tools of radio astronomy.- 3rd rev. ed.* Springer, 2000, Vol. 120, 289
- Schilke, P., Groesbeck, T. D., Blake, G. A., & Phillips, T. G. 1997, *ApJS*, 108, 301
- Shiao, Y., Looney, L. W., Remijan, A. J., Snyder, L. E., & Friedel, D. N. 2010, *ApJ*, 716, 286
- Shuping, R. Y., Morris, M., & Bally, J. 2004, *AJ*, 128, 363
- Simpson, J. P., Colgan, S. W. J., Erickson, E. F., Burton, M. G., & Schultz, A. S. B. 2006, *ApJ*, 642, 339
- Smith, N., Bally, J., Shuping, R. Y., Morris, M., & Kassis, M. 2005, *AJ*, 130, 1763
- Snyder, L. E., Lovas, F. J., Hollis, J. M., et al. 2005, *ApJ*, 619, 914
- Stolovy, S. R., Burton, M. G., Erickson, E. F., et al. 1998, *ApJ*, 492, L151+
- Tang, Y., Ho, P. T. P., Koch, P. M., & Rao, R. 2010, *ApJ*, 717, 1262
- Tielens, A. G. G. M. 2005, *The Physics and Chemistry of the Interstellar Medium*, ed. Tielens, A. G. G. M.
- Turner, B. E. 1991, *ApJS*, 76, 617
- van der Tak, F. F. S., van Dishoeck, E. F., & Caselli, P. 2000, *A&A*, 361, 327
- Wang, K., Kuan, Y., Liu, S., & Charnley, S. B. 2010, *ApJ*, 713, 1192
- Wang, S., Bergin, E. A., Crockett, N. R., et al. 2011, *ArXiv e-prints*
- Wilson, T. L., Gaume, R. A., Gensheimer, P., & Johnston, K. J. 2000, *ApJ*, 538, 665
- Wynn-Williams, C. G., Genzel, R., Becklin, E. E., & Downes, D. 1984, *ApJ*, 281, 172
- Zapata, L. A., Schmid-Burgk, J., Ho, P. T. P., Rodríguez, L. F., & Menten, K. M. 2009, *ApJ*, 704, L45
- Zapata, L. A., Schmid-Burgk, J., & Menten, K. M. 2010, *ArXiv e-prints*
- Ziurys, L. M. & McGonagle, D. 1993, *ApJS*, 89, 155

Table 10. Transitions of methyl formate observed with the Plateau de Bure Interferometer toward position MF1 in Orion-KL

N°	Set	Frequency (MHz)	Transition	E _{up} (K)	Sμ ² (D ²)	sigma (K)	v (km s ⁻¹)	Δv _{1/2} (km s ⁻¹)	T _B (K)	W (K km s ⁻¹)	N _{up} /g _{up} (10 ¹² cm ⁻²)	Source size (" x ")	PA(°)	Comments
(1)	(2)	(3)	(4)	(5)	(6)	(7)	(8)	(9)	(10)	(11)	(12)	(13)	(14)	(15)
1	1	80531.669(0.030)	9 _{2,8} – 9 _{0,9} E, (v _t =1)	216	0.6	0.05	-	-	≤0.15	≤0.6	≤1.04	-	-	not detected
2	1	80565.210(0.010)	10 _{2,8} – 9 _{3,7} E	36	1.1	0.05	7.9(0.1)	3.8(0.3)	0.51	2.0(0.1)	1.88	10.0x7.0	10	detected
3	1	80572.589(0.010)	10 _{2,8} – 9 _{3,7} A	36	1.1	0.05	8.0(0.5)	4.3(1.5)	0.47	2.2(0.5)	2.07	10.0x8.0	45	detected
4	2	80604.508(0.030)	12 _{9,3} – 13 _{8,5} E, (v _t =1)	288	0.2	0.09	-	-	≤0.31	≤1.3	≤6.73	-	-	blend
5	2	80652.521(0.010)	15 _{4,11} – 14 _{5,10} A	83	1.0	0.09	-	-	≤0.74	≤3.0	≤3.10	-	-	blend
6	3	101202.806(0.010)	9 _{1,9} – 8 _{0,8} A, (v _t =1)	213	4.2	0.04	7.6(0.1)	3.5(0.2)	1.02	3.8(0.2)	0.75	-	-	partial blend
7	3	101210.208(0.004)	24 _{3,21} – 25 _{2,24} A	187	0.04	0.04	-	-	≤0.12	≤0.4	≤8.68	-	-	not detected
8	3	101279.006(0.010)	9 _{1,9} – 8 _{0,8} E, (v _t =1)	212	4.0	0.04	7.8(0.1)	3.4(0.1)	1.18	4.3(0.1)	0.89	5.5x3.5	84	detected
9	3	101289.471(0.010)	29 _{9,20} – 28 _{10,19} A, (v _t =1)	498	1.8	0.04	-	-	≤0.12	≤0.4	≤0.18	-	-	not detected
10	3	101302.159(0.010)	25 _{6,19} – 25 _{5,20} A	219	11.1	0.04	7.6(0.1)	3.9(0.4)	3.11	12.8(1.0)	0.95	5.0x3.5	26	detected
11	3	101305.506(0.010)	25 _{6,19} – 25 _{5,20} E	219	11.1	0.04	7.8(0.2)	3.7(0.4)	2.65	10.4(1.0)	0.77	5.5x3.5	20	detected
12	3	101318.966(0.010)	13 _{3,11} – 13 _{2,12} E, (v _t =1)	246	3.2	0.04	7.8(0.1)	3.1(0.3)	0.70	2.3(0.2)	0.59	5.5x3.5	5	detected
13	3	101356.788(0.010)	15 _{2,13} – 15 _{1,14} A, (v _t =1)	263	3.5	0.04	-	-	≤0.59	≤2.1	≤0.49	-	-	blend
14	3	101370.505(0.010)	13 _{3,11} – 13 _{2,12} E	60	3.2	0.04	7.9(0.1)	3.7(0.1)	3.78	14.7(0.1)	3.78	5.0x3.5	5	detected
15	3	101414.746(0.010)	13 _{3,11} – 13 _{2,12} A	60	3.2	0.04	7.8(0.1)	3.6(0.1)	3.73	14.3(0.1)	3.68	5.0x3.5	5	detected
16	3	101418.330(0.001)	5 _{3,3} – 5 _{1,4} A, (v _t =1)	203	0.04	0.04	-	-	≤0.12	≤0.4	≤7.37	-	-	not detected
17	3	101477.421(0.010)	18 _{3,15} – 18 _{3,16} E	111	1.8	0.04	-	-	≤9.31	≤33.2	≤15.17	-	-	blend with H ₂ CS
18	3	101545.453(0.010)	18 _{3,15} – 18 _{3,16} A	111	1.8	0.04	7.8(0.1)	3.6(0.1)	1.80	6.9(0.2)	3.15	5.0x3.5	5	detected
19	3	101626.884(0.010)	9 _{1,9} – 8 _{0,8} E	25	4.1	0.04	-	-	≤5.96	≤21.2	≤4.25	-	-	blend with HCOOCH ₃ -A
20	3	101628.149(0.010)	9 _{1,9} – 8 _{0,8} A	25	4.1	0.04	-	-	≤5.47	≤19.5	≤3.91	-	-	blend with HCOOCH ₃ -E
21	4	105663.117(0.030)	19 _{13,7} – 20 _{12,9} E, (v _t =1)	412	0.4	0.02	-	-	≤0.06	≤0.1	≤0.20	-	-	not detected
22	4	105722.672(0.030)	10 _{4,6} – 10 _{3,8} E, (v _t =1)	230	0.5	0.02	-	-	≤0.11	≤0.2	≤0.32	-	-	blend
23	5	105810.803(0.030)	14 _{11,4} – 15 _{10,6} E	142	0.2	0.03	-	-	≤0.11	≤0.2	≤0.79	-	-	blend
24	5	105815.953(0.030)	3 _{3,1} – 2 _{2,0} E	10	0.2	0.03	7.6(0.1)	2.2(0.2)	0.39	0.9(0.1)	3.55	10.5x7.5	6	detected
25	5	105832.067(0.030)	14 _{11,3} – 15 _{10,5} E	142	0.2	0.03	7.9(0.1)	1.6(0.2)	0.20	0.4(0.1)	1.58	10.5x7.5	6	detected
26	6	110153.652(0.010)	10 _{1,10} – 9 _{1,9} A, (v _t =1)	218	25.1	0.12	-	-	≤8.08	≤9.7	≤0.29	-	-	blend with NH ₂ D
27	7	203349.158(0.006)	24 _{19,5} – 25 _{18,7} E	416	0.2	0.09	-	-	≤1.73	≤2.8	≤5.77	-	-	blend
28	7	203378.812(0.007)	24 _{19,6} – 25 _{18,8} E	416	0.2	0.09	-	-	≤5.64	≤9.2	≤18.94	-	-	blend
29	8	203427.575(0.100)	21 _{8,13} – 21 _{7,14} A, (v _t =1)	366	6.2	0.09	7.9(0.4)	1.7(0.8)	1.40	2.5(1.0)	0.17	4.5x2.5	45	detected
30	8	203435.554(0.100)	19 _{8,11} – 19 _{7,12} A	155	5.3	0.09	7.6(0.9)	1.6(0.9)	6.40	10.6(1.6)	0.82	5.0x3.5	65	detected
31	8	203471.840(0.05)	19 _{8,11} – 19 _{7,12} E	155	4.9	0.09	7.5(0.1)	1.6(0.1)	5.28	9.2(2.0)	0.77	5.0x3.5	40	detected
32	9	223435.416(0.001)	11 _{4,8} – 10 _{3,7} A, (v _t =1)	237	1.8	0.17	-	-	≤3.66	≤6.7	≤1.38	-	-	blend
33	9	223465.340(0.050)	11 _{4,8} – 10 _{3,7} E	50	2.1	0.17	7.6(0.1)	2.0(0.2)	10.74	22.5(1.9)	4.00	3.0x2.0	0	detected
34	9	223500.463(0.001)	11 _{4,8} – 10 _{3,7} A	50	1.8	0.17	7.4(0.1)	1.8(0.1)	11.49	21.8(1.7)	4.61	3.0x1.5	0	detected
35	9	223534.727(0.100)	18 _{5,14} – 17 _{5,13} E, (v _t =1)	305	41.6	0.17	7.4(0.1)	1.7(0.1)	10.25	18.5(0.8)	0.17	3.5x2.0	0	detected
36	9	223538.511(0.100)	43 _{8,35} – 43 _{7,36} E	618	13.9	0.17	-	-	≤0.51	≤0.9	≤0.02	-	-	not detected
37	9	223592.231(0.100)	43 _{8,35} – 43 _{7,36} A	618	13.9	0.17	-	-	≤0.91	≤1.7	≤0.05	-	-	blend
38	9	223618.470(0.007)	27 _{9,19} – 27 _{8,19} E, (v _t =1)	464	0.4	0.17	-	-	≤0.51	≤0.9	≤0.90	-	-	not detected
39	9	223624.496(0.100)	37 _{8,30} – 37 _{7,31} E	463	11.7	0.17	7.7(0.3)	1.8(0.6)	0.68	1.3(0.4)	0.04	-	-	partial blend

Table 10. continued.

N°	Set	Frequency (MHz)	Transition	E _{up} (K)	Sμ ² (D ²)	sigma (K)	v (km s ⁻¹)	Δv _{1/2} (km s ⁻¹)	T _B (K)	W (K km s ⁻¹)	N _{up} /g _{up} (10 ¹² cm ⁻²)	Source size (" x ")	PA(°)	Comments
(1)	(2)	(3)	(4)	(5)	(6)	(7)	(8)	(9)	(10)	(11)	(12)	(13)	(14)	(15)
40	9	223634.916(0.100)	37 _{8,30} – 37 _{7,31} A	463	11.7	0.17	-	-	≤2.06	≤3.8	≤0.12	-	-	blend
41	9	223642.180(0.001)	12 _{5,7} – 12 _{3,10} E	63	0.1	0.17	-	-	≤4.08	≤7.4	≤32.97	-	-	blend
42	9	223645.342(0.001)	12 _{5,7} – 12 _{3,10} A	63	0.1	0.17	-	-	≤1.66	≤3.0	≤11.23	-	-	blend
43	9	223651.592(0.007)	33 _{9,24} – 33 _{8,26} E, (v _t =1)	573	0.7	0.17	-	-	≤1.35	≤2.5	≤1.25	-	-	blend
44	9	223676.472(0.006)	35 _{7,29} – 35 _{5,30} A, (v _t =1)	593	3.0	0.17	-	-	≤2.09	≤3.8	≤0.47	-	-	blend
45	9	223782.081(0.007)	33 _{6,28} – 33 _{5,29} E, (v _t =1)	543	7.0	0.17	-	-	≤0.51	≤0.9	≤0.05	-	-	not detected
46	9	223821.523(0.002)	35 _{7,29} – 35 _{6,30} E	409	8.2	0.17	-	-	≤2.31	≤4.2	≤0.19	-	-	blend
47	9	223854.201(0.100)	35 _{7,29} – 35 _{6,30} A	409	10.1	0.17	-	-	≤4.63	≤8.4	≤0.31	-	-	blend
48	10	225689.371(0.008)	34 _{5,29} – 34 _{5,30} A, (v _t =1)	562	3.0	0.13	-	-	≤12.20	≤12.6	≤1.57	-	-	blend
49	10	225696.842(0.100)	20 _{1,19} – 19 _{1,18} E, (v _t =1)	307	50.2	0.13	-	-	≤16.8	≤17.4	≤0.13	-	-	blend
50	10	225702.857(0.100)	19 _{2,17} – 18 _{2,16} A, (v _t =1)	304	46.8	0.13	-	-	≤20.09	≤20.8	≤0.16	-	-	blend
51	10	225727.506(0.100)	6 _{6,1} – 5 _{5,0} A, (v _t =1)	224	3.1	0.13	-	-	≤4.04	≤4.2	≤0.50	-	-	blend
52	10	225727.506(0.100)	6 _{6,0} – 5 _{5,1} A, (v _t =1)	224	3.1	0.13	-	-	≤4.04	≤4.2	≤0.50	-	-	blend
53	11	225855.505(0.100)	6 _{6,1} – 5 _{5,1} E	36	3.1	0.10	7.6(0.1)	1.2(0.1)	6.84	9.1(0.1)	1.08	5.5x4.5	5	detected
54	11	225900.684(0.100)	6 _{6,0} – 5 _{5,0} E	36	3.1	0.10	-	-	≤12.74	≤13.2	≤1.57	-	-	blend with HDO
55	11	225928.659(0.100)	6 _{6,0} – 5 _{5,1} A	36	3.1	0.10	-	-	≤11.42	≤11.8	≤1.41	-	-	blend
56	11	225928.659(0.100)	6 _{6,1} – 5 _{5,0} A	36	3.1	0.10	-	-	≤11.42	≤11.8	≤1.41	-	-	blend
57	12	225999.145(0.100)	30 _{7,23} – 29 _{8,22} E	312	2.2	0.11	7.5(0.1)	0.9(0.3)	0.70	0.6(0.2)	0.10	5.0x3.5	0	detected
58	12	226061.796(0.100)	20 _{3,17} – 19 _{4,16} E, (v _t =1)	321	4.0	0.11	7.6(0.2)	1.0(0.5)	0.72	0.8(0.3)	0.07	5.5x3.5	25	detected
59	12	226077.920(0.001)	10 _{3,7} – 9 _{1,8} E	39	0.3	0.11	-	-	≤2.62	≤2.7	≤3.53	-	-	blend
60	12	226081.175(0.002)	30 _{7,23} – 29 _{8,22} A	312	1.8	0.11	-	-	≤0.71	≤0.7	≤0.14	-	-	blend
61	12	226087.718(0.007)	29 _{4,26} – 29 _{3,27} A, (v _t =1)	450	4.3	0.11	-	-	≤0.82	≤0.8	≤0.07	-	-	blend
62	12	226090.301(0.100)	19 _{2,17} – 18 _{2,16} E, (v _t =1)	303	47.0	0.11	-	-	≤9.62	≤9.6	≤0.08	-	-	blend
63	12	226112.470(0.007)	29 _{4,26} – 29 _{2,27} A, (v _t =1)	450	2.1	0.11	-	-	≤0.33	≤0.3	≤0.05	-	-	not detected
64	12	226125.600(0.001)	10 _{3,7} – 9 _{1,8} A	39	0.3	0.11	-	-	≤4.04	≤4.2	≤5.49	-	-	blend

Notes: (1) Numbering of the observed transitions with E_{upper} ≤ 650 K. (2) Reference number of the corresponding data set (see Table 1). (3) Frequencies and uncertainties taken from Ilyushin et al. (2009) and from the JPL database (<http://spec.jpl.nasa.gov/>). (4) Transitions in ground state (v_t=0). Transitions in torsional levels (v_t=1) are specified. (5) Energy of the upper level. (6) Line strength calculated by Ilyushin et al. (2009). For the transitions coming from the JPL database, the line strength is calculated from the formulae of Pickett et al. (1998). (7) Noise estimated from spectrum (1σ). (8) Lines with number 30, 31, 33, 34, 35, 41, 53 and 57 are decomposed. Only the first component is given here, other components are given in Table 3, except for lines 29, 39 and 58 because of the blend with the second component. (8), (9), (10) and (11) Velocity, linewidth at half intensity, brightness temperature and integrated intensities. The uncertainties are estimated with the CLASS software. (12) Column densities of the upper state of the transition with respect to the rotational degeneracy (2J_{up}+1). (13) and (14) Source size estimated at half flux density from detected transitions with spatial resolution allowing to isolate the source. (15) Blended lines are specified.

**Appendix A: Transitions of methyl formate
observed with the Plateau de Bure
Interferometer towards positions MF2 to MF5 in
Orion-KL.**

The following tables summarize the line parameters for all detected, blended or not detected transitions of the methyl formate molecule (HCOOCH₃) in all our PdBI data sets towards the emission peaks MF2 to MF5.

Table A.1. Transitions of methyl formate observed with the Plateau de Bure Interferometer toward position MF2 in Orion-KL

N°	Set	Frequency (MHz)	Transition	E _{up} (K)	Sμ ² (D ²)	sigma (K)	v (km s ⁻¹)	Δv _{1/2} (km s ⁻¹)	T _B (K)	W (K km s ⁻¹)	N _{up} /g _{up} (10 ¹² cm ⁻²)	Source size (" x "')	PA(°)	Comments
(1)	(2)	(3)	(4)	(5)	(6)	(7)	(8)	(9)	(10)	(11)	(12)	(13)	(14)	(15)
1	1	80531.669(0.030)	9 _{2,8} – 9 _{0,9} E, (v _t =1)	216	0.6	0.03	-	-	≤0.09	≤0.4	≤0.69	-	-	not detected
2	1	80565.210(0.010)	10 _{2,8} – 9 _{3,7} E	36	1.1	0.03	7.9(0.3)	4.4(0.5)	0.24	1.1(0.1)	1.04	-	-	detected
3	1	80572.589(0.010)	10 _{2,8} – 9 _{3,7} A	36	1.1	0.03	-	-	≤0.30	≤1.3	≤1.22	-	-	blend
4	2	80604.508(0.030)	12 _{9,3} – 13 _{8,5} E, (v _t =1)	288	0.2	0.10	-	-	≤8.03	≤35.3	≤182.73	-	-	blend
5	2	80652.521(0.010)	15 _{4,11} – 14 _{5,10} A	83	1.0	0.10	-	-	≤3.92	≤17.2	≤17.80	-	-	blend
6	3	101202.806(0.010)	9 _{1,9} – 8 _{0,8} A, (v _t =1)	213	4.2	0.04	-	-	≤0.64	≤2.6	≤0.51	-	-	blend
7	3	101210.208(0.004)	24 _{3,21} – 25 _{2,24} A	187	0.04	0.04	-	-	≤0.34	≤1.4	≤30.36	-	-	blend
8	3	101279.006(0.010)	9 _{1,9} – 8 _{0,8} E, (v _t =1)	212	4.0	0.04	7.6(0.7)	4.1(2.0)	0.64	2.8(1.0)	0.58	4.0x2.5	20	detected
9	3	101289.471(0.010)	29 _{9,20} – 28 _{10,19} A, (v _t =1)	498	1.8	0.04	-	-	≤0.12	≤0.5	≤0.23	-	-	not detected
10	3	101302.159(0.010)	25 _{6,19} – 25 _{5,20} A	219	11.1	0.04	7.1(0.4)	4.3(1.0)	2.09	9.6(1.9)	0.71	-	-	partial blend
11	3	101305.506(0.010)	25 _{6,19} – 25 _{5,20} E	219	11.1	0.04	7.5(0.8)	4.4(2.2)	1.58	7.3(3.0)	0.54	5.0x2.5	20	detected
12	3	101318.966(0.010)	13 _{3,11} – 13 _{2,12} E, (v _t =1)	246	3.2	0.04	7.7(0.5)	3.8(1.2)	0.50	2.0(0.5)	0.51	5.5x2.5	35	detected
13	3	101356.788(0.010)	15 _{2,13} – 15 _{1,14} A, (v _t =1)	263	3.5	0.04	-	-	≤0.56	≤2.2	≤0.52	-	-	blend
14	3	101370.505(0.010)	13 _{3,11} – 13 _{2,12} E	60	3.2	0.04	7.5(0.1)	3.8(0.1)	1.66	6.6(0.2)	1.70	4.5x2.5	35	detected
15	3	101414.746(0.010)	13 _{3,11} – 13 _{2,12} A	60	3.2	0.04	7.5(0.1)	4.1(0.3)	1.49	6.6(0.4)	1.70	4.5x2.5	35	detected
16	3	101418.330(0.001)	5 _{3,3} – 5 _{1,4} A, (v _t =1)	203	0.04	0.04	-	-	≤0.12	≤0.5	≤9.22	-	-	not detected
17	3	101477.421(0.010)	18 _{3,15} – 18 _{3,16} E	111	1.8	0.04	-	-	≤9.17	≤36.7	≤16.77	-	-	blend with H ₂ CS
18	3	101545.453(0.010)	18 _{3,15} – 18 _{3,16} A	111	1.8	0.04	7.6(0.3)	3.5(0.6)	1.03	3.8(0.6)	1.73	4.5x2.5	35	detected
19	3	101626.884(0.010)	9 _{1,9} – 8 _{0,8} E	25	4.1	0.04	-	-	≤2.80	≤11.2	≤2.24	-	-	blend with HCOOC _{1,1} -A
20	3	101628.149(0.010)	9 _{1,9} – 8 _{0,8} A	25	4.1	0.04	-	-	≤2.97	≤11.9	≤2.38	-	-	blend with HCOOC _{1,1} -E
21	4	105663.117(0.030)	19 _{13,7} – 20 _{12,9} E, (v _t =1)	412	0.4	0.02	-	-	≤0.19	≤0.6	≤1.18	-	-	blend
22	4	105722.672(0.030)	10 _{4,6} – 10 _{3,8} E, (v _t =1)	230	0.5	0.02	-	-	≤0.06	≤0.2	≤0.32	-	-	not detected
23	5	105810.803(0.030)	14 _{11,4} – 15 _{10,6} E	142	0.2	0.02	-	-	≤0.09	≤0.3	≤1.18	-	-	blend
24	5	105815.953(0.030)	3 _{3,1} – 2 _{2,0} E	10	0.2	0.02	7.7(0.2)	3.0(0.9)	0.17	0.5(0.1)	1.97	-	-	detected
25	5	105832.067(0.030)	14 _{11,3} – 15 _{10,5} E	142	0.2	0.02	-	-	≤0.23	≤0.7	≤2.76	-	-	blend
26	6	110153.652(0.010)	10 _{1,10} – 9 _{1,9} A, (v _t =1)	218	25.1	0.10	-	-	≤8.63	≤9.5	≤0.29	-	-	blend with NH ₂ D
27	7	203349.158(0.006)	24 _{19,5} – 25 _{18,7} E	416	0.2	0.07	-	-	≤3.35	≤8.3	≤17.09	-	-	blend
28	7	203378.812(0.007)	24 _{19,6} – 25 _{18,8} E	416	0.2	0.07	-	-	≤20.42	≤50.4	≤103.77	-	-	blend
29	8	203427.575(0.100)	21 _{8,13} – 21 _{7,14} A, (v _t =1)	366	6.2	0.07	7.8(0.4)	2.3(1.0)	1.14	2.7(1.1)	0.18	6.5x3.0	35	detected
30	8	203435.554(0.100)	19 _{8,11} – 19 _{7,12} A	155	5.3	0.07	7.8(0.2)	2.6(0.6)	4.24	11.8(2.0)	0.91	6.0x2.5	25	detected
31	8	203471.840(0.050)	19 _{8,11} – 19 _{7,12} E	155	4.9	0.07	7.6(0.5)	2.5(1.3)	3.22	8.5(3.4)	0.71	6.0x2.5	25	detected
32	9	223435.416(0.001)	11 _{4,8} – 10 _{3,7} A, (v _t =1)	237	1.8	0.25	-	-	≤5.75	≤13.9	≤2.86	-	-	blend
33	9	223465.340(0.050)	11 _{4,8} – 10 _{3,7} E	50	2.1	0.25	7.8(0.1)	2.2(0.2)	5.62	12.9(1.3)	2.29	2.5x1.2	10	detected
34	9	223500.463(0.001)	11 _{4,8} – 10 _{3,7} A	50	1.8	0.25	7.5(0.2)	2.3(0.5)	5.71	13.7(2.8)	2.90	2.5x1.2	10	detected
35	9	223534.727(0.100)	18 _{5,14} – 17 _{5,13} E, (v _t =1)	305	41.6	0.25	7.5(0.1)	2.6(0.3)	12.67	35.5(3.5)	0.32	-	-	partial blend
36	9	223538.511(0.100)	43 _{8,35} – 43 _{7,36} E	618	13.9	0.25	-	-	≤1.23	≤3.0	≤0.08	-	-	blend
37	9	223592.231(0.100)	43 _{8,35} – 43 _{7,36} A	618	13.9	0.25	7.8(0.9)	2.2(1.8)	1.22	2.8(2.2)	0.08	2.0x1.2	20	detected
38	9	223618.470(0.007)	27 _{9,19} – 27 _{8,19} E, (v _t =1)	464	0.4	0.25	-	-	≤0.75	≤1.8	≤1.80	-	-	not detected
39	9	223624.496(0.100)	37 _{8,30} – 37 _{7,31} E	463	11.7	0.25	-	-	≤0.92	≤2.2	≤0.07	-	-	blend
40	9	223634.916(0.100)	37 _{8,30} – 37 _{7,31} A	463	11.7	0.25	-	-	≤1.83	≤4.2	≤0.13	-	-	blend

C. Favre et al.: HCOOC_{1,1} as a probe of temperature and structure of Orion-KL
 Online Material p 2

Table A.1. continued.

N°	Set	Frequency (MHz)	Transition	E _{up} (K)	Sμ ² (D ²)	sigma (K)	v (km s ⁻¹)	Δv _{1/2} (km s ⁻¹)	T _B (K)	W (K km s ⁻¹)	N _{up} /g _{up} (10 ¹² cm ⁻²)	Source size (" x ")	PA(°)	Comments
(1)	(2)	(3)	(4)	(5)	(6)	(7)	(8)	(9)	(10)	(11)	(12)	(13)	(14)	(15)
41	9	223642.180(0.001)	12 _{5,7} – 12 _{3,10} E	63	0.1	0.25	-	-	≤3.58	≤8.7	≤38.77	-	-	blend
42	9	223645.342(0.001)	12 _{5,7} – 12 _{3,10} A	63	0.1	0.25	-	-	≤0.83	≤2.0	≤7.49	-	-	blend
43	9	223651.592(0.007)	33 _{9,24} – 33 _{8,26} E, (v _t =1)	573	0.7	0.25	-	-	≤1.88	≤4.5	≤2.25	-	-	blend
44	9	223676.472(0.006)	35 _{7,29} – 35 _{5,30} A, (v _t =1)	593	3.0	0.25	-	-	≤3.42	≤8.3	≤1.02	-	-	blend
45	9	223782.081(0.007)	33 _{6,28} – 33 _{5,29} E, (v _t =1)	543	7.0	0.25	-	-	≤0.75	≤1.8	≤0.10	-	-	not detected
46	9	223821.523(0.002)	35 _{7,29} – 35 _{6,30} E	409	8.2	0.25	-	-	≤2.06	≤5.0	≤0.23	-	-	blend
47	9	223854.201(0.100)	35 _{7,29} – 35 _{6,30} A	409	10.1	0.25	-	-	≤2.33	≤5.6	≤0.21	-	-	blend
48	10	225689.371(0.008)	34 _{5,29} – 34 _{5,30} A, (v _t =1)	562	3.0	0.10	-	-	≤17.26	≤19.0	≤2.37	-	-	blend
49	10	225696.842(0.100)	20 _{1,19} – 19 _{1,18} E, (v _t =1)	307	50.2	0.10	-	-	≤24.50	≤27.0	≤0.20	-	-	blend
50	10	225702.857(0.100)	19 _{2,17} – 18 _{2,16} A, (v _t =1)	304	46.8	0.10	-	-	≤43.23	≤47.6	≤0.38	-	-	blend
51	10	225727.506(0.100)	6 _{6,1} – 5 _{5,0} A, (v _t =1)	224	3.1	0.10	-	-	≤4.61	≤5.1	≤0.61	-	-	blend
52	10	225727.506(0.100)	6 _{6,0} – 5 _{5,1} A, (v _t =1)	224	3.1	0.10	-	-	≤4.61	≤5.1	≤0.61	-	-	blend
53	11	225855.505(0.100)	6 _{6,1} – 5 _{5,1} E	36	3.1	0.11	-	-	≤3.68	≤4.0	≤0.48	-	-	blend
54	11	225900.684(0.100)	6 _{6,0} – 5 _{5,0} E	36	3.1	0.11	-	-	≤19.23	≤21.2	≤2.53	-	-	blend with HDO
55	11	225928.659(0.100)	6 _{6,0} – 5 _{5,1} A	36	3.1	0.11	-	-	≤5.80	≤6.4	≤0.76	-	-	blend
56	11	225928.659(0.100)	6 _{6,1} – 5 _{5,0} A	36	3.1	0.11	-	-	≤5.80	≤6.4	≤0.76	-	-	blend
57	12	225999.145(0.100)	30 _{7,23} – 29 _{8,22} E	312	2.2	0.10	-	-	≤0.30	≤0.3	≤0.05	-	-	not detected
58	12	226061.796(0.100)	20 _{3,17} – 19 _{4,16} E, (v _t =1)	321	4.0	0.10	7.8(0.3)	1.1(0.6)	0.42	0.5(0.2)	0.05	-	-	partial blend
59	12	226077.920(0.001)	10 _{3,7} – 9 _{1,8} E	39	0.3	0.10	-	-	≤2.52	≤2.8	≤3.66	-	-	blend
60	12	226081.175(0.002)	30 _{7,23} – 29 _{8,22} A	312	1.8	0.10	-	-	≤0.42	≤0.5	≤0.10	-	-	blend
61	12	226087.718(0.007)	29 _{4,26} – 29 _{3,27} A, (v _t =1)	450	4.3	0.10	-	-	≤0.73	≤0.8	≤0.07	-	-	blend
62	12	226090.301(0.100)	19 _{2,17} – 18 _{2,16} E, (v _t =1)	303	47.0	0.10	-	-	≤7.67	≤8.4	≤0.07	-	-	blend
63	12	226112.470(0.007)	29 _{4,26} – 29 _{2,27} A, (v _t =1)	450	2.1	0.10	-	-	≤0.53	≤0.6	≤0.11	-	-	blend
64	12	226125.600(0.001)	10 _{3,7} – 9 _{1,8} A	39	0.3	0.10	-	-	≤3.22	≤3.5	≤4.58	-	-	blend

Notes: (1) Numbering of the observed transitions with E_{upper} ≤ 650 K. (2) Reference number of the corresponding data set (see Table 1). (3) Frequencies and uncertainties taken from Ilyushin et al. (2009) and from the JPL database (<http://spec.jpl.nasa.gov/>). (4) Transitions in ground state (v_t=0). Transitions in torsional levels (v_t=1) are specified. (5) Energy of the upper level. (6) Line strength calculated by Ilyushin et al. (2009). For the transitions coming from the JPL database, the line strength is calculated from the formulae of Pickett et al. (1998). (7) Noise estimated from spectrum (1σ). (8), (9), (10) and (11) Velocity, linewidth at half intensity, brightness temperature and integrated intensities. The uncertainties are estimated with the CLASS software. (12) Column densities of the upper state of the transition with respect to the rotational degeneracy (2J_{up}+1). (13) and (14) Source size estimated at half flux density from detected transitions with spatial resolution allowing to isolate the source. (15) Blended lines are specified.

Table A.2. Transitions of methyl formate observed with the Plateau de Bure Interferometer toward position MF3 in Orion-KL

N°	Set	Frequency (MHz)	Transition	E _{up} (K)	Sμ ² (D ²)	sigma (K)	v (km s ⁻¹)	Δv _{1/2} (km s ⁻¹)	T _B (K)	W (K km s ⁻¹)	N _{up} /g _{up} (10 ¹² cm ⁻²)	Source size (" x ")	PA(°)	Comments
(1)	(2)	(3)	(4)	(5)	(6)	(7)	(8)	(9)	(10)	(11)	(12)	(13)	(14)	(15)
1	1	80531.669(0.030)	9 _{2,8} – 9 _{0,9} E, (v _t =1)	216	0.6	0.02	-	-	≤0.06	≤0.2	≤0.35	-	-	not detected
2	1	80565.210(0.010)	10 _{2,8} – 9 _{3,7} E	36	1.1	0.02	7.8(0.1)	3.8(0.2)	0.43	1.8(0.1)	1.69	10.0x7.0	10	detected
3	1	80572.589(0.010)	10 _{2,8} – 9 _{3,7} A	36	1.1	0.02	-	-	≤0.39	≤1.5	≤1.41	-	-	blend
4	2	80604.508(0.030)	12 _{9,3} – 13 _{8,5} E, (v _t =1)	288	0.2	0.06	-	-	≤3.20	≤12.2	≤63.15	-	-	blend
5	2	80652.521(0.010)	15 _{4,11} – 14 _{5,10} A	83	1.0	0.06	-	-	≤1.94	≤7.4	≤7.66	-	-	blend
6	3	101202.806(0.010)	9 _{1,9} – 8 _{0,8} A, (v _t =1)	213	4.2	0.04	8.0(0.1)	4.0(0.2)	0.51	2.2(0.1)	0.43	-	-	partial blend
7	3	101210.208(0.004)	24 _{3,21} – 25 _{2,24} A	187	0.04	0.04	-	-	≤0.12	≤0.5	≤10.84	-	-	not detected
8	3	101279.006(0.010)	9 _{1,9} – 8 _{0,8} E, (v _t =1)	212	4.0	0.04	7.5(0.4)	3.5(0.9)	0.55	2.0(0.4)	0.41	-	-	detected
9	3	101289.471(0.010)	29 _{9,20} – 28 _{10,19} A, (v _t =1)	498	1.8	0.04	-	-	≤0.12	≤0.5	≤0.23	-	-	not detected
10	3	101302.159(0.010)	25 _{6,19} – 25 _{5,20} A	219	11.1	0.04	7.4(0.4)	4.1(1.2)	1.76	7.6(1.8)	0.56	-	-	partial blend
11	3	101305.506(0.010)	25 _{6,19} – 25 _{5,20} E	219	11.1	0.04	7.8(0.2)	4.0(0.6)	1.33	5.7(0.6)	0.42	-	-	detected
12	3	101318.966(0.010)	13 _{3,11} – 13 _{2,12} E, (v _t =1)	246	3.2	0.04	7.5(0.3)	3.2(0.8)	0.28	1.0(0.2)	0.26	-	-	detected
13	3	101356.788(0.010)	15 _{2,13} – 15 _{1,14} A, (v _t =1)	263	3.5	0.04	-	-	≤0.30	≤1.1	≤0.26	-	-	blend
14	3	101370.505(0.010)	13 _{3,11} – 13 _{2,12} E	60	3.2	0.04	7.7(0.1)	3.8(0.1)	1.77	7.2(0.1)	1.85	-	-	detected
15	3	101414.746(0.010)	13 _{3,11} – 13 _{2,12} A	60	3.2	0.04	7.7(0.1)	3.7(0.1)	1.83	7.2(0.2)	1.85	-	-	detected
16	3	101418.330(0.001)	5 _{3,3} – 5 _{1,4} A, (v _t =1)	203	0.04	0.04	-	-	≤0.12	≤0.5	≤9.22	-	-	not detected
17	3	101477.421(0.010)	18 _{3,15} – 18 _{3,16} E	111	1.8	0.04	-	-	≤10.05	≤37.8	≤17.27	-	-	blend with H ₂ CS
18	3	101545.453(0.010)	18 _{3,15} – 18 _{3,16} A	111	1.8	0.04	7.9(0.1)	3.8(0.2)	0.83	3.4(0.1)	1.55	-	-	detected
19	3	101626.884(0.010)	9 _{1,9} – 8 _{0,8} E	25	4.1	0.04	-	-	≤3.21	≤12.1	≤2.42	-	-	blend with HCOOC ₁₃ -A
20	3	101628.149(0.010)	9 _{1,9} – 8 _{0,8} A	25	4.1	0.04	-	-	≤3.23	≤12.2	≤2.44	-	-	blend with HCOOC ₁₃ -E
21	4	105663.117(0.030)	19 _{13,7} – 20 _{12,9} E, (v _t =1)	412	0.4	0.02	7.6(0.3)	2.1(0.8)	0.09	0.2(0.1)	0.39	11x8.5	6	detected
22	4	105722.672(0.030)	10 _{4,6} – 10 _{3,8} E, (v _t =1)	230	0.5	0.02	-	-	≤0.11	≤0.2	≤0.32	-	-	blend
23	5	105810.803(0.030)	14 _{11,4} – 15 _{10,6} E	142	0.2	0.02	-	-	≤0.12	≤0.2	≤0.79	-	-	blend
24	5	105815.953(0.030)	3 _{3,1} – 2 _{2,0} E	10	0.2	0.02	7.6(0.1)	2.1(0.3)	0.35	0.8(0.1)	3.15	10.5x8.5	6	detected
25	5	105832.067(0.030)	14 _{11,3} – 15 _{10,5} E	142	0.2	0.02	7.7(0.1)	1.5(0.2)	0.17	0.3(0.1)	1.18	10.0x7.5	6	detected
26	6	110153.652(0.010)	10 _{1,10} – 9 _{1,9} A, (v _t =1)	218	25.1	0.12	-	-	≤6.40	≤12.2	≤0.37	-	-	blend with NH ₂ D
27	7	203349.158(0.006)	24 _{19,5} – 25 _{18,7} E	416	0.2	0.20	-	-	≤0.60	≤1.0	≤2.06	-	-	not detected
28	7	203378.812(0.007)	24 _{19,6} – 25 _{18,8} E	416	0.2	0.20	-	-	≤2.94	≤5.0	≤10.29	-	-	blend
29	8	203427.575(0.100)	21 _{8,13} – 21 _{7,14} A, (v _t =1)	366	6.2	0.20	-	-	≤0.60	≤1.0	≤0.07	-	-	not detected
30	8	203435.554(0.100)	19 _{8,11} – 19 _{7,12} A	155	5.3	0.20	7.7(0.1)	1.7(0.1)	3.33	6.1(0.3)	0.47	-	-	detected
31	8	203471.840(0.050)	19 _{8,11} – 19 _{7,12} E	155	4.9	0.20	7.6(0.1)	1.7(0.3)	2.73	4.8(0.8)	0.40	-	-	detected
32	9	223435.416(0.001)	11 _{4,8} – 10 _{3,7} A, (v _t =1)	237	1.8	0.30	-	-	≤0.90	≤1.4	≤0.29	-	-	not detected
33	9	223465.340(0.050)	11 _{4,8} – 10 _{3,7} E	50	2.1	0.30	7.7(0.1)	1.7(0.3)	3.24	5.8(1.2)	1.03	-	-	partial blend
34	9	223500.463(0.001)	11 _{4,8} – 10 _{3,7} A	50	1.8	0.30	7.7(0.1)	1.2(0.1)	4.02	5.2(0.3)	1.10	3.0x1.5	0	detected
35	9	223534.727(0.100)	18 _{5,14} – 17 _{5,13} E, (v _t =1)	305	41.6	0.30	7.7(0.1)	1.6(0.1)	3.49	6.0(0.4)	0.05	2.5x1.5	0	detected
36	9	223538.511(0.100)	43 _{8,35} – 43 _{7,36} E	618	13.9	0.30	-	-	≤0.90	≤1.4	≤0.04	-	-	not detected
37	9	223592.231(0.100)	43 _{8,35} – 43 _{7,36} A	618	13.9	0.30	-	-	≤0.90	≤1.4	≤0.04	-	-	not detected
38	9	223618.470(0.007)	27 _{9,19} – 27 _{8,19} E, (v _t =1)	464	0.4	0.30	-	-	≤0.90	≤1.4	≤1.40	-	-	not detected
39	9	223624.496(0.100)	37 _{8,30} – 37 _{7,31} E	463	11.7	0.30	-	-	≤0.90	≤1.4	≤0.04	-	-	not detected
40	9	223634.916(0.100)	37 _{8,30} – 37 _{7,31} A	463	11.7	0.30	-	-	≤0.90	≤1.4	≤0.04	-	-	not detected

Table A.2. continued.

N°	Set	Frequency (MHz)	Transition	E _{up} (K)	Sμ ² (D ²)	sigma (K)	v (km s ⁻¹)	Δv _{1/2} (km s ⁻¹)	T _B (K)	W (K km s ⁻¹)	N _{up} /g _{up} (10 ¹² cm ⁻²)	Source size (" x ")	PA(°)	Comments
(1)	(2)	(3)	(4)	(5)	(6)	(7)	(8)	(9)	(10)	(11)	(12)	(13)	(14)	(15)
41	9	223642.180(0.001)	12 _{5,7} – 12 _{3,10} E	63	0.1	0.30	-	-	≤1.13	≤1.7	≤7.57	-	-	blend
42	9	223645.342(0.001)	12 _{5,7} – 12 _{3,10} A	63	0.1	0.30	-	-	≤0.90	≤1.4	≤5.24	-	-	not detected
43	9	223651.592(0.007)	33 _{9,24} – 33 _{8,26} E, (v _t =1)	573	0.7	0.30	-	-	≤0.90	≤1.4	≤0.70	-	-	not detected
44	9	223676.472(0.006)	35 _{7,29} – 35 _{5,30} A, (v _t =1)	593	3.0	0.30	-	-	≤0.90	≤1.4	≤0.17	-	-	not detected
45	9	223782.081(0.007)	33 _{6,28} – 33 _{5,29} E, (v _t =1)	543	7.0	0.30	-	-	≤0.90	≤1.4	≤0.08	-	-	not detected
46	9	223821.523(0.002)	35 _{7,29} – 35 _{6,30} E	409	8.2	0.30	-	-	≤0.90	≤1.4	≤0.06	-	-	not detected
47	9	223854.201(0.100)	35 _{7,29} – 35 _{6,30} A	409	10.1	0.30	-	-	≤0.90	≤1.4	≤0.05	-	-	not detected
48	10	225689.371(0.008)	34 _{5,29} – 34 _{5,30} A, (v _t =1)	562	3.0	0.14	-	-	≤13.06	≤22.2	≤2.77	-	-	blend
49	10	225696.842(0.100)	20 _{1,19} – 19 _{1,18} E, (v _t =1)	307	50.2	0.14	-	-	≤22.85	≤38.8	≤0.29	-	-	blend
50	10	225702.857(0.100)	19 _{2,17} – 18 _{2,16} A, (v _t =1)	304	46.8	0.14	-	-	≤25.75	≤43.8	≤0.35	-	-	blend
51	10	225727.506(0.100)	6 _{6,1} – 5 _{5,0} A, (v _t =1)	224	3.1	0.14	-	-	≤3.20	≤5.4	≤0.64	-	-	blend
52	10	225727.506(0.100)	6 _{6,0} – 5 _{5,1} A, (v _t =1)	224	3.1	0.14	-	-	≤3.20	≤5.4	≤0.64	-	-	blend
53	11	225855.505(0.100)	6 _{6,1} – 5 _{5,1} E	36	3.1	0.09	-	-	≤5.27	≤9.0	≤1.07	-	-	blend
54	11	225900.684(0.100)	6 _{6,0} – 5 _{5,0} E	36	3.1	0.09	-	-	≤11.08	≤18.8	≤2.24	-	-	blend with HDO
55	11	225928.659(0.100)	6 _{6,0} – 5 _{5,1} A	36	3.1	0.09	-	-	≤7.14	≤12.1	≤1.44	-	-	blend
56	11	225928.659(0.100)	6 _{6,1} – 5 _{5,0} A	36	3.1	0.09	-	-	≤7.14	≤12.1	≤1.44	-	-	blend
57	12	225999.145(0.100)	30 _{7,23} – 29 _{8,22} E	312	2.2	0.12	-	-	≤0.36	≤0.6	≤0.10	-	-	not detected
58	12	226061.796(0.100)	20 _{3,17} – 19 _{4,16} E, (v _t =1)	321	4.0	0.12	-	-	≤0.46	≤0.8	≤0.07	-	-	blend
59	12	226077.920(0.001)	10 _{3,7} – 9 _{1,8} E	39	0.3	0.12	-	-	≤2.48	≤4.2	≤5.50	-	-	blend
60	12	226081.175(0.002)	30 _{7,23} – 29 _{8,22} A	312	1.8	0.12	-	-	≤0.36	≤0.6	≤0.12	-	-	not detected
61	12	226087.718(0.007)	29 _{4,26} – 29 _{3,27} A, (v _t =1)	450	4.3	0.12	-	-	≤0.46	≤0.8	≤0.07	-	-	blend
62	12	226090.301(0.100)	19 _{2,17} – 18 _{2,16} E, (v _t =1)	303	47.0	0.12	-	-	≤6.10	≤10.4	≤0.08	-	-	blend
63	12	226112.470(0.007)	29 _{4,26} – 29 _{2,27} A, (v _t =1)	450	2.1	0.12	-	-	≤0.36	≤0.6	≤0.11	-	-	not detected
64	12	226125.600(0.001)	10 _{3,7} – 9 _{1,8} A	39	0.3	0.12	-	-	≤1.83	≤3.1	≤4.05	-	-	blend

Notes: (1) Numbering of the observed transitions with E_{upper} ≤ 650 K. (2) Reference number of the corresponding data set (see Table 1). (3) Frequencies and uncertainties taken from Ilyushin et al. (2009) and from the JPL database (<http://spec.jpl.nasa.gov/>). (4) Transitions in ground state (v_t=0). Transitions in torsional levels (v_t=1) are specified. (5) Energy of the upper level. (6) Line strength calculated by Ilyushin et al. (2009). For the transitions coming from the JPL database, the line strength is calculated from the formulae of Pickett et al. (1998). (7) Noise estimated from spectrum (1σ). (8), (9), (10) and (11) Velocity, linewidth at half intensity, brightness temperature and integrated intensities. The uncertainties are estimated with the CLASS software. (12) Column densities of the upper state of the transition with respect to the rotational degeneracy (2J_{up}+1). (13) and (14) Source size estimated at half flux density from detected transitions with spatial resolution allowing to isolate the source. (15) Blended lines are specified.

Table A.3. Transitions of methyl formate observed with the Plateau de Bure Interferometer toward position MF4 in Orion-KL

N°	Set	Frequency (MHz)	Transition	E _{up} (K)	Sμ ² (D ²)	sigma (K)	v (km s ⁻¹)	Δv _{1/2} (km s ⁻¹)	T _B (K)	W (K km s ⁻¹)	N _{up} /g _{up} (10 ¹² cm ⁻²)	Source size (" x " PA(°))	Comments	
(1)	(2)	(3)	(4)	(5)	(6)	(7)	(8)	(9)	(10)	(11)	(12)	(13)	(14)	(15)
1	1	80531.669(0.030)	9 _{2,8} – 9 _{0,9} E, (v _t =1)	216	0.6	0.02	-	-	≤0.06	≤0.2	≤0.35	-	-	not detected
2	1	80565.210(0.010)	10 _{2,8} – 9 _{3,7} E	36	1.1	0.02	8.1(0.2)	4.0(0.4)	0.28	1.2(0.1)	1.13	-	-	detected
3	1	80572.589(0.010)	10 _{2,8} – 9 _{3,7} A	36	1.1	0.02	-	-	≤0.33	≤1.3	≤1.22	-	-	blend
4	2	80604.508(0.030)	12 _{9,3} – 13 _{8,5} E, (v _t =1)	288	0.2	0.12	-	-	≤6.26	≤25.0	≤129.41	-	-	blend
5	2	80652.521(0.010)	15 _{4,11} – 14 _{5,10} A	83	1.0	0.12	-	-	≤2.33	≤9.3	≤9.62	-	-	blend
6	3	101202.806(0.010)	9 _{1,9} – 8 _{0,8} A, (v _t =1)	213	4.2	0.03	-	-	≤0.42	≤1.8	≤0.35	-	-	blend
7	3	101210.208(0.004)	24 _{3,21} – 25 _{2,24} A	187	0.04	0.03	-	-	≤0.37	≤1.6	≤34.70	-	-	blend
8	3	101279.006(0.010)	9 _{1,9} – 8 _{0,8} E, (v _t =1)	212	4.0	0.03	-	-	≤0.42	≤1.8	≤0.37	-	-	blend
9	3	101289.471(0.010)	29 _{9,20} – 28 _{10,19} A, (v _t =1)	498	1.8	0.03	-	-	≤0.09	≤0.4	≤0.18	-	-	not detected
10	3	101302.159(0.010)	25 _{6,19} – 25 _{5,20} A	219	11.1	0.03	8.0(0.1)	4.3(0.2)	1.07	4.9(0.3)	0.36	-	-	partial blend
11	3	101305.506(0.010)	25 _{6,19} – 25 _{5,20} E	219	11.1	0.03	8.1(0.2)	4.5(0.6)	1.04	4.9(0.6)	0.36	5.0x2.7	0	detected
12	3	101318.966(0.010)	13 _{3,11} – 13 _{2,12} E, (v _t =1)	246	3.2	0.03	8.4(0.3)	3.9(0.6)	0.23	0.9(0.1)	0.23	4.5x2.7	20	detected
13	3	101356.788(0.010)	15 _{2,13} – 15 _{1,14} A, (v _t =1)	263	3.5	0.03	-	-	≤0.29	≤1.2	≤0.28	-	-	blend
14	3	101370.505(0.010)	13 _{3,11} – 13 _{2,12} E	60	3.2	0.03	7.9(0.1)	4.0(0.1)	1.27	5.4(0.1)	1.39	-	-	partial blend
15	3	101414.746(0.010)	13 _{3,11} – 13 _{2,12} A	60	3.2	0.03	8.2(0.1)	4.6(0.1)	1.36	6.6(0.2)	1.70	5.5x3.0	0	detected
16	3	101418.330(0.001)	5 _{3,3} – 5 _{1,4} A, (v _t =1)	203	0.04	0.03	-	-	≤0.09	≤0.4	≤7.37	-	-	not detected
17	3	101477.421(0.010)	18 _{3,15} – 18 _{3,16} E	111	1.8	0.03	-	-	≤7.79	≤32.8	≤14.99	-	-	blend with H ₂ CS
18	3	101545.453(0.010)	18 _{3,15} – 18 _{3,16} A	111	1.8	0.03	8.7(0.3)	4.0(0.6)	0.57	2.4(0.3)	1.10	5.5x2.7	0	detected
19	3	101626.884(0.010)	9 _{1,9} – 8 _{0,8} E	25	4.1	0.03	-	-	≤2.88	≤12.1	≤2.42	-	-	blend with HCOOCN
20	3	101628.149(0.010)	9 _{1,9} – 8 _{0,8} A	25	4.1	0.03	-	-	≤2.22	≤9.4	≤1.88	-	-	blend with HCOOCN-E
21	4	105663.117(0.030)	19 _{13,7} – 20 _{12,9} E, (v _t =1)	412	0.4	0.02	-	-	≤0.10	≤0.3	≤0.59	-	-	blend
22	4	105722.672(0.030)	10 _{4,6} – 10 _{3,8} E, (v _t =1)	230	0.5	0.02	-	-	≤0.06	≤0.2	≤0.32	-	-	not detected
23	5	105810.803(0.030)	14 _{11,4} – 15 _{10,6} E	142	0.2	0.02	-	-	≤0.06	≤0.2	≤0.79	-	-	not detected
24	5	105815.953(0.030)	3 _{3,1} – 2 _{2,0} E	10	0.2	0.02	7.9(0.1)	2.5(0.3)	0.15	0.4(0.1)	1.58	-	-	partial blend
25	5	105832.067(0.030)	14 _{11,3} – 15 _{10,5} E	142	0.2	0.02	7.6(0.2)	2.5(0.4)	0.14	0.4(0.1)	1.58	-	-	detected
26	6	110153.652(0.010)	10 _{1,10} – 9 _{1,9} A, (v _t =1)	218	25.1	0.11	-	-	≤3.32	≤6.6	≤0.20	-	-	blend with NH ₂ D
27	7	203349.158(0.006)	24 _{19,5} – 25 _{18,7} E	416	0.2	0.09	-	-	≤1.15	≤2.3	≤4.74	-	-	blend
28	7	203378.812(0.007)	24 _{19,6} – 25 _{18,8} E	416	0.2	0.09	-	-	≤16.84	≤33.7	≤69.38	-	-	blend
29	8	203427.575(0.100)	21 _{8,13} – 21 _{7,14} A, (v _t =1)	366	6.2	0.09	-	-	≤0.27	≤0.5	≤0.03	-	-	not detected
30	8	203435.554(0.100)	19 _{8,11} – 19 _{7,12} A	155	5.3	0.09	7.8(0.1)	2.0(0.3)	2.13	4.6(0.5)	0.36	-	-	partial blend
31	8	203471.840(0.050)	19 _{8,11} – 19 _{7,12} E	155	4.9	0.09	-	-	≤1.09	≤2.2	≤0.18	-	-	blend
32	9	223435.416(0.001)	11 _{4,8} – 10 _{3,7} A, (v _t =1)	237	1.8	0.20	-	-	≤0.60	≤1.2	≤0.25	-	-	not detected
33	9	223465.340(0.050)	11 _{4,8} – 10 _{3,7} E	50	2.1	0.20	8.0(0.1)	1.9(0.3)	3.83	7.7(2.5)	1.37	2.0x1.5	60	detected
34	9	223500.463(0.001)	11 _{4,8} – 10 _{3,7} A	50	1.8	0.20	8.0(0.1)	2.2(0.2)	1.90	4.4(0.4)	0.93	2.0x1.5	60	detected
35	9	223534.727(0.100)	18 _{5,14} – 17 _{5,13} E, (v _t =1)	305	41.6	0.20	8.7(0.3)	3.0(0.4)	1.78	5.8(0.8)	0.05	3.0x1.5	60	detected
36	9	223538.511(0.100)	43 _{8,35} – 43 _{7,36} E	618	13.9	0.20	-	-	≤0.60	≤1.2	≤0.03	-	-	not detected
37	9	223592.231(0.100)	43 _{8,35} – 43 _{7,36} A	618	13.9	0.20	-	-	≤0.60	≤1.2	≤0.03	-	-	not detected
38	9	223618.470(0.007)	27 _{9,19} – 27 _{8,19} E, (v _t =1)	464	0.4	0.20	-	-	≤0.60	≤1.2	≤1.20	-	-	not detected
39	9	223624.496(0.100)	37 _{8,30} – 37 _{7,31} E	463	11.7	0.20	-	-	≤0.60	≤1.2	≤0.04	-	-	not detected
40	9	223634.916(0.100)	37 _{8,30} – 37 _{7,31} A	463	11.7	0.20	-	-	≤0.60	≤1.2	≤0.04	-	-	not detected

C. Favre et al.: HCOOCN as a probe of temperature and structure of Orion-KL
 MNRAS **000**, 1–15 (2018)

Table A.3. continued.

N°	Set	Frequency (MHz)	Transition	E_{up} (K)	$S\mu^2$ (D ²)	sigma (K)	v (km s ⁻¹)	$\Delta v_{1/2}$ (km s ⁻¹)	T_{B} (K)	W (K km s ⁻¹)	$N_{\text{up}}/g_{\text{up}}$ (10 ¹² cm ⁻²)	Source size (" x ")	PA(°)	Comments
(1)	(2)	(3)	(4)	(5)	(6)	(7)	(8)	(9)	(10)	(11)	(12)	(13)	(14)	(15)
41	9	223642.180(0.001)	12 _{5,7} – 12 _{3,10} E	63	0.1	0.20	-	-	≤0.60	≤1.2	≤5.35	-	-	not detected
42	9	223645.342(0.001)	12 _{5,7} – 12 _{3,10} A	63	0.1	0.20	-	-	≤0.60	≤1.2	≤4.49	-	-	not detected
43	9	223651.592(0.007)	33 _{9,24} – 33 _{8,26} E, ($v_t=1$)	573	0.7	0.20	-	-	≤0.60	≤1.2	≤0.60	-	-	not detected
44	9	223676.472(0.006)	35 _{7,29} – 35 _{5,30} A, ($v_t=1$)	593	3.0	0.20	-	-	≤2.20	≤4.5	≤0.55	-	-	blend
45	9	223782.081(0.007)	33 _{6,28} – 33 _{5,29} E, ($v_t=1$)	543	7.0	0.20	-	-	≤0.60	≤1.2	≤0.06	-	-	not detected
46	9	223821.523(0.002)	35 _{7,29} – 35 _{6,30} E	409	8.2	0.20	-	-	≤0.60	≤1.2	≤0.05	-	-	not detected
47	9	223854.201(0.100)	35 _{7,29} – 35 _{6,30} A	409	10.1	0.20	-	-	≤0.60	≤1.2	≤0.04	-	-	not detected
48	10	225689.371(0.008)	34 _{5,29} – 34 _{5,30} A, ($v_t=1$)	562	3.0	0.12	-	-	≤20.83	≤41.7	≤5.19	-	-	blend
49	10	225696.842(0.100)	20 _{1,19} – 19 _{1,18} E, ($v_t=1$)	307	50.2	0.12	-	-	≤10.57	≤21.1	≤0.16	-	-	strongly blend
50	10	225702.857(0.100)	19 _{2,17} – 18 _{2,16} A, ($v_t=1$)	304	46.8	0.12	-	-	≤14.30	≤28.6	≤0.23	-	-	blend
51	10	225727.506(0.100)	6 _{6,1} – 5 _{5,0} A, ($v_t=1$)	224	3.1	0.12	-	-	≤0.71	≤1.4	≤0.17	-	-	blend
52	10	225727.506(0.100)	6 _{6,0} – 5 _{5,1} A, ($v_t=1$)	224	3.1	0.12	-	-	≤0.71	≤1.4	≤0.17	-	-	blend
53	11	225855.505(0.100)	6 _{6,1} – 5 _{5,1} E	36	3.1	0.07	-	-	≤1.02	≤2.0	≤0.24	-	-	blend
54	11	225900.684(0.100)	6 _{6,0} – 5 _{5,0} E	36	3.1	0.07	-	-	≤5.59	≤11.2	≤1.33	-	-	blend with HDO
55	11	225928.659(0.100)	6 _{6,0} – 5 _{5,1} A	36	3.1	0.07	-	-	≤1.74	≤3.5	≤0.42	-	-	blend
56	11	225928.659(0.100)	6 _{6,1} – 5 _{5,0} A	36	3.1	0.07	-	-	≤1.74	≤3.5	≤0.42	-	-	blend
57	12	225999.145(0.100)	30 _{7,23} – 29 _{8,22} E	312	2.2	0.09	-	-	≤0.27	≤0.5	≤0.08	-	-	not detected
58	12	226061.796(0.100)	20 _{3,17} – 19 _{4,16} E, ($v_t=1$)	321	4.0	0.09	-	-	≤0.27	≤0.5	≤0.05	-	-	not detected
59	12	226077.920(0.001)	10 _{3,7} – 9 _{1,8} E	39	0.3	0.09	-	-	≤0.27	≤0.5	≤0.65	-	-	not detected
60	12	226081.175(0.002)	30 _{7,23} – 29 _{8,22} A	312	1.8	0.09	-	-	≤0.27	≤0.5	≤0.10	-	-	not detected
61	12	226087.718(0.007)	29 _{4,26} – 29 _{3,27} A, ($v_t=1$)	450	4.3	0.09	-	-	≤0.84	≤1.7	≤0.15	-	-	blend
62	12	226090.301(0.100)	19 _{2,17} – 18 _{2,16} E, ($v_t=1$)	303	47.0	0.09	-	-	≤2.57	≤5.1	≤0.04	-	-	blend
63	12	226112.470(0.007)	29 _{4,26} – 29 _{2,27} A, ($v_t=1$)	450	2.1	0.09	-	-	≤0.27	≤0.5	≤0.09	-	-	not detected
64	12	226125.600(0.001)	10 _{3,7} – 9 _{1,8} A	39	0.3	0.09	-	-	≤0.32	≤0.6	≤0.78	-	-	blend

Notes: (1) Numbering of the observed transitions with $E_{\text{upper}} \lesssim 650$ K. (2) Reference number of the corresponding data set (see Table 1). (3) Frequencies and uncertainties taken from Ilyushin et al. (2009) and from the JPL database (<http://spec.jpl.nasa.gov/>). (4) Transitions in ground state ($v_t=0$). Transitions in torsional levels ($v_t=1$) are specified. (5) Energy of the upper level. (6) Line strength calculated by Ilyushin et al. (2009). For the transitions coming from the JPL database, the line strength is calculated from the formulae of Pickett et al. (1998). (7) Noise estimated from spectrum (1σ). (8) Lines with number 33 and 34 are decomposed. Only the first component is given here, other components are given in Table 4, except for line 30 because of the blend with the second component. (8), (9), (10) and (11) Velocity, linewidth at half intensity, brightness temperature and integrated intensities. The uncertainties are estimated with the CLASS software. (12) Column densities of the upper state of the transition with respect to the rotational degeneracy ($2J_{\text{up}}+1$). (13) and (14) Source size estimated at half flux density from detected transitions with spatial resolution allowing to isolate the source. (15) Blended lines are specified.

Table A.4. Transitions of methyl formate observed with the Plateau de Bure Interferometer toward position MF5 in Orion-KL

N°	Set	Frequency (MHz)	Transition	E _{up} (K)	Sμ ² (D ²)	sigma (K)	v (km s ⁻¹)	Δv _{1/2} (km s ⁻¹)	T _B (K)	W (K km s ⁻¹)	N _{up} /g _{up} (10 ¹² cm ⁻²)	Source size (" x " PA(°))	Comments	
(1)	(2)	(3)	(4)	(5)	(6)	(7)	(8)	(9)	(10)	(11)	(12)	(13)	(14)	(15)
1	1	80531.669(0.030)	9 _{2,8} – 9 _{0,9} E, (v _t =1)	216	0.6	0.03	-	-	≤0.09	≤0.4	≤0.69	-	-	not detected
2	1	80565.210(0.010)	10 _{2,8} – 9 _{3,7} E	36	1.1	0.03	-	-	≤0.21	≤0.8	≤0.75	-	-	blend
3	1	80572.589(0.010)	10 _{2,8} – 9 _{3,7} A	36	1.1	0.03	-	-	≤0.28	≤1.1	≤1.04	-	-	blend
4	2	80604.508(0.030)	12 _{9,3} – 13 _{8,5} E, (v _t =1)	288	0.2	0.11	-	-	≤5.48	≤21.9	≤113.37	-	-	blend
5	2	80652.521(0.010)	15 _{4,11} – 14 _{5,10} A	83	1.0	0.11	-	-	≤1.96	≤7.8	≤8.07	-	-	blend
6	3	101202.806(0.010)	9 _{1,9} – 8 _{0,8} A, (v _t =1)	213	4.2	0.04	7.7(0.2)	4.5(0.4)	0.43	2.1(0.2)	0.41	-	-	partial blend
7	3	101210.208(0.004)	24 _{3,21} – 25 _{2,24} A	187	0.04	0.04	-	-	≤0.41	≤1.9	≤41.21	-	-	blend
8	3	101279.006(0.010)	9 _{1,9} – 8 _{0,8} E, (v _t =1)	212	4.0	0.04	7.5(0.5)	4.6(1.2)	0.49	2.4(0.5)	0.49	5.0x2.7	0	detected
9	3	101289.471(0.010)	29 _{9,20} – 28 _{10,19} A, (v _t =1)	498	1.8	0.04	-	-	≤0.12	≤0.5	≤0.23	-	-	not detected
10	3	101302.159(0.010)	25 _{6,19} – 25 _{5,20} A	219	11.1	0.04	7.7(0.5)	5.5(1.4)	1.16	6.8(1.1)	0.50	-	-	partial blend
11	3	101305.506(0.010)	25 _{6,19} – 25 _{5,20} E	219	11.1	0.04	7.7(0.3)	4.2(0.6)	1.11	5.0(0.6)	0.37	5.0x2.7	0	detected
12	3	101318.966(0.010)	13 _{3,11} – 13 _{2,12} E, (v _t =1)	246	3.2	0.04	7.7(0.2)	4.5(0.5)	0.30	1.4(0.1)	0.36	4.5x2.7	20	detected
13	3	101356.788(0.010)	15 _{2,13} – 15 _{1,14} A, (v _t =1)	263	3.5	0.04	-	-	≤0.19	≤0.9	≤0.21	-	-	blend
14	3	101370.505(0.010)	13 _{3,11} – 13 _{2,12} E	60	3.2	0.04	7.9(0.1)	4.7(0.1)	1.42	7.1(0.1)	1.83	5.0x2.7	0	detected
15	3	101414.746(0.010)	13 _{3,11} – 13 _{2,12} A	60	3.2	0.04	7.8(0.1)	4.8(0.1)	1.42	7.2(0.1)	1.85	5.5x3.0	0	detected
16	3	101418.330(0.001)	5 _{3,3} – 5 _{1,4} A, (v _t =1)	203	0.04	0.04	-	-	≤0.12	≤0.5	≤9.22	-	-	not detected
17	3	101477.421(0.010)	18 _{3,15} – 18 _{3,16} E	111	1.8	0.04	-	-	≤7.56	≤34.4	≤15.72	-	-	blend with H ₂ CS
18	3	101545.453(0.010)	18 _{3,15} – 18 _{3,16} A	111	1.8	0.04	-	-	≤0.58	≤2.6	≤1.19	-	-	blend
19	3	101626.884(0.010)	9 _{1,9} – 8 _{0,8} E	25	4.1	0.04	-	-	≤2.89	≤13.1	≤2.62	-	-	blend with HCOOC _{1,1} -A
20	3	101628.149(0.010)	9 _{1,9} – 8 _{0,8} A	25	4.1	0.04	-	-	≤2.42	≤11.0	≤2.20	-	-	blend with HCOOC _{1,1} -E
21	4	105663.117(0.030)	19 _{13,7} – 20 _{12,9} E, (v _t =1)	412	0.4	0.02	-	-	≤0.08	≤0.2	≤0.39	-	-	blend
22	4	105722.672(0.030)	10 _{4,6} – 10 _{3,8} E, (v _t =1)	230	0.5	0.02	-	-	≤0.06	≤0.1	≤0.16	-	-	not detected
23	5	105810.803(0.030)	14 _{11,4} – 15 _{10,6} E	142	0.2	0.02	-	-	≤0.06	≤0.1	≤0.39	-	-	not detected
24	5	105815.953(0.030)	3 _{3,1} – 2 _{2,0} E	10	0.2	0.02	7.9(0.4)	2.6(0.3)	0.13	0.3(0.1)	1.18	-	-	partial blend
25	5	105832.067(0.030)	14 _{11,3} – 15 _{10,5} E	142	0.2	0.02	7.5(0.2)	2.1(0.3)	0.12	0.3(0.1)	1.18	-	-	detected
26	6	110153.652(0.010)	10 _{1,10} – 9 _{1,9} A, (v _t =1)	218	25.1	0.10	-	-	≤2.75	≤7.2	≤0.22	-	-	blend with NH ₂ D
27	7	203349.158(0.006)	24 _{19,5} – 25 _{18,7} E	416	0.2	0.16	-	-	≤1.44	≤2.9	≤5.97	-	-	blend
28	7	203378.812(0.007)	24 _{19,6} – 25 _{18,8} E	416	0.2	0.16	-	-	≤4.30	≤8.6	≤17.71	-	-	blend
29	8	203427.575(0.100)	21 _{8,13} – 21 _{7,14} A, (v _t =1)	366	6.2	0.16	-	-	≤0.48	≤1.0	≤0.07	-	-	not detected
30	8	203435.554(0.100)	19 _{8,11} – 19 _{7,12} A	155	5.3	0.16	-	-	≤1.85	≤3.7	≤0.29	-	-	blend
31	8	203471.840(0.050)	19 _{8,11} – 19 _{7,12} E	155	4.9	0.16	-	-	≤1.25	≤2.5	≤0.21	-	-	blend
32	9	223435.416(0.001)	11 _{4,8} – 10 _{3,7} A, (v _t =1)	237	1.8	0.27	-	-	≤0.81	≤1.7	≤0.35	-	-	not detected
33	9	223465.340(0.050)	11 _{4,8} – 10 _{3,7} E	50	2.1	0.27	7.8(0.1)	4.3(0.3)	2.2	10.1(0.6)	1.79	2.0x1.5	60	detected
34	9	223500.463(0.001)	11 _{4,8} – 10 _{3,7} A	50	1.8	0.27	7.6(0.1)	4.2(0.2)	2.4	10.7(0.5)	2.26	2.0x1.5	60	detected
35	9	223534.727(0.100)	18 _{5,14} – 17 _{5,13} E, (v _t =1)	305	41.6	0.27	8.1(0.1)	5.7(0.3)	2.5	15.1(0.8)	0.14	3.0x1.5	70	detected
36	9	223538.511(0.100)	43 _{8,35} – 43 _{7,36} E	618	13.9	0.27	-	-	≤0.81	≤1.7	≤0.05	-	-	not detected
37	9	223592.231(0.100)	43 _{8,35} – 43 _{7,36} A	618	13.9	0.27	-	-	≤0.81	≤1.7	≤0.05	-	-	not detected
38	9	223618.470(0.007)	27 _{9,19} – 27 _{8,19} E, (v _t =1)	464	0.4	0.27	-	-	≤0.81	≤1.7	≤1.70	-	-	not detected
39	9	223624.496(0.100)	37 _{8,30} – 37 _{7,31} E	463	11.7	0.27	-	-	≤0.81	≤1.7	≤0.05	-	-	not detected
40	9	223634.916(0.100)	37 _{8,30} – 37 _{7,31} A	463	11.7	0.27	-	-	≤0.81	≤1.7	≤0.05	-	-	not detected

C. Favre et al.: HCOOC_{1,1} as a probe of temperature and structure of Orion-KL
Online Material p 8

Table A.4. continued.

N°	Set	Frequency (MHz)	Transition	E _{up} (K)	Sμ ² (D ²)	sigma (K)	v (km s ⁻¹)	Δv _{1/2} (km s ⁻¹)	T _B (K)	W (K km s ⁻¹)	N _{up} /g _{up} (10 ¹² cm ⁻²)	Source size (" x ") PA(°)	Comments	
(1)	(2)	(3)	(4)	(5)	(6)	(7)	(8)	(9)	(10)	(11)	(12)	(13)	(14)	(15)
41	9	223642.180(0.001)	12 _{5,7} – 12 _{3,10} E	63	0.1	0.27	-	-	≤0.81	≤1.7	≤7.57	-	-	not detected
42	9	223645.342(0.001)	12 _{5,7} – 12 _{3,10} A	63	0.1	0.27	-	-	≤0.81	≤1.7	≤6.37	-	-	not detected
43	9	223651.592(0.007)	33 _{9,24} – 33 _{8,26} E, (v _t =1)	573	0.7	0.27	-	-	≤0.81	≤1.7	≤0.85	-	-	not detected
44	9	223676.472(0.006)	35 _{7,29} – 35 _{5,30} A, (v _t =1)	593	3.0	0.27	-	-	≤0.81	≤1.7	≤0.21	-	-	not detected
45	9	223782.081(0.007)	33 _{6,28} – 33 _{5,29} E, (v _t =1)	543	7.0	0.27	-	-	≤0.81	≤1.7	≤0.09	-	-	not detected
46	9	223821.523(0.002)	35 _{7,29} – 35 _{6,30} E	409	8.2	0.27	-	-	≤0.81	≤1.7	≤0.08	-	-	not detected
47	9	223854.201(0.100)	35 _{7,29} – 35 _{6,30} A	409	10.1	0.27	-	-	≤0.81	≤1.7	≤0.06	-	-	not detected
48	10	225689.371(0.008)	34 _{5,29} – 34 _{5,30} A, (v _t =1)	562	3.0	0.13	-	-	≤15.43	≤30.9	≤3.85	-	-	blend
49	10	225696.842(0.100)	20 _{1,19} – 19 _{1,18} E, (v _t =1)	307	50.2	0.13	-	-	≤13.25	≤26.5	≤0.20	-	-	blend
50	10	225702.857(0.100)	19 _{2,17} – 18 _{2,16} A, (v _t =1)	304	46.8	0.13	-	-	≤7.71	≤15.4	≤0.12	-	-	blend
51	10	225727.506(0.100)	6 _{6,1} – 5 _{5,0} A, (v _t =1)	224	3.1	0.13	-	-	≤0.90	≤1.8	≤0.21	-	-	blend
52	10	225727.506(0.100)	6 _{6,0} – 5 _{5,1} A, (v _t =1)	224	3.1	0.13	-	-	≤0.90	≤1.8	≤0.21	-	-	blend
53	11	225855.505(0.100)	6 _{6,1} – 5 _{5,1} E	36	3.1	0.08	-	-	≤1.20	≤2.4	≤0.29	-	-	blend
54	11	225900.684(0.100)	6 _{6,0} – 5 _{5,0} E	36	3.1	0.08	-	-	≤3.16	≤6.3	≤0.75	-	-	blend with HDO
55	11	225928.659(0.100)	6 _{6,0} – 5 _{5,1} A	36	3.1	0.08	-	-	≤1.53	≤3.1	≤0.37	-	-	blend
56	11	225928.659(0.100)	6 _{6,1} – 5 _{5,0} A	36	3.1	0.08	-	-	≤1.53	≤3.1	≤0.37	-	-	blend
57	12	225999.145(0.100)	30 _{7,23} – 29 _{8,22} E	312	2.2	0.10	-	-	≤0.30	≤0.6	≤0.10	-	-	not detected
58	12	226061.796(0.100)	20 _{3,17} – 19 _{4,16} E, (v _t =1)	321	4.0	0.10	-	-	≤0.30	≤0.6	≤0.06	-	-	not detected
59	12	226077.920(0.001)	10 _{3,7} – 9 _{1,8} E	39	0.3	0.10	-	-	≤0.30	≤0.6	≤0.79	-	-	not detected
60	12	226081.175(0.002)	30 _{7,23} – 29 _{8,22} A	312	1.8	0.10	-	-	≤0.30	≤0.6	≤0.12	-	-	not detected
61	12	226087.718(0.007)	29 _{4,26} – 29 _{3,27} A, (v _t =1)	450	4.3	0.10	-	-	≤0.79	≤1.6	≤0.14	-	-	blend
62	12	226090.301(0.100)	19 _{2,17} – 18 _{2,16} E, (v _t =1)	303	47.0	0.10	-	-	≤1.00	≤2.0	≤0.02	-	-	blend
63	12	226112.470(0.007)	29 _{4,26} – 29 _{2,27} A, (v _t =1)	450	2.1	0.10	-	-	≤0.30	≤0.6	≤0.11	-	-	not detected
64	12	226125.600(0.001)	10 _{3,7} – 9 _{1,8} A	39	0.3	0.10	-	-	≤0.59	≤1.2	≤1.57	-	-	blend

Notes: (1) Numbering of the observed transitions with E_{upper} ≤ 650 K. (2) Reference number of the corresponding data set (see Table 1). (3) Frequencies and uncertainties taken from Ilyushin et al. (2009) and from the JPL database (<http://spec.jpl.nasa.gov/>). (4) Transitions in ground state (v_t=0). Transitions in torsional levels (v_t=1) are specified. (5) Energy of the upper level. (6) Line strength calculated by Ilyushin et al. (2009). For the transitions coming from the JPL database, the line strength is calculated from the formulae of Pickett et al. (1998). (7) Noise estimated from spectrum (1σ). (8), (9), (10) and (11) Velocity, linewidth at half intensity, brightness temperature and integrated intensities. The uncertainties are estimated with the CLASS software. (12) Column densities of the upper state of the transition with respect to the rotational degeneracy (2J_{up}+1). (13) and (14) Source size estimated at half flux density from detected transitions with spatial resolution allowing to isolate the source. (15) Blended lines are specified.

This figure "fig.gif" is available in "gif" format from:

<http://arxiv.org/ps/1103.2548v1>